

*p*ISSN 2615-5109
*e*ISSN 2621-0541

INTERNATIONAL JOURNAL OF ENGINEERING

EPI

Volume 5 Number 1, February 2022

Publisher:



Center of Technology
Fakultas Teknik, Universitas Hasanuddin
Gowa, Indonesia



Copyright © 2022, Publication Division, Center of Technology (CoT)
Faculty of Engineering, Hasanuddin University

Print edition ISSN 2615-5109
Electronic edition ISSN 2621-0541

Reproduction in whole or in part by any means, is subject to permission in writing by Publication Division, Center of Technology (CoT), Faculty of Engineering, Hasanuddin University. All Rights Reserved.

Publisher:

Center of Technology, Fakultas Teknik, Universitas Hasanuddin

Address:

Engineering Faculty Campus, Hasanuddin University
Jl. Poros Malino km. 6, Bontomarannu
Kabupaten Gowa, Sulawesi Selatan, Indonesia, 92171
Email : epi-ije@unhas.ac.id
Website : cot.unhas.ac.id/journals/index.php/epiije
Telp/Fax : +62-(0)411-58601

EPI International Journal of Engineering

Editorial Board

Editor-in-Chief : **Dr. Faisal Mahmuddin**, Hasanuddin University (Makassar, Indonesia)

Associate Editors : **Prof. Yoshihiro Narita**, Hokkaido University (Sapporo, Japan)
Prof. Ahmad Fitriadhy, Universiti Malaysia Terengganu (Terengganu, Japan)

Editorial Board :

- Indonesia

Prof. Muh. Arsyad Thaha, Hasanuddin University (Makassar, Indonesia)
Prof. Wahyu Haryadi Piarah, Hasanuddin University (Makassar, Indonesia)
Prof. M. Ramli Rahim, Hasanuddin University (Makassar, Indonesia)
Prof. Herman Parung, Hasanuddin University (Makassar, Indonesia)
Prof. Imran Umar, Hasanuddin University (Makassar, Indonesia)
Dr. Rhiza S. Sadjad, Hasanuddin University (Makassar, Indonesia)
Dr. Ganding Sitepu, Hasanuddin University (Makassar, Indonesia)
Prof. Satriyo Brodjonegoro, Bandung Institute of Technology (Bandung, Indonesia)
Prof. I Ketut Aria Pria Utama, Surabaya Institute of Technology (Surabaya, Indonesia)
Dr. Arifuddin Idrus, Gadjah Mada University (Yogyakarta, Indonesia)
Dr. Ngurah Nitya, Udayana University (Denpasar, Indonesia)
Dr. Putu Wijaya Sunu, Bali State Polytechnic (Denpasar, Indonesia)
Dr. Lukiyanto YB, Sanata Dharma University (Yogyakarta, Indonesia)
Dr. Farid Triawan, Sampoerna University (Jakarta, Indonesia)

- Outside Indonesia

Prof. Erasmo Carrera, Polytechnic University of Turin (Torino, Italy)
Prof. Mark Ewing, University of Kansas (Lawrence, USA)
Prof. Danna Ganbat, Mongol University of Science and Technology (Ulaanbaatar, Mongolia)
Prof. S. Ilanko, University of Waikato (Hamilton, New Zealand)
Prof. David Kennedy, Cardiff University, (Cardiff, United Kingdom)
Prof. Larry Lessard, McGill University (Montreal, Canada)
Prof. Woo Il Lee, Seoul National University (Seoul, Korea)
Prof. Oliver Polit, University Paris Ovest (Paris, France)
Prof. Vasaka Visoottiviseth, Mahidol University, (Bangkok, Thailand)
Dr. Jane Louie Fresco Zamora, Weathernews Inc. (Chiba, Japan)
Dr. Kazunori Abe, Akita University (Akita, Japan)
Prof. Jun Ando, Kyushu University (Fukuoka, Japan)
Prof. Satoshi Echizenya, Yamato University (Osaka, Japan)
Prof. Naohiro Hozumi, Toyohashi University of Technology (Toyohashi, Japan)
Prof. Shigeru Kashihara, Osaka Institute of Technology (Osaka, Japan)
Prof. Akio Miyara, Saga University (Saga, Japan)
Dr. Yusuke Mochida, University of Waikato (Hamilton, New Zealand)
Prof. Prakash Bhandary Netra, Ehime Univ. (Matsuyama, Japan)
Prof. Yoshiki Ohta, Hokkaido University of Science (Sapporo, Japan)
Prof. Tsubasa Otake, Hokkaido University (Sapporo, Japan)
Prof. Nobumasa Sekishita, Toyohashi University of Technology (Toyohashi, Japan)
Prof. Masao Yamawaki, Yamato University (Osaka, Japan)
Prof. Hideaki Yasuhara, Ehime University (Matsuyama, Japan)

Foreword

We are glad that the EPI International Journal of Engineering (EPI-IJE) Volume 5 Number 1 February 2022 has been published. After considering the publication time and for quality improvement purposes, from this edition, the number of manuscripts to be published in one edition will be reduced. If the previous editions have around 14 manuscripts, then starting from this edition, it only has a maximum of 9 or 10 manuscripts.

Therefore, this edition consists of only 10 (ten) manuscripts. The first manuscript is related to the strength of the cutter suction dredger ship. It is followed by a manuscript related to tracking shoe patterns for vehicles on sandy terrain. The third manuscript conducted a simulation of a double-stage single-phase PV system, while the next manuscript studied mining equipment productivity data using K-Means algorithm.

The fifth and sixth manuscripts investigated the natural frequencies of isotropic rectangular plates and vibration signals from cutting tools for CNC turning monitoring systems, respectively. The next two manuscripts studied the performance of TEC cascade in a fish cooler box and the classification freshness of red snapper using a convolutional neural network. The subsequent manuscript discussed the semiotic perspective of Hunto Sultan Amai Mosque ornaments in Gorontalo. The last manuscript examined the thermal sensation in the building of Universitas Ichsan Gorontalo.

We highly appreciate all authors for their contribution to this edition. We are also always grateful to all other people and parties for their ongoing support for the EPI journal publication. We hope the published manuscripts will have a positive contribution to the future development of science and technology.

Warm regards,

Dr. Faisal Mahmuddin
Editor-in-Chief of EPI-IJE

TABLE OF CONTENTS

Editorial Board	i
Foreword	ii
Table of contents	iii
Strenght Analysis due to the Elongation’s Ladder of Cutter Suction Dredger Ship	1-9
Hariyono (Hasanuddin University, Indonesia)	
Ganding Sitepu (Hasanuddin University, Indonesia)	
Muhammad Zubair Muis Alie (Hasanuddin University, Indonesia)	
Numerical and Experimental Analyses of Track Shoe Patterns for Vehicle on Sandy Terrain.....	10-15
.....	
Ignatius Pulung Nurprasetio (Institut Teknologi Bandung, Indonesia)	
Wiryawicaksana (Institut Teknologi Bandung, Indonesia)	
Siti Zulaikah (National Center for Sustainable Transportation Technology, Indonesia)	
Bentang Arief Budiman (Institut Teknologi Bandung, Indonesia)	
Modeling and Simulation of a Double-Stage Single-Phase Grid-Connected PV System	16-20
.....	
Cannareth Srun (Institute of Techonology of Cambodia)	
Phok Chrin (Institute of Techonology of Cambodia)	
Sokchea Am (Institute of Techonology of Cambodia)	
Bunthern Kim (Institute of Techonology of Cambodia)	
Clustering Mining Equipment Productivity Data using K-Means Algorithm	21-25
.....	
Muhammad Sandi Arista Ikhsan Yahmid (Hasanuddin University, Indonesia)	
Tony Chen (Hasanuddin University, Indonesia)	
Muhammad Emirat Millenium Try (Hasanuddin University, Indonesia)	
Karno Nugroho Silangin (Hasanuddin University, Indonesia)	
Nurul Alifia Putri (Hasanuddin University, Indonesia)	
Aryanti Virtanti Anas (Hasanuddin University, Indonesia)	
Natural Frequencies of Isotropic Rectangular Plates in Improved Accuracy.....	26-36
.....	
Yoshihiro Narita (Hakkaido University, Japan)	
Characteristic of Vibration Signal from Cutting Tool Against Steel with a Tensile Strenght of 60 for CNC Turning Monitoring System	37-43
.....	
Muh Fachrul (Polytechnic of Bosowa, Indonesia)	
Ahmad Yusran Aminy (Hasanuddin University, Indonesia)	
Azwar Hayat (Hasanuddin University, Indonesia)	
Performance of TEC Cascade on Input Voltage Variations in Fish Cooler Box.....	44-49
.....	
Sabiqunassabiqun (Universitas Hasanuddin, Indonesia)	
Zuryati Djafar (Universitas Hasanuddin, Indonesia)	
Wahyu Haryadi Piarah (Universitas Hasanuddin, Indonesia)	

Classification Freshness of Red Snapper (<i>Lutjanus Campechanus</i>) Based on Eye Image Using Convolutianal Neural Network.....	50-56
Muh Subhan (Politeknik Negeri Fakfak, Indonesia) Nursakinah (Politeknik Negeri Fakfak, Indonesia)	
Semiotic Perspective of Charateristics and Meanings of Hunto Sultan Amai Mosque Ornaments in Gorontalo.....	57-70
Asmin Salongi (Universitas Hasanuddin, Indonesia) Afifah Harisah (Universitas Hasanuddin, Indonesia) Ria Wikantari (Universitas Hasanuddin, Indonesia)	
Thermal Sensation Analysis in the Building of Universitas Ichsan Gorontalo	71-80
Siti Khairunnisa Abay (Universitas Hasanuddin, Indonesia) Baharuddin Hamzah (Universitas Hasanuddin, Indonesia) Rosady Mulyadi (Universitas Hasanuddin, Indonesia)	

Strength Analysis due to the Elongation's Ladder of Cutter Suction Dredger Ship

Hariyono^{a,*}, Ganding Sitepu^b, Muhammad Zubair Muis Alie^c

^aDepartment of Naval Architecture, Engineering Faculty, Hasanuddin University, Gowa, Indonesia. Email: hariyono.ismail07@gmail.com

^bDepartment of Naval Architecture, Engineering Faculty, Hasanuddin University, Gowa, Indonesia. Email: g.sitepu@unhas.ac.id

^cDepartment of Ocean Engineering, Engineering Faculty, Hasanuddin University, Gowa, Indonesia. Email: zubair.m@eng.unhas.ac.id

Abstract

The more frequent mining activities are carried out, the deeper the tin on the seabed, therefore many ship owners want to increase the length of the ladder on production suction vessels. The owner of the KIP Timah 8 suction boat will increase the length of the ladder to 70 meters, which previously was only 58 meters. The paper research are the response of the ladder structure before and after being extended, the limit strength of the ladder structure in the pulley area, then the ultimate strength of the longitudinal ladder structure due to the vertical bending moment. Length of the ladder construction subsequently increases commencing 58 m, 62 m, 66 m, to 70 m with each increase in length varying the slope angle of the ladder starting from 0°, 30°, 45°, to 60°. This paper uses a numerical method with the help of ansys software. The structure being reviewed is only in the ship ladder area. The response of the ladder structure before and after being extended, the maximum stress value occurs in the strut construction which is 49 meters from the ladder shaft, which is 56.88 N/mm² and the maximum shift is 14.28 mm when the ladder length is 70 meters and still meets the allowable stress. Investigation of the limit strength using the Nonlinear Finite Element Analysis (NLFEA) method. Based on the results the analysis of the strength longitudinal ladder structure in the hogging and sagging conditions 42 meters from the ladder shaft, the maximum deflection in the column is 131.73 mm from the initial position before being loaded. While at an angle of 60 degrees it will collapse when deflection 66.17 mm. The results of the analysis showed that the load acting on the ladder the pipe load, cutter load and cutter torque the resulting stress still meets the stress that the longer ladder is directly proportional to the resulting stress and deflection value and the greater the slope of the ladder, the smaller stress and deflection.

Keyword: Bending moment; NLFEA; ladder; ultimate strength

1. Introduction

Bangka, Belitung and Batam island the highest tin producers in Indonesia both on land and at sea. Currently, the economic driver for this region is still dominated by the tin processing sector. The management of tin mining must be as good as possible in order to benefit many parties. Mining at sea requires facilities such as ships. The ship used to mine tin is called the Kapal Isap Produksi (KIP), which is a digging or soil removal tool used to dig the subsoil, mechanical equipment and material processing rests on a pontoon. The sub-soil containing tin sand is cut using a cutter/cutter. As a floating device, the hallmark of a Kapal Isap Produksi (KIP) is that it consists of 4 capsules (Pontoon), the right and left side capsules are shorter and two capsules in the middle are longer. There

is also a ladder, which is a long steel frame that functions as a pole and a place for placing suction pipes, mud pumps, pressure pipes and cutters located at the end of the ladder as a cutter that is installed in the middle of the ship which is used to dig for tin on the seabed.

Maximum inclination of the ladder when operating is 60 degrees. The tin on the seabed is getting deeper because mining is often carried out so that many ship owners want to increase the length of their ship's ladder in the hope that they can still reach the seabed to mine tin. Modification of the ship's ladder is done so that it can be used for mining at sea. The Ladder KIP Timah 8 will be extended to be able to mine deeper. Several ladders experienced structural failure on other ships with relatively similar ladder lengths to the length of KIP Timah 8 ladder, possibly due to corrosion, ladder age and ladder strength (structure). Efforts to lengthen the ladder must be carried out with reliable calculations so that there will be no failure since cost of repairing a broken ladder is very expensive 6 billion. Therefore an

*Corresponding author. Tel.: +62-823-9431-3349
Jalan Poros Malino km. 6, Bontomarannu
Gowa, Indonesia, 92171

analysis of the ladder structure is necessarily to be conducted to minimize the level of damage (broken) on the ladder ship.

This paper presents research are the response of the ladder structure before and after being extended, the ultimate strength of the ladder structure in the pulley area, then the ultimate strength of the longitudinal ladder structure due to the vertical bending moment. In order for the simulation of the analysis of the ladder strength the production suction ship in accordance with the reality, use the existing ladder data. The type of data in this paper is secondary data. Secondary data is data obtained from sources related to the object of research, including pictures of stairs construction and materials used. The initial stage in the analysis is the collection of preliminary data in the form of the main dimension of the ship, the drawing of the ladder. Then the calculation of pipe load, cutter load and cutter torque is carried out. After that, ladder structure modeling is carried out for each length increase ranging from 58 meters, 62 meters, 66 meters and 70 meters. Each increase in length varies the angle of the ladder ranging from 0 degrees, 30 degrees, 45 degrees and 60 degrees.

1.1. Mining Technical at KIP Timah 8

Kapal Isap Produksi (KIP) Tin 8 is owned by PT. Timah (Persero) has dimensions of a total length of 85.5 meters, a total width of 22 meters, and a total height of 10.5 meters with a cutter section dredger type and started operating in 2010. The operation of KIP is determined from the specifications of the excavation equipment, namely the length of the ladder and the maximum angle of the ladder. with a water surface that affects the maximum depth that can be produced. Pontoons are a very important part of the operation of KIP. A pontoon is a floating object whose role is to hold the ship afloat. KIP's pontoon is made of hollow steel in the form of a capsule and the pontoon is divided into four main parts, namely two inner pontoons and two outer pontoons. The pontoon is divided into several compartments as shown in Fig. 1.

Superstructure is the part that functions as a means of supporting the other parts so that the ship's construction is stronger and more durable. In KIP there are two main decks, namely the lower deck and the upper deck. All equipment on the upper deck is held by the hull so that the ship remains stable as for the propulsion engine, hydraulic engine and ladder as shown in Fig. 2.

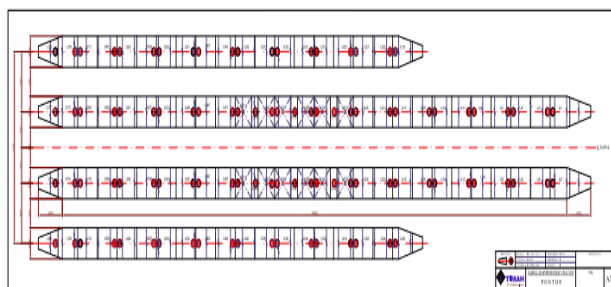


Figure 1. Schematic the pontoon [1]

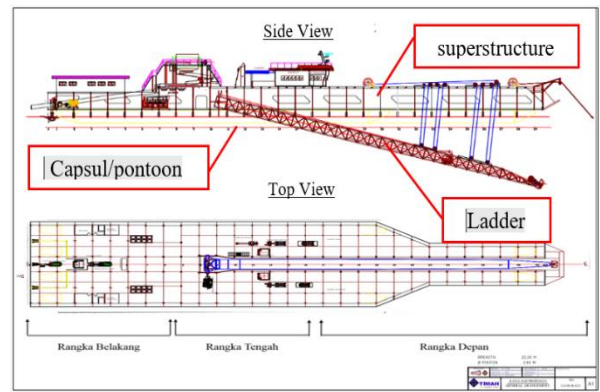


Figure 2. Top view and side view of KIP Timah 8 [1]

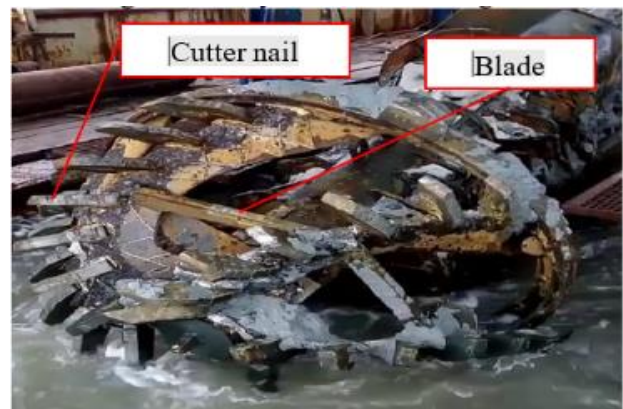


Figure 3. Cutter head [1]

Figure 2 is the construction of a Kapal Isap Produksi (KIP) Timah 8 which consists of a superstructure with a girder profile connected to the pontoon and also equipped with a cutter head on the ladder as a tool for cutting the soil layer as shown in Fig. 3.

1.2. Pipe Construction

In general, pipe is a term used to designate a hollow tubular body used to transport any impurities that have flow characteristics such as those found in liquids, gases, vapors, liquid solids, and fine powders. Just as there are different manufacturing methods, there are also different ways to categorize pipe sizes. Pipes are identified by three different size categories: nominal pipe size, outside diameter, and inside diameter as in Fig. 4 [2].

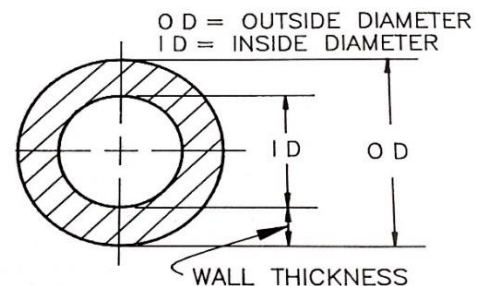


Figure 4. Pipe diameter [2]

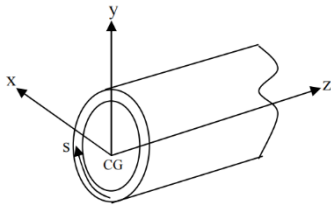


Figure 5. Coordinates of thin walled beams [5]

Laser measurements are used to get the exact shape of the steel pipe; Based on the digital inverse modeling technology, the actual constitutive equation of the steel pipe material is introduced to perform precise simulations on the buckling behavior of steel pipes under internal stress and bending conditions, and establish a technological numerical simulation for the buckling strain capacity of steel pipes [3].

The formulation in the beam finite element is based on the theory of thin-walled beams. Here, the fundamental theory of thin-walled beam elements includes torsional effects as a general case [4]. The x and y axes are defined on the beam cross section and the z axis is parallel to the beam axis. The origin of the coordinate system is located at the center of gravity of the cross section. The s-coordinate is defined along the center thickness line. Assuming that the cross section remains undistorted during deformation, the displacements U, V and W in Equations (1, 2, and 3) at x, y, and z at coordinates (x, y, z) can be expressed as in Fig. 5 [5].

$$U(x,y,z) = u_s(z) - (y-y_s)\theta(z) \quad (1)$$

$$V(x,y,z) = v_s(z) + (x-x_s)\theta(z) \quad (2)$$

$$W(x,y,z) = w(z) + xu'_s(z) - yv'_s(z) + \omega_{ns}(x,y)\theta'(z) \quad (3)$$

Where u_s and v_s are the displacements at the center of shear in the x and y directions and w are the displacements at the center of gravity in the z direction. θ is the angle of rotation about the center of shear. x_s and y_s are the x and y coordinates of the center of shear. ns is the bending function in the central shear. The prime number (') indicates the differentiation to the z-coordinate [5].

1.3. Frame Structure

Frame structure is a structure whose elements consist of tensile bars, columns, beams, and bars that are subjected to bending and axial loads. Most common building constructions that fall into this category are high rise buildings which usually consist of beams and columns that are rigidly joined or with simple end joints with diagonal bracing for stability. Although multi-storey buildings are three-dimensional in shape, when designed with rigid joints, they usually have much greater rigidity in one direction than in the other [6]. Several cross-sectional shapes such as square, round, angled, rectangular and various others are produced in a wide range of sizes and are used as well as flat plates and solid bars of various thicknesses. The wide wing profile is a profile that is widely used as a plate holder as shown in Fig. 6 [4].

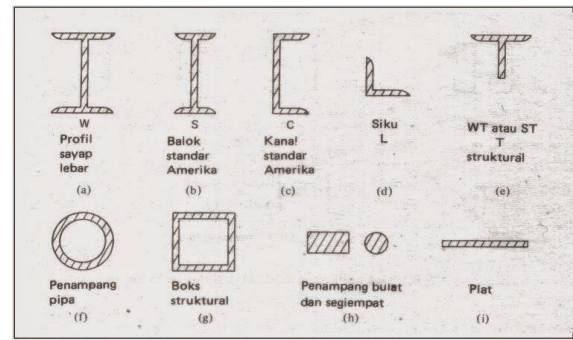


Figure 6. Cross section of the profile [4]

The bracing system serves to help transmit horizontal loads to the foundation, protect the integrity of the structure during the fabrication and installation process, and resist jolts from the installed jacket-pile system, as well as supporting the corrosion anode and well conductors and transmitting the generated wave force to the foundation. Another important characteristic of the tubular frame is the stability of the cross section which is expressed in the diameter/wall thickness ratio (d/t) which also indicates stability against local buckling. The buckling strength at the toe of the deck must be designed so that the deck platform has sufficient strength not only to support but also for the safety of people working on the platform including all facilities [7].

1.4. Loads Acting on the Structure

Dead load is a load that comes from the weight of the ladder structure itself and the weight of various permanent equipment located on the ladder structure and additional equipment whose weight does not change under operating conditions [7]. Live loads are loads that apply to the structure during its operation only and can vary during operating conditions or from operating conditions to other conditions. live load is a gravity load on a structure, which varies in size and location, examples of live loads are humans, furniture, movable equipment. Since the weight, location and density of live loads are unknown, the actual magnitude and position of these loads are very large. difficult to determine [7].

1.5. Stress, Strain and Deflection

Three positive normal stresses x, y and z, and 6 positive shear stresses, xy, yx, τ_{yz} , zy, zx, and xz as shown in Fig. 7 are shown to ensure static balance, as Eq. 4 applies [8].

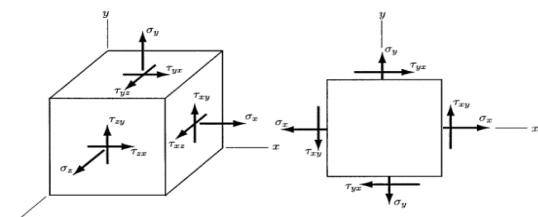


Figure 7. Stress acting on a plane [8]

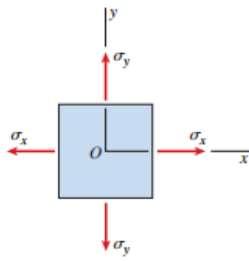


Figure 8. Biaxial stress system [8]

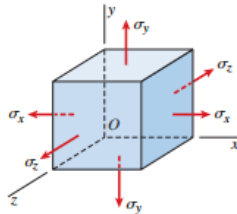


Figure 9. Triaxial stress system [8]

$$\tau_{xy} = \tau_{yx}, \quad \tau_{yz} = \tau_{zy}, \quad \tau_{zx} = \tau_{xz} \quad (4)$$

$$\sigma_x = \frac{E}{(1+\nu)(1-2\nu)} [\epsilon_x(1+\nu) + \nu(\epsilon_y + \epsilon_z)] \quad (5)$$

$$\sigma_y = \frac{E}{(1+\nu)(1-2\nu)} [\epsilon_y(1+\nu) + \nu(\epsilon_x + \epsilon_z)] \quad (6)$$

$$\sigma_z = \frac{E}{(1+\nu)(1-2\nu)} [\epsilon_z(1+\nu) + \nu(\epsilon_x + \epsilon_y)] \quad (7)$$

Strain is a measure of how far the bar is deformed shown in Fig. 8.

In a special case, the biaxial stress as in Fig. 8 occurs when in a structure the axial load acts in two mutually perpendicular axes [8].

The strains produced by the stresses x , y , and z as in Fig. 9 which work independently to obtain the resulting strain can be seen in Eqs. 7, 8, and 9 [8].

$$\epsilon_x = \frac{\sigma_x}{E} - \frac{\nu}{E} (\sigma_y + \sigma_z) \quad (8)$$

$$\epsilon_y = \frac{\sigma_y}{E} - \frac{\nu}{E} (\sigma_z + \sigma_x) \quad (9)$$

$$\epsilon_z = \frac{\sigma_z}{E} - \frac{\nu}{E} (\sigma_x + \sigma_y) \quad (10)$$

Deflection is a change in the shape of the beam in the y direction due to the vertical loading applied to the beam or rod [9]. The allowable stress is the highest stress allowed in a construction or it can be said as the maximum stress that occurs in the construction that is not allowed to be exceeded. In particular, the allowable stress is determined by BKL [10] that the working allowable stress should not exceed the stress in Eq. 11.

$$\text{Stress} = 150/k \text{ [N/mm}^2\text{]} \text{ with } k = \text{steel factor} \quad (11)$$

The stress-strain diagram for a typical structural steel in tension is shown in Fig. 10. Strain on the horizontal axis and stress on the vertical axis.

The relationship between the strength-limit bending moment and curvature is shown in Fig. 11 a positive curvature value indicates a hogging condition and a negative curvature value indicates a sagging condition [12].

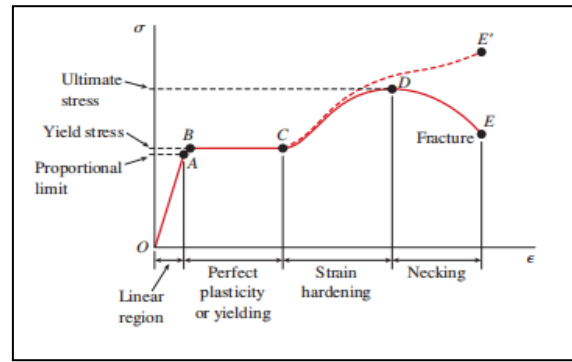


Figure 10. The relationship between stress-strain [11]

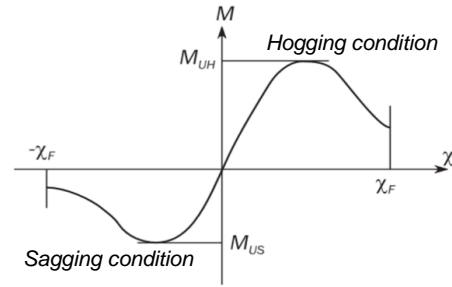


Figure 11. Bending moment strength and curvature [12]

The ultimate strength of the structure depends on various influencing factors, namely geometric/material properties, loading characteristics, related fabrication imperfections, boundary conditions and local damage age related to corrosion, fatigue cracking and deformation [13]. Column members are subjected to yielding and their capacity begins to decrease with increasing deflection. In this sense, the buckling strength of the column member is the maximum load and can be considered as the limiting strength [14]. Ultimate strength for ships that suffered damage to the hull due to aground has been carried out with good results by using Finite Element (FE) [15]. So, with the assumption that the ladder installed on the Kapal Isap Produksi (KIP) Timah 8 can also be calculated with the ultimate strength.

The phenomenon of buckling is usually divided into three categories, namely elastic buckling, elastic-plastic buckling and plastic buckling, the latter two being called inelastic buckling. In-plane stiffness is significantly reduced after the start of buckling. In this case, elastic bending of the seams between the supports may be permitted in the design, sometimes intentionally to save weight of the material. Since significant residual strength of the coating is not expected after buckling occurs in inelastic but inelastic buckling is usually considered as the limiting strength [14].

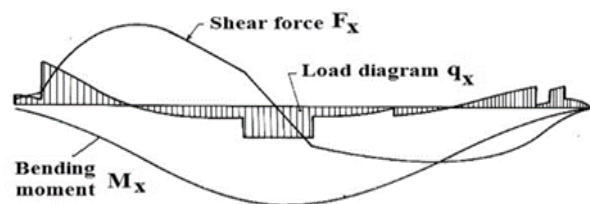


Figure 12. Distribution of loads, shear forces and bending moments on the ship [17]

The bending moments and shear forces in calm water conditions are derived from the buoyancy and weight distribution along the length of the ship as shown in Fig. 12 [16].

2. Research Method

The type of research used is a quantitative simulation to describe the analysis of the strength of the ladder structure for the Kapal Isap Produksi (KIP) Timah 8 after the addition of length. In order for the simulation of the analysis of the strength of the extension of the cutter suction dredger ladder in accordance with reality, the existing ladder data is used. The type of data in this study is secondary data. Secondary data is data obtained from sources related to the object of research, including ladder construction drawings and the materials used. The initial stage in the analysis is the collection of initial data in the form of the main size of the ship, ladder drawings. Then do the calculation of pipe load, cutter load and cutter torque. After that, the structural modeling is modeled for each additional length starting from 58 m, 62 m, 66 m and 70 m. Each increase in length varies the ladder angle starting from 0 degrees, 30 degrees, 45 degrees and 60 degrees.

The ladder model is analyzed using the numerical method is software Ansys, starting from the stages of defining the element type, installing the constraints as shown in Fig. 13.

The ladder model with a vertical bending moment using the multi point constraint (MPC) method, which is given a pedestal at both ends of the ladder model. the end of the ladder shaft is restrained in the x, y and z translational directions and the end of the ladder where the cutter is in the x and y translational bridle. All directions of free rotation are given a moment at one end of the support as shown in Fig. 14.

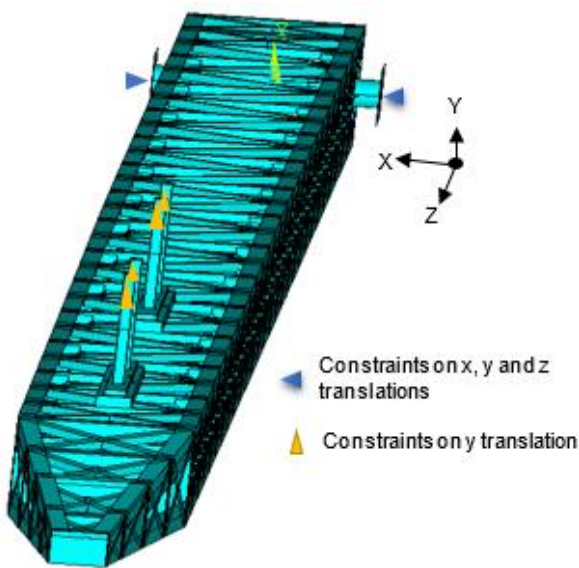


Figure 13. Position of restraint on ladder

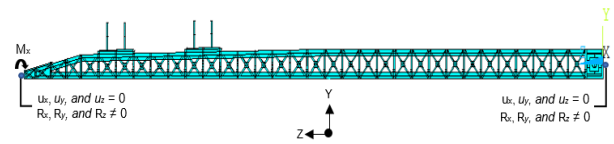


Figure 14. Restraint on the longitudinal strength of the ladder using the Multiple Point Constraint (MPC) method

Table 1. Variation of load increase

Load variation %	Pipe weight x 10 ⁵ N	Cutter weight x 10 ⁵ N	Torque moment x 10 ⁸ Nmm
100	1.42	0.57	0.67
200	2.83	1.14	1.34
300	4.25	1.71	2.01
etc.	etc.	etc.	etc.

After being restrained, the loading and the expected results of the analysis will of course know the stresses and deformations that occur on the ladder after being given a load and also know the highest stress that the ladder can withstand before collapsing.

3. Results and Discussion

3.1. Ladder Structure Loading

Based on the calculation of the load that works on the ladder, the pipe load is 1.42 x 10⁵ N, the cutter weight is 5.6 x 10⁴ N and the cutter torque is 6.71 x 10⁷ Nmm and will vary the load increase every 100% from the initial load until the collapse stress can be summarized in Table 1.

To obtain the value of the vertical bending moment during hogging and sagging conditions for the ladder model, the bending moment will be varied to what extent the ladder construction is able to withstand the moment. In the moment variation experiment, every 100% increased from the initial moment of 5 x 10⁷ Nmm until the stress collapses is given in Table 2.

3.2. Ladder Tilt Angle Variation

In this condition, the ladder angle is varied starting from 0°, 30°, 45°, and 60° with the angle measured between the position of the ladder's slope and the horizontal line of the water surface as shown in Fig. 15.

Table 2. Variation of increase in bending moment.

Bending Moment Variation %	Hogging x 10 ⁸ Nmm	Sagging x 10 ⁸ Nmm
100	0.5	-0.5
200	1.0	-1.0
300	1.5	-1.5
etc.	etc.	etc.

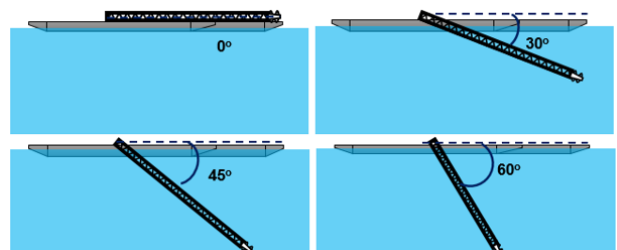


Figure 15. Ladder tilt angle variation

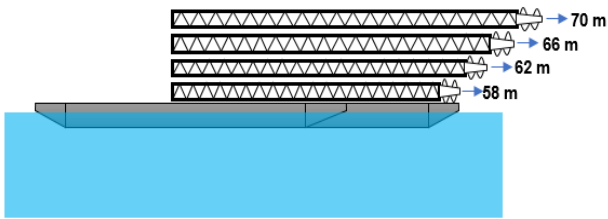


Figure 16. Ladder length variation

3.3. Ladder Length Variation

In this condition, each angle variation such as in the 42 ladder length is varied starting from the initial length of the ladder, namely 58 meters, 62 meters, 66 meters and 70 meters, each length increase is followed by angle variations as shown in Fig. 16.

After calculating the load, then the ladder strength analysis is carried out by looking at the structural response, namely changes in the shape of the ladder structure or shifts and stresses due to loads acting on the ladder such as pipe loads, cutter loads and torque moments due to cutter torque looking at the review points on ladder models.

3.4. Ladder Structure Analysis

a. Analysis of Ladder Structure due to Pipe Load, Cutter Load, and Cutter Torque

Some parts of the modeled structure will experience displacement (shift) when a load acts on it. The ladder model will be tested by giving each load that works on the ladder such as the shift in Fig. 17 due to cutter load, Fig. 18 due to pipe load and Fig. 19 cutter torque.

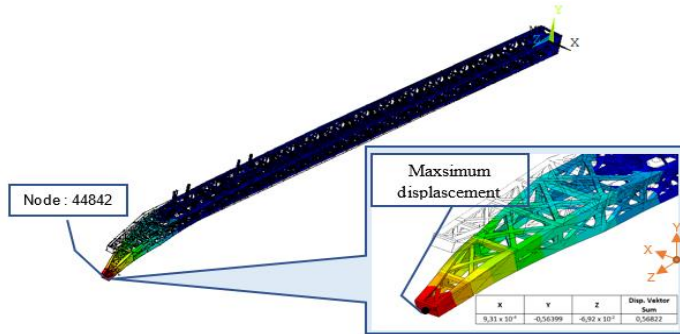


Figure 17. Displacement of x, y and z directions with a model length of 70 meters due to cutter load

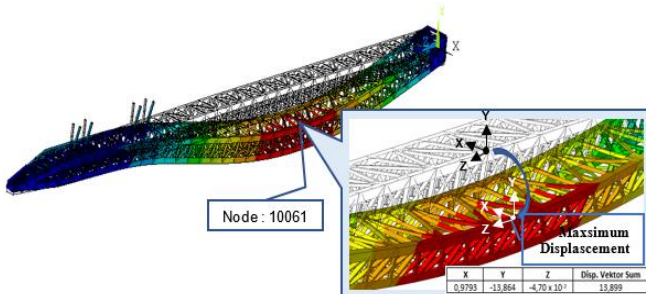


Figure 18. Displacement of x, y and z directions with a model length of 70 meters due to pipe load

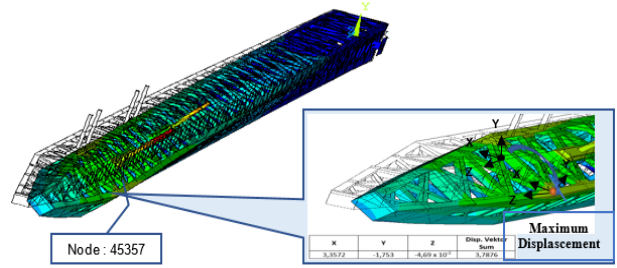


Figure 19. Displacement of x, y and z axes with a model length of 70 meters due to torsional moment

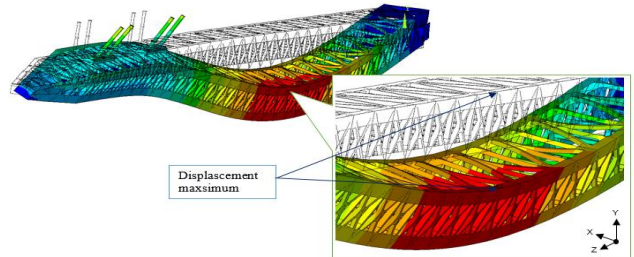


Figure 20. Displacement of x, y and z axes with a model length of 70 meters for all loads

Of the three load experiments, the maximum shift due to the pipe load that occurs in the column along the 42 meters from the shaft ladder is 13.86 mm, while the cutter load shifts 0.57 mm and the cutter torque shifts 3.79 mm. and if the load works simultaneously can be seen in Fig. 20.

Maximum displacement for all directions x, y and z is 14.29 mm for a model length of 70 meters with a shift value in the x direction is 2.22 mm for the y direction is 14.19 mm and the z direction is 0.38×10^{-1} mm. Thus the largest displacement occurs in the y direction of 14.19 mm.

Each ladder length is given the same load starting from 58 meters, 62 meters, 66 meters and 70 meters with each increase in ladder length varying the angle starting from the angle of 0° , 30° , 45° , and 60° . The deflection results show that at a ladder length of 58 m for an angle of 0° of 5.06 mm while at an angle of 60° with the same ladder length it has a deflection value of 2.65 mm. For a ladder length of 70 meters with an angle of 0° has a deflection value of 14.28 mm and an angle of 60° has a deflection value of 7.28 mm as shown in Fig. 21.

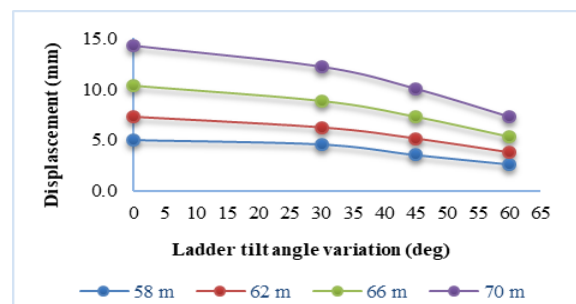


Figure 21. Curve of variation of ladder angle with displacement at each increase in ladder length

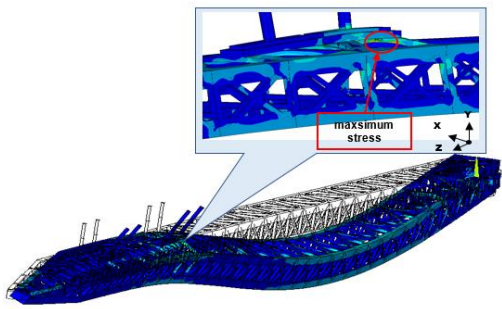


Figure 22. Behavior and distribution of working stress on ladder construction with a model length of 70 meters

Based on Fig. 21 The longer the ladder, the greater the displacement value with an average percentage increase of 29.24% from the initial shift and the greater the slope angle of the ladder the smaller the shift with an average reduction of 19.9% from the initial displacement.

Stress is the magnitude of the force exerted by the molecules on the cross-sectional area as shown in Fig. 22.

Based on Fig. 22 it can be seen that the maximum stress occurs in the strut area of the pulley foundation which functions to move up and down the ladder. Strut withstands the greatest load so that it gets a maximum stress of 56.88 N/mm². Each length of the ladder is given the same load, starting from the length of the ladder 58 meters, 62 meters, 66 meters and 70 meters with each increase in the length of the ladder varying the angle starting from the angle of 0°, 30°, 45°, and 60° so that the stress results can be seen. in Fig. 23.

Based on Fig. 23 The longer the ladder, the greater the stress value with an average percentage increase of 29.24% from the initial stress and the greater the slope angle of the stress ladder decreases with an average reduction of 19.9% from the initial stress.

b. Analysis of Ladder Structure in the Pulley Area

Due to pipe load, cutter load and cutter torque, based on the results of the analysis, the maximum stress occurs in the pulley area. To facilitate the identification of each component of the construction as shown in Fig. 24.

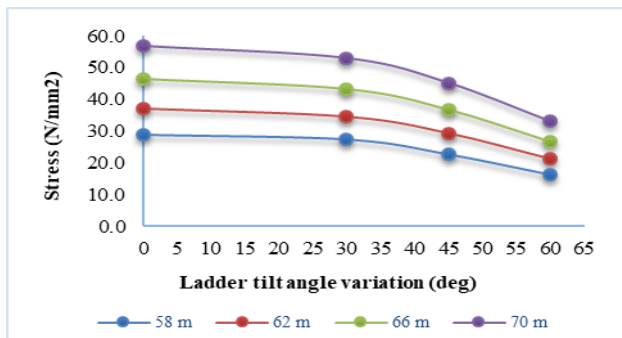


Figure 23. Variation curve of ladder angle with stress (von mises stress) at each increase in ladder length

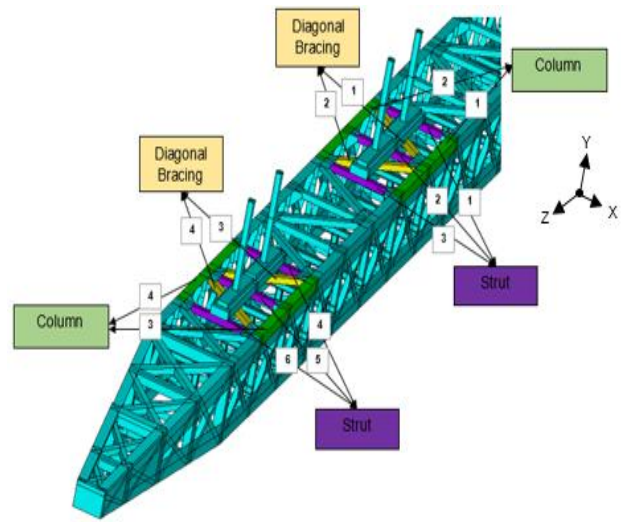


Figure 24. Components of the ladder structure to be analyzed

Based on Fig. 24, it can be seen the division of structural components in the pulley foundation area which consists of 6 units of strut components, 4 units of diagonal Brace components and 4 units of column components. After the analysis, it is divided into two areas as shown in Fig. 25.

Based on Fig. 25 the maximum stress occurs at strut number 1. The strut component has the maximum maximum stress right at strut 1 which has a major role in holding the rope due to the pipe load and the ladder construction along 49 meters.

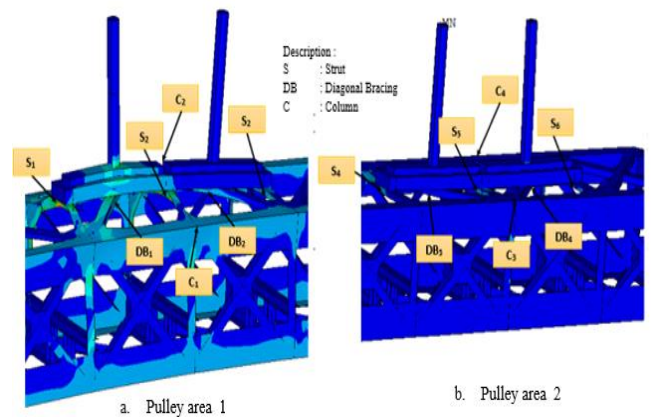


Figure 25. Behavior and distribution of working stress on ladder structure (pulley 1) foundation area, (pulley 2) foundation area

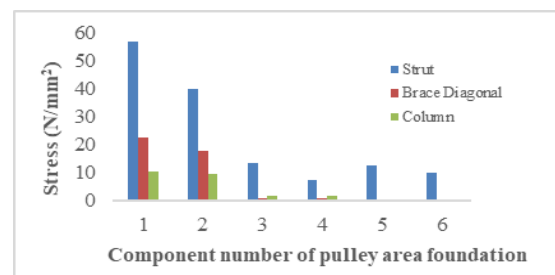


Figure 26. Relationship between stress and structural components of the pulley foundation area

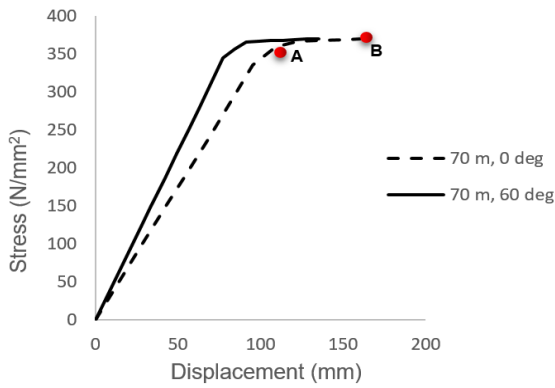


Figure 27. The curve of the relationship between stress and displacement

Based on Fig. 26 the maximum stress occurs in strut number 1. The strut component has the maximum stress that is right at strut number 1 which has a big role in holding the rope due to the pipe load and the 49 meter long ladder construction.

c. Ultimate Strength

Ultimate strength is the stress at the highest level that a test object can withstand before it breaks. In the experiment the model will be tested by increasing the load variation until the model collapses. With variations in the increase in the load that works on the ladder including the pipe load, cutter load and cutter torque, there is a maximum stress on strut 1. So each load is varied every 100% increase from the initial load until strut number 1 collapses so that from the variation of the load the limit strength is obtained. like in Fig. 27.

From the results of the experiment, at an angle of 0 degree ladder the strut will collapse 60 degrees and at an angle of 60 degrees it will shift 130.6 mm. so from Fig. 27 it can be seen that the greater the slope angle of the ladder, the smaller the displacement value.

The longitudinal strength of the ladder was analyzed using the Multiple Point Constraint (MPC) method with variations in vertical bending moment. The end of the ladder shaft is on the reins of the x, y and z axes. Then the end of the ladder where the cutter is on the reins in the x and y directions, all axes of rotation are freed. one end is given a moment. Then we will review the maximum displacement that occurs in the model in the hogging and sagging conditions as shown in Fig. 28.

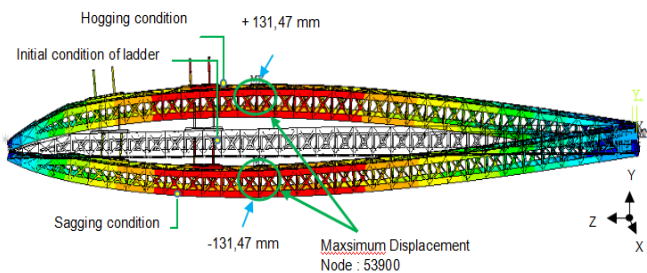


Figure 28. Displacement the limit strength a ladder with a length of 70 meters and an angle of 0 degrees on the y-axis due to hogging and sagging

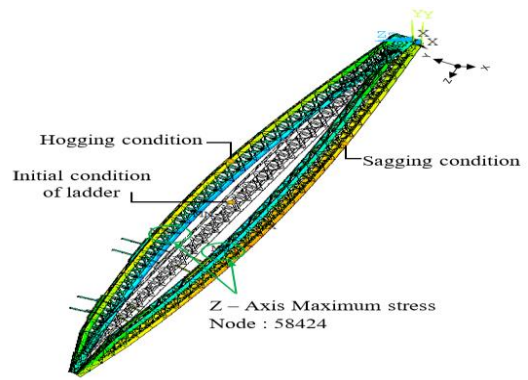


Figure 29. Behavior and distribution of limiting stress on a ladder length of 70 meters and a slope angle of 60 degrees the z-axis due to hogging and sagging

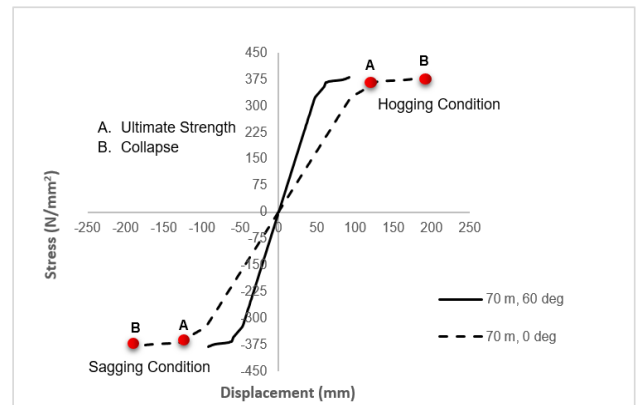


Figure 30. Curve of the relationship between stress and bending moment variations in hogging and sagging conditions

Based on Fig. 28 The maximum displacement at an angle of 0 degrees occurs in the column with a distance of 42 meters from the end of the ladder shaft which will collapse when it receives a moment of 2.89×10^9 Nmm with a maximum shift of 131.73 mm. Stress generated at an angle of 60 degrees can be seen in Figure 29.

Based on Fig. 29 The maximum stress at an angle of 60 degrees occurs at the end of the ladder which is restrained and will collapse when it receives a moment of 1.45×10^9 Nmm with a maximum shift of 66.17 mm from the initial position of the ladder before it is loaded.

Based on Fig. 30 it can be seen at the ladder tilt angle of 0 degrees for hogging and sagging conditions the limit of the bending moment that can be endured is 2.91×10^9 Nmm while at a slope angle of 60 degrees the limit of the bending moment that can be endured is 5.82×10^9 Nmm. so that for the same ladder length the greater the angle of inclination is inversely proportional to the value of the stress and displacement.

4. Conclusion

Based on the results the analysis the load acting on the ladder, namely pipe load, cutter load and cutter torque. The longer the ladder is directly proportional to the stress and displacement values produced with an average increase of 24.8% from the initial value and the greater the slope angle of the ladder is inversely proportional to the stress and displacement values produced with an average decrease of 16.6% from the

initial value. At an angle of 0 degrees the strut ladder will collapse when shifted 160.2 mm. 60 degree angle of collapse when receiving a displacement of 130.36 mm. Based on the results of the analysis of the strength of the longitudinal ladder structure in the conditions of hogging and sagging, a distance of 42 meters from the ladder shaft experienced a maximum shift in the column of 131.73 mm from the initial position before being loaded. While at an angle of 60 degrees it will collapse when receiving a 0.49% decrease from the initial shift of the 0 degree angle.

References

- [1] PT. Timah (Persero) Tbk, Kundur, Riau Islands, 2020.
- [2] R. A. Parisher and R. A. Rhea, *Pipe drafting and Design Second Edition*. Boston, Oxford, Auckland, Johannesburg, Melbourne, New Delhi: Gulf Professional Publishing, 2002.
- [3] Y. Feng *et al.*, "Research progress and prospect of key technologies for high-strain line pipe steel and pipes," *Nat. Gas Ind. B*, vol. 8, pp. 146–153, 2021.
- [4] C. G. Salmon and E. J. Jhon, *Steel Structures, Design and Behavior*. Jakarta, Indonesia: Erlangga, 1991.
- [5] M. Z. Muis Alie, "Residual Strength Analysis of Asymmetrically Damaged Ship Hull Girder Using Beam Finite Element Method," *Makara J. Technol*, vol. 20, no. 1, 2016.
- [6] Anwar, "Effect of Brace on Helideck Structure Leg Strength in Withstanding Helicopter Emergency Landing Loads," Hasanuddin University, 2018.
- [7] A. Setiawan, *Steel Structure Planning*. Jakarta: Erlangga, 2002.
- [8] D. B. Marghitu, *Mechanical Engineer's Handbook*. Academic Press, 2001.
- [9] L. D. Schodek, *Structure*. Bandung, Indonesia: PT Rafika Aditama, 1998.
- [10] Biro Klasifikasi Indonesia, "Domestic Stomach Guidelines Volume 1," Jakarta, 2019.
- [11] J. M. Gere and B. J. Goodno, *Mechanics of Materials Seventh Edition*. 2009.
- [12] DNV GL, "Rules for Classification: Ships, Pt.3 Ch.5. Hull Girder Strength," 2017.
- [13] P. Rigo and E. Rizzo, "Analysis and Design of Ship Structure," 2003.
- [14] T. Yao and M. Fujikubo, *Buckling and Ultimate Strength of Ship and Ship-like Floating Structures*. Elsevier, 2016.
- [15] M. Z. Muis Alie, D. Ra masari, T. Rachman, and R. Adiputra, "Effects of Collision Damage on the Ultimate Strength of FPSO Vessels," *Makara J. Technol*, vol. 24, no. 1, 2020.
- [16] M. Shama, *Buckling of Ship Structures*. Springer, Verlag Berlin Heidelberg, 2013.
- [17] Ship Structure Committee, "Survivalability of Hull Girder in Damaged Condition," Washington DC, 2015.

Numerical and Experimental Analyses of Track Shoe Patterns for Vehicle on Sandy Terrain

Ignatius Pulung Nurprasetyo^{a,*}, Wiryawicak^b, Siti Zulaikah^c, Bentang Arief Budiman^d

^aFaculty of Mechanical and Aerospace Engineering, Institut Teknologi Bandung. Email: ipn@ftmd.itb.ac.id

^bFaculty of Mechanical and Aerospace Engineering, Institut Teknologi Bandung. Email: wiryawicak@yahoo.com

^cNational Center for Sustainable Transportation Technology. Email: siti.zulaikah@my.sampoernauniversity.ac.id

^dFaculty of Mechanical and Aerospace Engineering, Institut Teknologi Bandung. Email: bentang@ftmd.itb.ac.id

Abstract

A track is a vehicle propulsion system that consists of a continuous band of chains connected with track shoes or may be entirely made of rubber. The track system is still commonly used on various vehicles, including bulldozers, excavators, tanks, and tractors, and has recently been used in lunar expedition vehicles. A tracked vehicle is mainly designed to provide better mobility in rough, uneven, or slippery terrain. The main component of the track system is track shoes or so-called grousers. This track shoe geometry will determine the tractive performance of the vehicle. If an incorrect shape is used, the excavator will most likely slip. The previous study approached this traction problem by using the semi-empirical method. However, until now, the track geometry and traction relation are still unclear. This research focuses on the effects of track shoe geometry on tractive performance and vehicle climbing ability. The analysis was mainly conducted with a DEM (Discrete Element Method) simulation. The result from the experimental test is also confirmed using a small-scale RC prototype on simulated terrain with different slope variations. It is proven that the grouser height directly affects the climbing performance of tracked vehicles. A higher grouser height proves to be better at a higher inclination slope. However, for a low inclination angle, the flattened track was better. The traction result from the EDEM simulation also yields a similar result. However, higher usable traction means more friction is generated; therefore, the track with higher traction also takes more energy to cover the same distance.

Keywords: Sandy terrain vehicle; track shoe; vehicle tractive performance

1. Introduction

Since the early 20th century, tracked vehicles have been developed for various off-road environments such as agriculture, construction, military, particular logistics, and even space exploration [1]–[3]. Tracks system can give excellent ground holding capability and mobility through very rough terrain better than wheels [3]–[6]. Wide tracks help distribute the vehicle's weight over a large area, decreasing the ground pressure, thus preventing it from sinking in sandy or soft ground [3]. The tractive performance of a tracked vehicle is influenced by how the track interacts with the soil, which strongly depends on the shape of the track, soil composition, and soil properties [7], [8].

There have been previous studies regarding the effect of track shape on tractive performance. For instance, Wang et al. examined the influence of grouser thickness and grouser height on traction by using a grouser shoe model [9]. They discovered that the optimal grouser height

depended on the composition of the soil and the moisture content of the soil. The complex terramechanics problem was complicated to be solved fully theoretically [10], [11]. Therefore, the prediction of vehicle traction on soft ground has been investigated using an empirical and semi-empirical method. Several research studies have demonstrated the reasonable accuracy of semi-empirical techniques in traction prediction [12]–[15]. The Bekker traction model equations use the relationship between specific physical soil characteristics and shearing strength to predict off-road vehicle mobility [15], [16]. Bekker considers wheels and tracks as simple loading surfaces with similar forms but different lengths and widths. The analogy was extrapolated between soil shear produced by laboratory crawlers to track vehicles and does not consider the grouser shape and vehicle driving parameters.

With the rapid development in computer technology and computational methods, people have come up with other methods that can be used, namely, the discrete element method (DEM) [15], [17]. DEM simulation uses a multi-particle simulation that treats each particle individually [18]. Particle parameters such as shape, size, density, Young's Modulus, Poisson's ratio, coefficient of restitution, and friction coefficient can be easily specified

*Corresponding author.

Jl. Ganesa No.10, Lb. Siliwangi, Coblong
Bandung, Jawa Barat, Indonesia
40132

to model a real-life problem. Recently, these methods have become more widely used in addressing soil-body contact problems [19], [20].

The main objectives of this research are to investigate the track shoe and soil interaction and determine how different track shoe geometry may affect the vehicle's performance, mainly the climbing ability as well as the traction of the vehicle, and to determine the optimum grouser height for a tracked vehicle on sandy terrain at various inclination slopes.

This research is expected to provide a better understanding of track vehicles, specifically track shoes, and how various parameters will affect the overall vehicle performance. The results from the experiment could serve as a reference for future EDEM experiments and help engineers in developing new track shoes for the future, as well as mechanics or users who are looking for a new track shoe.

2. Methodology

2.1. Discrete Element Method

Given that sand is composed of many small particles, this research was approached using computational analysis, which is EDEM software. The forces acting upon one piece of the track shoe and their interaction with the particles would be found. Beforehand, the geometry model was constructed using SolidWorks. Figure 1 shows the EDEM system, including sand particles, a piece of track shoe, and a box. The gravitational force is in the z-direction, and the weight of the track shoe was assumed to be the weight of the small-scale RC excavator. It is 16 N divided by the total number of track shoes in direct contact with the sand, which is 42 tracks.

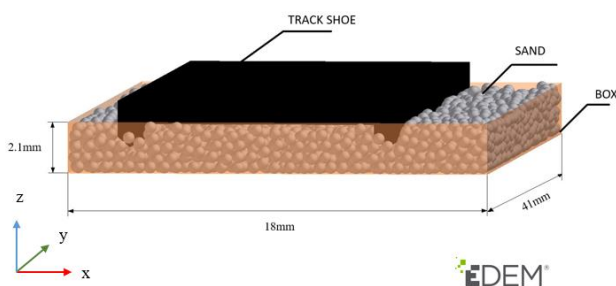


Figure 1. EDEM simulation

Table 1. Sand properties

Bulk Material Properties	Magnitude	Unit
Poisson's Ratio	0.25	-
Solid Density	1460	kg/m ³
Shear Modulus	69000000	Pa
Coefficient of Restitution	0.64	-
Coefficient of Static Friction	0.6	-
Coefficient of Rolling Friction	0.4	-
Particle Diameter	0.2604	mm
Total Particle	9000	particle

EDEM software has several particle shape libraries, including sphere, dual sphere, triple sphere, and tetrahedral. None of these could represent the shape of the real sand that is not uniform. Thus, the sand was depicted with a spherical particle as the simplest and fastest approach for this simulation. After choosing the shape, several particle parameters must be inputted into the program. Due to sand properties varying depending on its composition, some of the properties listed in Table 1 were assumed to be well-graded sand except for the particle diameter and density measured directly.

Figure 2a shows how the grain size of sand can be approximated by using a simple digital microscope with 50 times magnification. The sand is highlighted with a black line. Before starting the experiment, the pixel size of 1 mm was measured for the reference point and calculated to be 394 pixels. By the effective diameter method, the average sand grain size was calculated to be 102.6 pixels and then converted to mm, generating a grain size of 0.2604 mm. Figure 2b shows the outer and inner diameters approaching the sand diameter.

The discrete element method principle portrays the soil (terrain) as an assemblage of several discrete elements. Sand has almost no cohesion when water is not present; thus, dry sand using the discrete element method can be approached. Figure 2c depicts one circular element in the EDEM plane.

EDEM allows analyzing the track and sand interaction by examining the mechanical interactions between the track and adjacent elements and those between the contacting elements. Elements in contact with the track surface receive contact forces from the track. Elements not in contact with the track surface receive contact forces from other contacting elements. The magnitudes of the contact forces are assumed to be related to the relative displacement and relative velocity of the contacting elements, dependent upon the model for the mechanical property of the elements used.

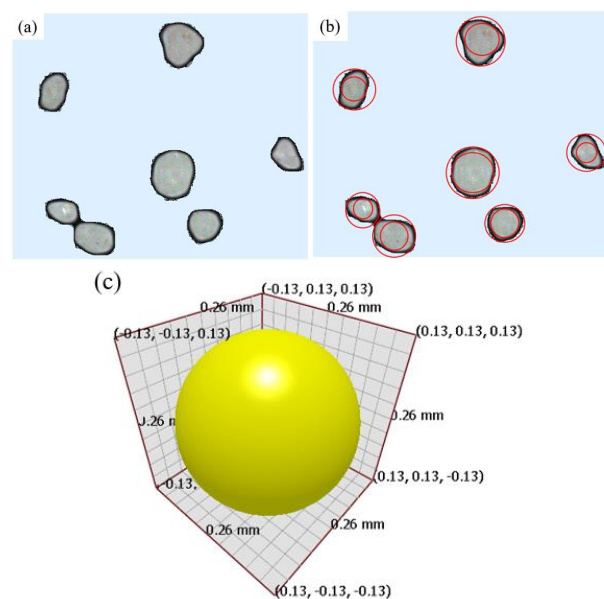


Figure 2. (a) Captured grains of sand under microscope; (b) Inner and outer diameter measurement under microscope; (c) Representative ball model for grains of sand in DEM

2.2. Experimental Method

The experiment setup mainly included a 1:14 scale RC excavator, digital weight scale, spirit level, digital Avometer, sand, video camera, leveler, measuring tape, tripod, and plywood. The experiment was conducted by running a small-scale RC excavator on well-graded sand. Beforehand, three different track setups were created by modifying the grouser height to simulate the three different grouser geometries. The track was produced by modifying the standard track using resin casting. For each setup, the performance would be compared to which one is the best in terms of traction and climbing ability.

Due to equipment and tool limitations, only three tracks were used in this experiment (Fig. 3). The first setup was the standard track obtained from the manufacturer without any modification, which used plastic material with clear concave and convex surfaces in their track shoes. The second setup was created to simulate low grouser height. This grouser has the space in between that is filled with resin, generating flatter and smoother surfaces. Lastly, the third setup was created to simulate high grouser height. A small stick of wood as wide as the track size was fixed to the track's surface using resin as its adhesive, generating a higher grouser height but still maintaining the stiffness.

For all three tracks, the weight was measured using a digital scale. As a result, setup 1 has the lightest weight at only 38 grams each; setup 2 has a weight of 41 grams each; and setup 3 has the heaviest weight at 53 grams each. Even though this weight difference is slight, it is predicted to still affect the RC excavator's performance.

All three setups were tested with the excavator on a sandy surface inside a plywood box. This box is custom-made and has dimensions 110 cm long, 40 cm wide, and 7.5 cm in height. Even though the sand only fills up to 75% of the box's maximum capacity or around 5 cm. Afterward, on the sides of the box, a measuring tape is attached to help monitor the distance traveled by the excavator. Figure 4a shows the main experiment apparatus used in this research.

For better accuracy, the sand was leveled, and the bumpiness was tested with a spirit level for each run to ensure no bumps or holes on the sand. The test was initially performed with slopes of 10°, 20°, and 30°. However, the excavator always failed or became stuck at the 30° slopes, as shown in Fig. 4b. As a result, the increment was changed to 5°. The excavator is run through uphill and downhill set configurations with 0°, 13°, 18°, and 23° slopes for each setup. All data is captured with the video camera.

All the grouser parameters of this work were defined as follows. The model used W of 16 N, L of 1 cm, h of 0.1, 0.3, and 0.5 cm, t of 0.2 cm, b of 4 cm, and λ of 0.1. The grouser length, vertical load, thickness, width, and thickness ratio are fixed due to limitations in manufacturing. In other words, this work focuses more on the effect of grouser height. Since the excavator motor speed cannot be precisely adjusted and only depend on the battery condition. Hence, the battery voltage was monitored for every run to ensure the speed was not affected by the battery.



Figure 3. Three different track setups: (a) Setup 1; (b) Setup 2; (c) Setup 3

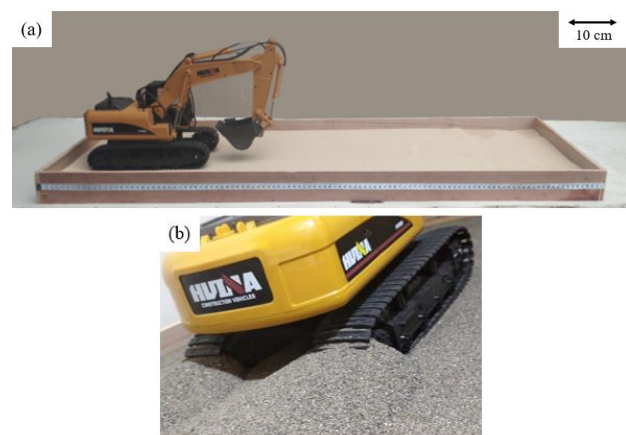


Figure 4. (a) Experimental apparatus; (b) Example of sinking excavator

3. Result and Discussion

3.1. Climbing Ability

Overall, three different setups (track profiles) were tested in this research. A video camera was used and placed on the side of the apparatus using a fixed tripod. This video camera can take videos with a resolution of 1080p at 24 FPS (frames per second). Afterward, the video would be processed in video editing software. The video editing software used is Adobe Premiere due to its user interface ease and its capability to process various video formats. Subsequently, the unnecessary frame is removed in this software, leaving only the part when the excavator starts moving until the excavator touches the other side of the box. Therefore, the timecode for every run can be obtained. Timecode values are a way of numbering frames in the video. Standardized by SMPTE (Society of Motion Picture and Television Engineers), video timecode is usually represented as an hour, minute, second; then, each

frame number is separated by a colon (:). The timecode is then converted to seconds by dividing the frames by 24. Since the distance traveled by the excavator, the speed in cm/s can be obtained.

Figure 5 is the bar graph obtained from the experimental results. In this graph, the speed for every setup and every inclination angle can be observed. The graph shows that the speed difference is relatively small (<5 cm/s). In addition to speed data, how steep the excavator’s ability to climb also can be found by investigating the angle of failure or the angle at which the excavator cannot climb anymore. The failure angles for setups 1, 2, and 3 are 25.93°, 24.87°, and 28.20°, respectively. It can be seen that for track shoe of setup 2, the speed difference of downhill and uphill is highest than other setups. This can occur because the setup 2 does not have sufficient grip to avoid slip between the track shoe and sand.

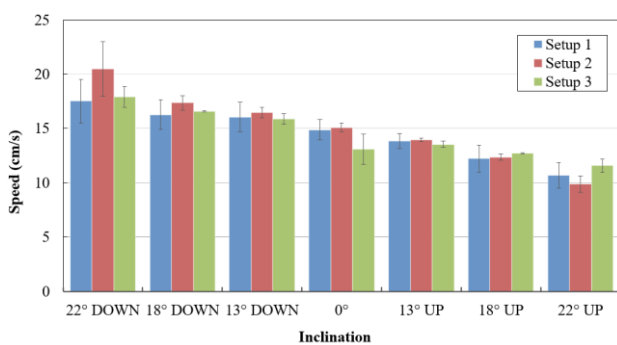


Figure 5. Speed graph

3.2. Slip ratio

The slip ratio is a non-dimensional value calculated from the motor revolution and actual distance traveled. By the slip ratio equation for a tracked vehicle, the slip ratio for each setup is found. The slip ratio value lies between zero (no slippage) and one (total slippage). In this research, the slip ratio was calculated using speed at the steepest inclination (22°), and the RPM was calculated from the total wheel rotation per minute. Table 2 is the result of the slip ratio.

The slip ratio for downhill is negative because the excavator travels faster than the wheel rotation itself. Since the slip ratios are not zero, the excavator experiences slip phenomena.

Table 2. Slip ratio

	Setup 1	Setup 2	Setup 3
r (cm)	2.4	2.4	2.4
h (cm)	0.3	0.1	0.5
RPM	55	55	55
ω (rad/s)	5.76	5.76	5.76
Speed uphill (cm/s)	12.05	10.73	12.28
Speed downhill (cm/s)	19.85	22	18.99
Slip ratio uphill	0.225	0.255	0.265
Slip ratio downhill	-0.276	-0.528	-0.137

3.3. EDEM Results

There are three main phases in the EDEM experiment. The first phase was the particle generation phase; the total number of particles was set at 9000 particles. The second phase was the moving phase. The track shoe started moving with a starting velocity of 0.09 m/s and 0 m/s² acceleration. Finally, the settling phase was where the track stopped moving and the particles settled. The total time from start to finish was 0.14 s. Afterward, the force in the x-direction is plotted on a graph. Since the excavator is supported by 42 track shoes when stationary, the forces for one shoe are multiplied by 42 to estimate the traction produced. The model of track shoes is made as close as possible to make the result comparable to the experiment conducted prior.

Figure 6a depicts setup 1 of track shoe and sands particles in the EDEM plane. Figure 6b depicts the sand compressive force contour from the isometric view. Figure 6c depicts the sand compressive force contour from the top view.

Figure 7a depicts setup 2 of track shoe and sands particle in the EDEM plane. Figure 7b depicts the sand compressive force contour from the isometric view. Figure 7c depicts the sand compressive force contour from the top view.

Figure 8a depicts setup 3 of track shoe and sands particle in the EDEM plane. Figure 8b depicts the sand compressive force contour from the isometric view. Figure 8c depicts the sand compressive force contour from the top view.

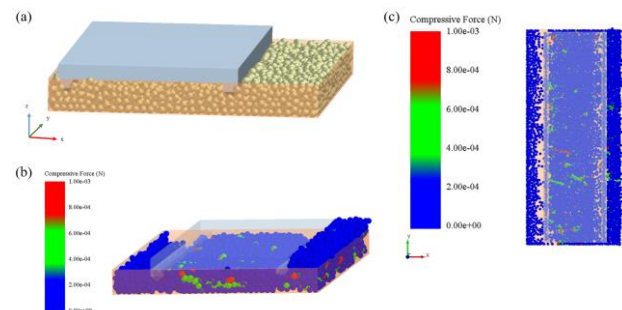


Figure 6. (a) EDEM setup 1; (b) Compressive force of EDEM setup 1; (c) Pressure contour of setup 1

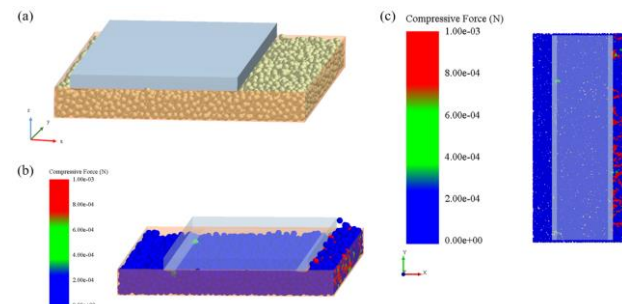


Figure 7. (a) EDEM setup 2; (b) Compressive force of EDEM setup 2; (c) Pressure contour of setup 2

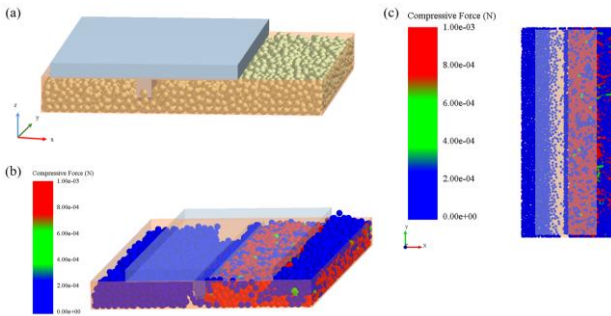


Figure 8. (a) EDEM setup 3; (b) Compressive force of EDEM setup 3; (c) Pressure contour of setup 3

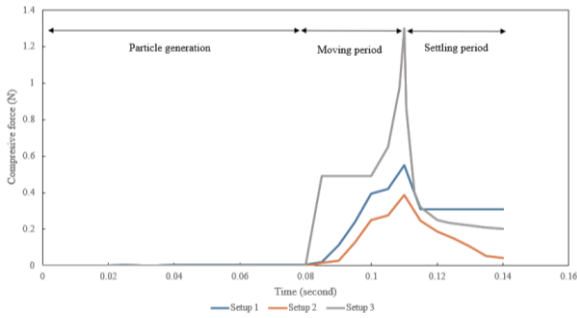


Figure 9. Plot of compressive force

The plot of Fig. 9 is the result of all EDEM. The x-axis represents time in second, and the y-axis represents the compressive force in Newton.

According to Fig. 9, the maximum force of setups 1, 2, and 3 are 0.549 N, 0.388 N, and 1.30 N, respectively. Then, by multiplying each of those results by 42, the final forces of setups 1, 2, and 3 are 23.1 N, 16.29 N, and 54.6 N, respectively. The whole set of the results is listed in Table 3, showing that setup 3 produced the highest traction force. Some errors probably occurred when it was compared to the actual traction.

3.4. Work Calculation

The excavator is assumed to move uphill with force equal to the total traction force obtained from the EDEM simulation. Then, the required work for each setup could be found if the excavator climbed the same 110 cm-long hills. To find the work, the formula is:

$$W = F \times s \tag{1}$$

Where W is work, F is force, and s is the distance traveled. Based on Fig. 10, the resultant force is traction force subtracted by $w \sin \theta$, and the distance is the sandbox length.

Table 3. Traction result

Setup	Max. compressive force (N)	Total traction (N)	Change (%)
1	0.55	23.1	Baseline
2	0.388	16.29	-29.48
3	1.3	54.6	136.36

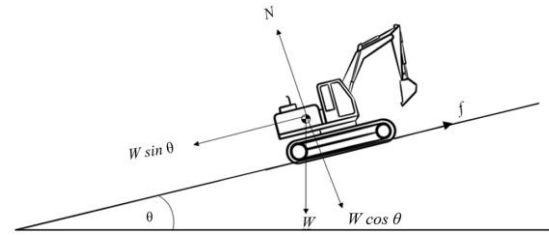


Figure 10. FBD of excavator

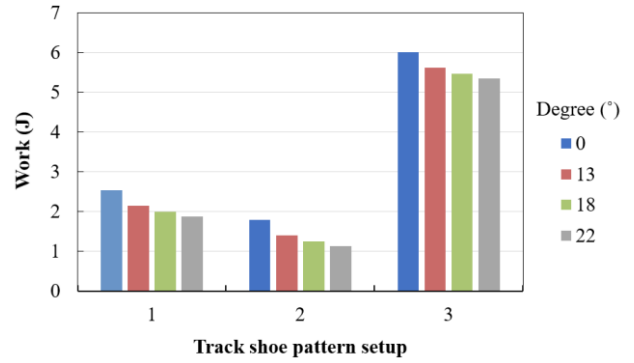


Figure 11. Work excavator

This data from the work calculation for each inclination is then plotted in Fig. 11. This graph can provide a general idea about the work for each track configuration. Although this data does not represent the actual work performed by the excavator, it is expected that the result will be as close as possible. Moreover, assuming no slip occurs, the maximum work done by the excavator can be obtained and given to propel the excavator forward.

3.5. Sand Pattern

The photos of the sand pattern for every run have been taken as a comparison. As shown in Fig. 12, there was a variety of different patterns. The track with no trailing lines on the sides indicates that the track is not slipping, as depicted in Fig. 12a. Additionally, the pattern with no-slip occurred also showed that the track pattern is very clear and does not overlap with the adjacent track shoe. On the other hand, as depicted in Fig. 12b, lines formed on the sides of the track, indicating that slipping has occurred. From the setup configuration, setup 3 leaves a deeper penetration compared to two other setups; meanwhile, setup 2 slipping lines are more obvious compared to two other setups.

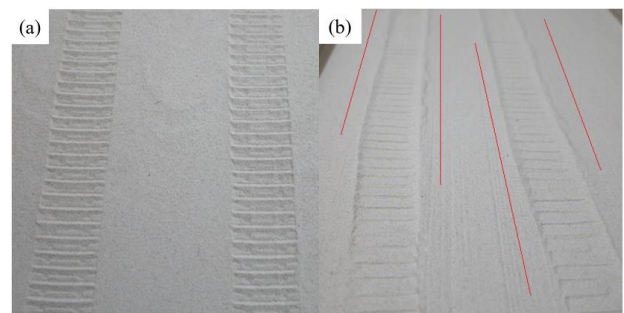


Figure 12. (a) Track pattern without slipping occurred; (b) Track pattern with slipping occurred

4. Conclusion

This research study has performed the simulation and experiment of track shoes on sandy terrain. The result shows that changing the grouser geometry, especially the grouser height, helps the excavator climb faster at a higher inclination slope greater than 18 degrees, while the lower inclination slope of fewer than 18 degrees does not contribute much or even slows the speed down slightly. A higher grouser height also demonstrates a greater climbing ability with the steeper hill of 28 degrees compared to 25 degrees from the standard track and 24 degrees from the flat track. EDEM simulation yields a similar result for a higher grouser height (setup 3) has 136% better traction force than the standard track (setup 1), meaning that setup 3, assuming no slippage, requires more energy to cover the same distance. Therefore, the tracked vehicle operated on sandy terrain with a steep slope would perform better when applying higher grouser height; meanwhile, applying flat or lower grouser height is suggested only when a tracked vehicle operated in flat terrain.

References

- [1] G. Ferretti and R. Girelli, "Modelling and simulation of an agricultural tracked vehicle," *J. Terramechanics*, vol. 36, no. 3, pp. 139–158, 1999.
- [2] Z. Hryciów and P. Rybak, "Numerical research of the high-speed military vehicle track," in *AIP Conference Proceedings*, 2019, vol. 2078, no. 1, p. 020029.
- [3] J. T. Cook, L. E. Ray, and J. H. Lever, "Mobility Enhancement of Heavy-Duty Tracked Vehicles Under Load Using Real-Time Terrain Characterization, Traction Control, and a Towing Winch," *J. Dyn. Syst. Meas. Control*, vol. 141, no. 7, 2019.
- [4] S. A. Shaikh et al., "Effect of grouser height on the tractive performance of single grouser shoe under different soil moisture contents in clay loam terrain," *Sustainability*, vol. 13, no. 3, p. 1156, 2021.
- [5] T. Nabaglo, J. Kowal, and A. Jurkiewicz, "Construction of a parametrized tracked vehicle model and its simulation in MSC.ADAMS program," *J. Low Freq. Noise, Vib. Act. Control*, vol. 32, no. 1–2, pp. 167–173, 2013.
- [6] Y. Yang, T. Cai, and X. Xu, "Track Design of Track-Wheel Transport Vehicle and Strength Analysis of Important Components," in *InIOP Conference Series: Materials Science and Engineering* 2020, 2020, vol. 782, no. 2, p. 022058.
- [7] Z. Ding, Y. Li, and Z. Tang, "Theoretical Model for Prediction of Turning Resistance of Tracked Vehicle on Soft Terrain," *Math. Probl. Eng.*, vol. 2020, 2020.
- [8] M. J. Dwyer, "The tractive performance of wheeled vehicles," *J. Terramechanics*, vol. 21, no. 1, pp. 19–34, 1984.
- [9] X. L. Wang, N. Ito, K. Kito, K. Sato, and M. Yamashita, "Studies on Grouser Shoe Dimension for Optimum Tractive Performance (Part 3) Comparison of predictive and experimental traction of track's grouser," *J. Japanese Soc. Agric. Mach.*, vol. 65, no. 5, pp. 64–69, 2003.
- [10] E. Leflaive, "Mechanics of wheels on soft soils—A method for presenting test results," *J. Terramechanics*, vol. 3, no. 1, pp. 13–22, 1966.
- [11] S. Taheri, C. Sandu, S. Taheri, E. Pinto, and D. Gorsich, "A technical survey on Terramechanics models for tire–terrain interaction used in modeling and simulation of wheeled vehicles," *J. Terramechanics*, vol. 57, pp. 1–22, 2015.
- [12] D. Gee-Clough, M. McAllister, G. Pearson, and D. W. Evernden, "The empirical prediction of tractor-implement field performance," *J. terramechanics*, vol. 15, no. 2, pp. 81–94, 1978.
- [13] M. G. Bekker, *Introduction to terrain-vehicle systems, part i: The terrain, part ii: The vehicle*. Michigan Univ Ann Arbor, 1969.
- [14] J. Y. Wong, *Terramechanics and off-road vehicle engineering: terrain behaviour, off-road vehicle performance and design*. Butterworth-heinemann, 2009.
- [15] A. Nicolini, F. Mocera, and A. Soma, "Multibody simulation of a tracked vehicle with deformable ground contact model," *Proc. Inst. Mech. Eng. Part K J. Multi-body Dyn.*, vol. 233, no. 1, pp. 152–162, 2019.
- [16] G. R. Gerhart, "The bekker model analysis for small robotic vehicles," *SAE Trans.*, pp. 317–324, 2004.
- [17] F. Mocera, A. Somà, and A. Nicolini, "Grousers Effect in Tracked Vehicle Multibody Dynamics with Deformable Terrain Contact Model," *Appl. Sci.*, vol. 10, no. 18, p. 6581, 2020.
- [18] S. Wangchai, "Numerical simulation of the flow of agricultural seeds inside a rotary drum dryer by DEM," in *IOP Conference Series: Earth and Environmental Science*, 2019, vol. 301, no. 1, p. 012048.
- [19] A. A. Tagar et al., "Finite element simulation of soil failure patterns under soil bin and field testing conditions," *Soil Tillage Res.*, vol. 145, pp. 157–170, 2015.
- [20] A. Yokoyama, H. Nakashima, H. Shimizu, J. Miyasaka, and K. Ohdoi, "Effect of open spaces between grousers on the gross traction of a track shoe for lightweight vehicles analyzed using 2D DEM," *J. Terramechanics*, vol. 90, pp. 31–40, 2020.

Modeling and Simulation of a Double-Stage Single-Phase Grid-Connected PV System

Channareth Srun^{a,*}, Phok Chrin^b, Sokchea Am^c, Bunthern Kim^d

^aMechatronics and Information Technology, Institute of Technology of Cambodia. Russian Federation Blvd, P.O. Box 86, Phnom Penh Cambodia. Email: nareth16npic@gmail.com

^bEnergy Technology and Management, Institute of Technology of Cambodia. Russian Federation Blvd, P.O. Box 86, Phnom Penh Cambodia. pchrin@gmail.com

^cEnergy Technology and Management, Institute of Technology of Cambodia. Russian Federation Blvd, P.O. Box 86, Phnom Penh Cambodia. sokchea_am@itc.edu.kh

^dEnergy Technology and Management, Institute of Technology of Cambodia. Russian Federation Blvd, P.O. Box 86, Phnom Penh Cambodia. Email: bunthern.kim9@gmail.com

Abstract

This paper presents the design model and simulation of a double-stage single-phase grid-connected PV system. This system includes an MPPT DC-DC boost power converter and a transformer-less single-phase DC-AC power inverter, which is connected to the power grid with an LCL filter. In the DC-DC boost converter, the Perturb and Observe algorithms are combined. The output voltage of the DC-DC converter is regulated by a proportional controller, and the DC/AC output voltage is synchronized with the grid. The grid current is controlled by a harmonic compensator and used to maintain its quality. The MATLAB-Simulink environment is used for the closed-loop simulation of the proposed setup. The simulation results are presented for various solar irradiance conditions and show that photovoltaic current is generated and matches the phase of grid voltage.

Keywords: Double-stage; Grid tie; MPPT; P&O algorithm; PV system

1. Introduction

Long-term policymakers believe fossil fuel-based traditional electricity generation is unsustainable. This has been one of the primary motivators for the extensive incorporation of renewable energy sources such as wind, solar photovoltaic (PV), hydropower, biomass power, geothermal power, and ocean power into public networks during the previous decade. Solar PV power output has continued to grow at a high rate among the major renewables in recent years, and it now plays a significant role in energy generation. Recently, most of the PV systems have been for residential applications. Therefore, single-phase grid-connected PV systems have been highlighted as a common configuration for residential PV applications in order to demonstrate the technology that will enable PV integration into the future hybrid energy grid [1].

Power electronics technology, particularly solar PV systems, has long been regarded as a critical facilitator for integrating additional renewable energy sources into the grid. The power electronics component of whole PV systems (i.e., power conversions) is responsible for converting clean and limitless solar PV energy into a

dependable and efficient form. As a result, a wide range of grid-connected PV power converters has been developed and marketed. The size and power of grid-connected PV systems, on the other hand, range from small-scale to large-scale PV power plants.

Residential applications typically employ single-phase systems with module and string converters [2]. One of the main drawbacks of single-stage PV topologies is that they are less efficient overall since the output voltage range of the PV panels/strings is constrained, especially in low-power applications (such as AC-module inverters). Due to a DC-DC converter that raises the PV module's voltage to a suitable level for the inverter stage, the double-stage PV system can get around this issue [3]. The main block diagram of a double-stage single-phase PV architecture is shown in Fig. 1.

The control mechanism suggested in [4] for single phase without a DC-DC converter. The internal current control loop and the external voltage control loop are the identical ones [5].

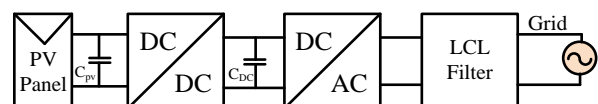


Figure 1. Block diagram of double-stage single-phase PV architecture

*Corresponding author. Tel.: +855-17-592-963
Phnom Penh, Cambodia, 12000

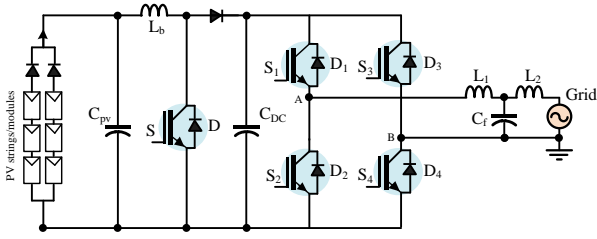


Figure 2. Double-stage single-phase PV scheme consisting of a boost converter and full-bridge inverter with an LCL filter

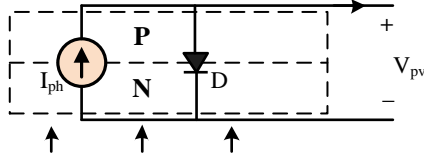


Figure 3. Ideal PV model

In this paper a double-stage PV system, the DC–DC converter also controls the MPPT of the PV panels, allowing for longer operation. A DC-DC converter and a full-bridge inverter are used in this double-stage PV technology.

Figure 2 illustrates a traditional double-stage single-phase PV system in which the leakage current must also be kept to a minimum. Including a boost converter will reduce total conversion efficiency. A single-phase grid-connected PV system's control goals may be classified into two categories: (1) PV-side control, which aims to optimize the power generated by PV panels; and (2) grid-side control, which is done on PV inverters and aims to meet power grid requirements.

2. System Model and Description

2.1. PV Array Model

Solar irradiance G , measured in W/m^2 , and temperature T , measured in degrees Celsius ($^{\circ}C$), are the two most important elements. Mathematically, the relationship between these two parameters and PV operational characteristics may be predicted. First, we look at the ideal model, which is depicted in Fig. 3 and includes the photocurrent source I_{ph} and a diode.

According to, the photocurrent I_{ph} in Eq. (1) is affected by both irradiance and temperature.

$$I_{ph}(G, T) = [I_{scn} + K_i(T - T_n)] \frac{G}{G_n} \quad (1)$$

where,

- I_{scn} : Nominal short-circuit current
- K_i : Current temperature coefficient
- G_n : Nominal solar irradiance, typically $1000 W/m^2$
- T_n : Nominal cell temperature, typically $25^{\circ}C$

The diode's current I_d and voltage V_d are represented as an exponential relationship and are represented in Eq. (2).

$$I_d(T, V_d) = I_s(T) \left[\exp\left(\frac{V_d}{aV_t(T)} - 1\right) \right] \quad (2)$$

where,

- I_s : Diode saturation current
- a : Diode ideality constant
- V_d : Diode voltage
- V_t : Thermal voltage of the semiconductor junction

The temperature-dependent diode saturation current is defined in Eq. (3).

$$I_s(T) = \frac{I_{scn} + K_i(T - T_n)}{\exp\left(\frac{V_{ocn} + K_v(T - T_n)}{aV_t(T)}\right) - 1} \quad (3)$$

where,

- K_v : Voltage temperature coefficient
- V_{ocn} : Nominal open-circuit voltage

For the ideal model, the diode voltage V_d is the same as the PV voltage V_{pv} . In addition, the thermal voltage V_t is defined by Eq. (4) and is dependent on the temperature T .

$$V_t(T) = \frac{kT}{q} N_s \quad (4)$$

where,

- k : Boltzmann's constant ($1.3807 \times 10^{-23} J.K^{-1}$)
- q : Electron charge ($1.60217662 \times 10^{-19} C$)
- N_s : Number of PV cells in series

The relationship between the PV current I_{pv} and PV voltage V_{pv} for the ideal PV model is calculated using Kirchhoff's circuit rules.

$$I_{pv} = I_{ph}(G, T) - I_d(T, V_{pv}) \quad (5)$$

where equation (1) defines the photocurrent I_{ph} and Eq. (2) defines the diode current I_d . The PV output current is clearly connected to the solar irradiance G and temperature T , as shown by the PV current I_{pv} in Eq. (5).

2.2. MPPT algorithm

The maximum power point tracking (MPPT) technique enables PV systems to maximize their energy production under varying sun irradiation and ambient temperature conditions. The overall efficiency of the PV energy producing system therefore rises. The power-voltage characteristic of the PV module has a derivative, which serves as the foundation for the perturbation and observation (P&O) MPPT technique. Throughout the P&O MPPT process, the output voltage and current of the PV module or array are frequently sampled at subsequent sampling stages in order to calculate the corresponding output power and the power derivative with voltage [6]. The MPPT technique was carried out by altering the power converter PWM controller's reference signal.

A control unit microcontroller or DSP device may be used to execute the P&O MPPT algorithm [7], [8], as shown in Fig. 4's flowchart, which is based on the procedure described in [9]. Until the gradient value reaches a specified threshold, which signifies that convergence close to the MPP with the required accuracy has been accomplished, this step is repeated.

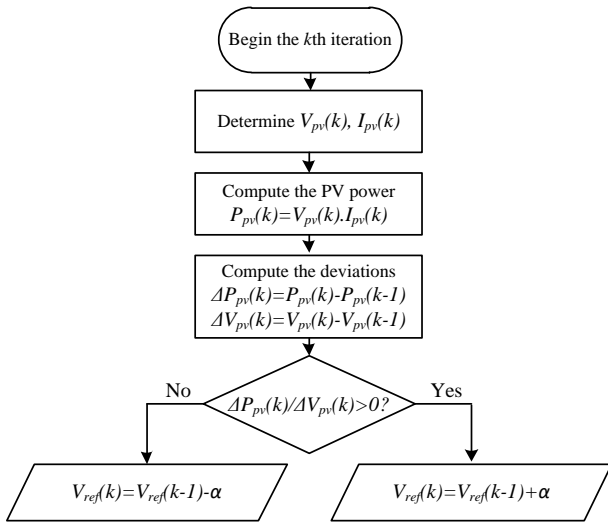


Figure 4. A flowchart of the algorithm implementing the P&O MPPT process

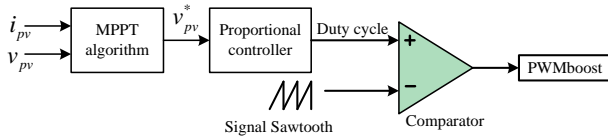


Figure 5. MPPT control structure for the boost converter

To simplify the MPPT control, a perturb and observe (P&O) approach has been used, as shown in Fig. 5. The P&O MPPT algorithm calculates the reference voltage for the PV panels (i.e., the voltage at the maximum power point), which is then regulated by a proportional controller or PI adaptive controller to prevent the overshoot [10], [11].

2.3. DC-DC Boost converter

In a double-stage PV system, the DC-DC converter is responsible for boosting the voltage of the PV module to a desired voltage level for the inverter stage. The DC-DC converter additionally plays the MPPT control of the PV panels, and thus, prolonged running hours can be carried out in a double-stage PV system. MATLAB-Simulink tools were used to create a boost converter. The converter is rated at 3kW and has the following specifications: These design parameters are specified in the m-file.

Boostparam.m:

```
fb=2e4;           % Switching frequency 20kHz
Vo=400;          % Average output voltage
Prated= 3e3;     % Output power 3kW
Vin =260;        % Input voltage
DeltaI=0.2;      % Ripple current of inductor
DeltaV=0.06;     % Ripple voltage of filter capacitor
Io=Prated/Vo;    % Output current
Lb= Vin*(Vo-Vin)/(fb*DeltaI*Vo) % Boost inductor
Cdc=Io*(Vo-Vin)/(fb*DeltaV*Vo) %DC-link capacitor
```

2.4. DC-AC Inverter

In the inverter stage, the single-phase inverter is used to convert the DC voltage of PV generator into the AC voltage for connection to the grid. The IGBT is used for switching devices because it can handle large power, which is suitable for PV systems.

2.5. LCL filter

In order to filter the harmonics produced by the inverter, an LCL filter is usually employed to connect an inverter to the utility grid. An L filter or LCL filter is typically placed between the inverter and the grid in order to minimize the switching frequency harmonics produced by grid-connected inverters. The LCL filter offers better dynamic characteristics and a higher capacity for attenuating high-order harmonics than the L filter. An LCL filter, however, might have stability problems due to the undesirable resonance that zero impedance causes at specific frequencies. The system may be shielded from this resonance using a number of dampening strategies. One approach is to connect a physical passive component, such as a resistor, in series with the filter capacitor [12]. The LCL filter design parameters are specified in the m-file.

LCLfilterparam.m:

```
Irated=20;           % Rated current
wg=314;             % Grid frequency
VgRMS=230           % Grid voltage
Vdc=400             % DC-link voltage
Prated=3e3          % Output power
Qre=0.025*Prated;   % Reactive power
Iripplemax=0.2*Irated; % maximum ripple current
finv=10e3;          % switching frequency
L=Vdc/(2*Iripplemax*finv) % Total inductance
Cf=Qre/(wg*(VgRMS^2)) % filter capacitor
```

3. Grid Connected Inverter Control

3.1. Control Structure

Two primary control goals exist for a single-phase grid-connected PV system: (1) PV-side control to maximize electricity from PV panels, and (2) grid-side control to satisfy power grid demands. In order to meet these requirements, a typical control structure for a grid-connected PV system consists of two cascading loops [13]. The outside power/voltage control loop establishes current references, while the inner control loop is in charge of modifying the current to maintain power quality and may also carry out other tasks [14].

Figure 6 shows the general control structure of a single-phase double-stage grid-connected PV system. The MPPT control is executed on the DC-DC converter, while the other functions are handled by the PV inverter control.

Figure 7 shows the inverter control diagram in the $\alpha\beta$ -reference frame.

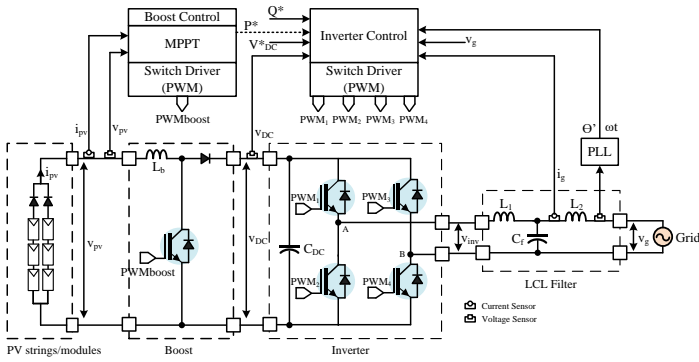


Figure 6. General control structure of a single-phase double-stage grid connected PV system

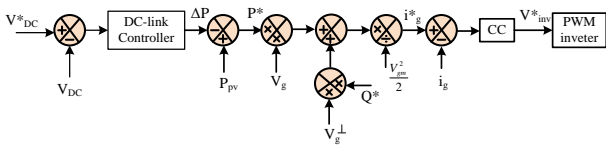


Figure 7. Inverter control diagram in the $\alpha\beta$ -reference frame

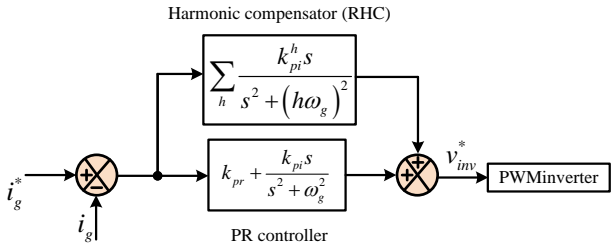


Figure 8. The current control with a harmonic compensator

The current control with a harmonic compensator for a double-stage single-phase PV System is shown in Fig. 8. The PR controller and harmonic compensator (RHC) are used to maintain a high-quality grid current.

3.2. Grid Synchronization

Grid synchronization is a crucial grid monitoring activity that considerably improves the dynamic performance and stability of the entire control system.

Figure 9 illustrates the PLL-based synchronization system's architecture. The PLL system consists of a phase detector (PD) for detecting phase differences, a PI-based loop filter (PI-LF) for smoothing the frequency output, and finally a voltage-controlled oscillator (VCO) [15].

Figure 10, the SOGI-PLL is used to produce the in-quadrature voltage system [16].

Figure 10, the SOGI-PLL is used to produce the in-quadrature voltage system [16].

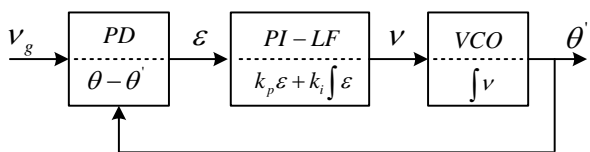


Figure 9. Structure of a PLL system

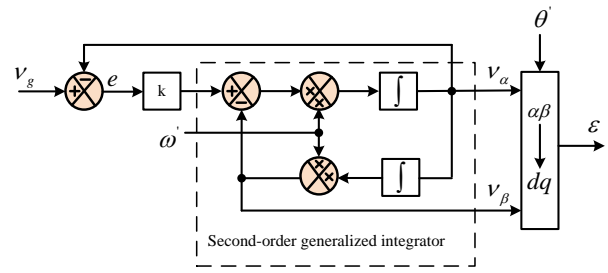


Figure 10. SOGI-PLL

Table 1. The 3-kW double-stage photovoltaic inverter system's parameters

Parameter	Value	Symbol
Boost inductor	2.2 mH	L_b
Boost Switching frequency	20 kHz	f_b
DC-link Capacitor	2200 μ F	C_{DC}
Grid voltage ((RMS))	230 V	V_g
Grid frequency	314 rad/s	ω_g
LCL filter	2.5 mH	L_1
	2.5 mH	L_2
	4.5 μ F	C_f

The system and control parameters are provided in Table 1. The parameters such as boost inductor, switching frequency of boost converter, dc-link capacitor, grid voltage, and frequency, and LCL filter are used in the simulation.

4. Simulation Result

The simulation results are displayed in Fig. 11, Fig. 12, and Fig. 13, where the solar irradiation changed in steps at a fixed ambient temperature of 25 °C, and the system was run at a unity power factor based on needs. Figure 11 shows the output power from PV arrays, which is from 0s to 0.1s irradiance 600 W/m², from 0.1s to 0.2s irradiance 1000 W/m², and 0.2s to 0.3s the irradiance 800 W/m². The step variations in solar irradiance really mirror PV intermittency, resulting in a continual input of fluctuating PV power.

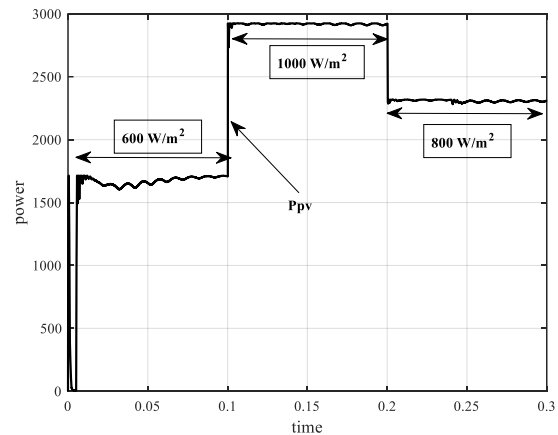


Figure 11. The output power PV

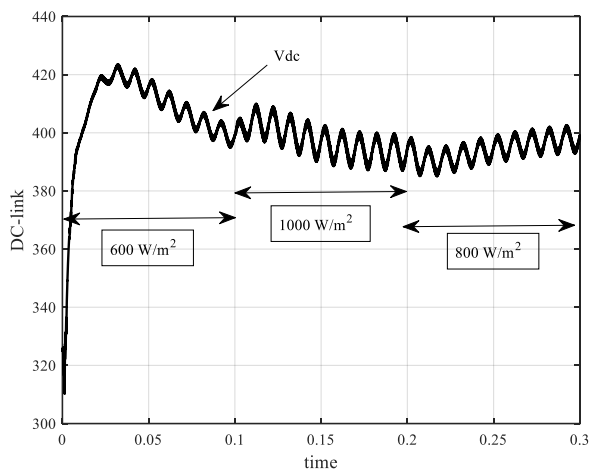


Figure 12. DC-link voltage

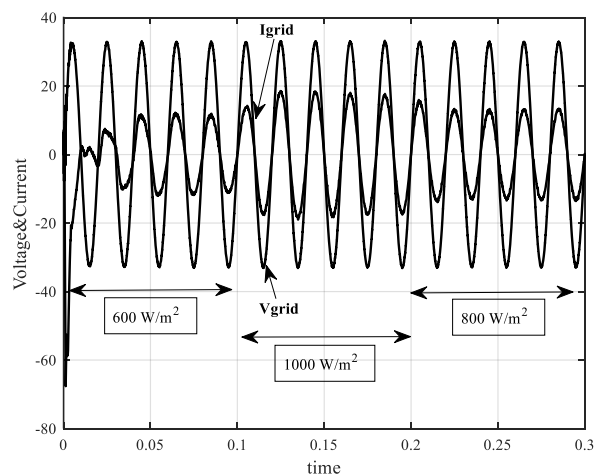


Figure 13. Grid current (20 A/div) and grid voltage (200V/div)

Figure 12 shows the voltage of the DC link, which is regulated by using a proportional controller. This voltage remains around 400 V DC, while the irradiance fluctuates between 600 W/m², 800 W/m², and 1000 W/m².

Figure 13 shows the grid current and voltage. The voltage is displayed on a scale of 200 V/div, while the current is displayed on a scale of 20 A/div. The value of the current depends on irradiance, which means that at high irradiance, the most current is transferred into the grid.

5. Conclusion

This paper presents the modeling and simulation of a grid-connected PV system with a P&O MPPT algorithm to inject the power extracted from the PV array. The current is controlled by a harmonic compensator. As in the simulation the current is provided by the results of the solar PV system and delivered to the utility grid. The grid voltage has a total harmonic distortion (THD) of 3.4% and the total harmonic distortion (THD) of the grid current is around 3.5% at the nominal operating condition. Future work will involve creating an ECU hardware module with a microcontroller or field programmable gate array (FPGA).

References

- [1] M. Morjaria, D. Anichkov, V. Chadliev, and S. Soni, "A Grid-Friendly Plant: The Role of Utility-Scale Photovoltaic Plants in Grid Stability and Reliability," *IEEE Power Energy Mag.*, vol. 12, no. 3, pp. 87–95, 2014, doi: 10.1109/MPE.2014.2302221.
- [2] Patrao, Iván, E. Figueres, F. González-Espín, and G. Garcera, "Transformerless topologies for grid-connected single-phase photovoltaic inverters," *Renew. Sustain. Energy Rev.*, vol. 15, no. 7, pp. 3423–3431, 2011.
- [3] Q. Li and P. Wolfs, "A Review of the Single-Phase Photovoltaic Module Integrated Converter Topologies with Three Different DC Link Configurations," *IEEE Trans. Power Electron.*, vol. 23, no. 3, pp. 1320–1333, 2008, doi: 10.1109/TPEL.2008.920883.
- [4] A. A. Nazari, P. Zacharias, F. M. Ibanez, and S. Somkun, "Design of Proportional-Resonant Controller with Zero Steady-State Error for a Single-Phase Grid-Connected Voltage Source Inverter with an LCL Output Filter," in *2019 IEEE Milan PowerTech*, 2019, pp. 1–6, doi: 10.1109/PTC.2019.8810554.
- [5] R. Teodorescu, F. Blaabjerg, M. Liserre, and P. C. Loh, "Proportional-resonant controllers and filters for grid-connected voltage-source converters," *IEE Proceedings-Electric Power Appl.*, vol. 153, no. 5, pp. 750–762, 2006.
- [6] N. Femia, G. Petrone, G. Spagnuolo, and M. Vitelli, "A Technique for Improving P&O MPPT Performances of Double-Stage Grid-Connected Photovoltaic Systems," *IEEE Trans. Ind. Electron.*, vol. 56, no. 11, pp. 4473–4482, 2009, doi: 10.1109/TIE.2009.2029589.
- [7] C. Srun, P. Chrin, S. Am, and B. Kim, "Design of MPPT Algorithms using Simulink Support Package for Arduino Hardware," *Int. J. Eng. Sci. Inf. Technol.*, vol. 2, no. 4, pp. 151–161, 2022.
- [8] M. Saran, S. Channareth, U. Sokoeun, S. Tara, N. Virbora, and S. Saravuth, "Optimization of an Integrated Hybrid Onboard Charger with High Efficiency of MPPT Solar Charger for Sustainable Energy of 3-Wheel Solar E-Rickshaw and Electric Vehicles," *Int. Res. J. Innov. Eng. Technol. - IRJIET*, vol. 6, no. 1, pp. 77–87, 2022.
- [9] D. C. Huynh, T. A. Nguyen, M. W. Dunnigan, and M. A. Mueller, "Maximum power point tracking of solar photovoltaic panels using advanced perturbation and observation algorithm," in *2013 IEEE 8th Conference on Industrial Electronics and Applications (ICIEA)*, 2013, pp. 864–869.
- [10] C. Srun, F. A. Samman, and R. S. Sadjad, "A high voltage gain DC-DC converter design based on charge pump circuit configuration with a voltage controller," in *2018 2nd International Conference on Applied Electromagnetic Technology (AEMT)*, 2018, pp. 79–84.
- [11] F. A. Samman, C. Srun, and R. S. O. Sadjad, "Adaptive look-up table and interpolated pi gain scheduling control for voltage regulator using DC-DC converter," *Int. J. Innov. Comput. Inf. Control*, vol. 15, no. 2, pp. 489–501, 2019.
- [12] C. Hanjoo and B. Chunggien, "Study and design of LCL filter for single-phase grid-connected PV inverter," in *Korean Electrical Society Conference Proceedings*, 2009, pp. 228–230.
- [13] Y. Yang, F. Blaabjerg, and H. Wang, "Low-Voltage Ride-Through of Single-Phase Transformerless Photovoltaic Inverters," *IEEE Trans. Ind. Appl.*, vol. 50, no. 3, pp. 1942–1952, 2014, doi: 10.1109/TIA.2013.2282966.
- [14] M. Ciobotaru, R. Teodorescu, and F. Blaabjerg, "Control of single-stage single-phase PV inverter," *Epe J.*, vol. 16, no. 3, pp. 20–26, 2006.
- [15] Y. Yang, L. Hadjidemetriou, F. Blaabjerg, and E. Kyriakides, "Benchmarking of phase locked loop-based synchronization techniques for grid-connected inverter systems," in *Proceedings of ICPE-IEEE ECCE Asia*, 2015, pp. 2167–2174.
- [16] M. Ciobotaru, R. Teodorescu, and F. Blaabjerg, "A new single-phase PLL structure based on second order generalized integrator," in *Proceedings of IEEE PESC*, 2006, pp. 1–6.

Clustering Mining Equipment Productivity Data using K-Means Algorithm

Muhammad Sandi Arista Ikhsan Yahmid^{a,*}, Tony Chen^b, Muhammad Emirat Millenium Try^c, Karno Nugroho Silangin^d, Nurul Alifia Putri^e, Aryanti Virtanti Anas^f

^aDepartment of Mining Engineering, Faculty of Engineering, Hasanuddin University, Indonesia. Email: sandiarista85@gmail.com

^bDepartment of Mining Engineering, Faculty of Engineering, Hasanuddin University, Indonesia. Email: tonychena33@gmail.com

^cDepartment of Informatics Engineering, Faculty of Engineering, Hasanuddin University, Indonesia. Email: emirat.millenium@yahoo.co.id

^dDepartment of Mining Engineering, Faculty of Engineering, Hasanuddin University, Indonesia. Email: kamonugroho.kn@gmail.com

^eDepartment of Mining Engineering, Faculty of Engineering, Hasanuddin University, Indonesia. Email: nurulalifia29@gmail.com

^fDepartment of Mining Engineering, Faculty of Engineering, Hasanuddin University, Indonesia. Email: virtanti@gmail.com

Abstract

Productivity and efficiency of mining equipment are among the most important factors contributing to unit mining cost. Therefore, knowing the condition of the machines on mining equipment is mandatory for mining supervisors. In analyzing the condition of mining equipment in large quantities requires a lot of energy and time. Based on these problems, a classification model is needed that can categorize mining equipment based on the performance and condition of the equipment. Clustering production data to determine the performance of mining equipment is important because it increases the productivity of production activities and reduces company losses. The purpose of this study is to obtain information on variables that affect the productivity of mining equipment and divide mining equipment categories based on production performance with data mining clustering techniques. The method in this study refers to the CRISP-DM with several adjustment using K-Means algorithm. The tools used are Jupyter Notebook with Python programming language. Variables used to cluster the mining equipment are Distance, Rites, and HaulDuration1 (working duration). There are 3 clusters formed based on the data used. Comparison of data on cluster with less production and less working duration can reach 58.50%. It shows that damaged equipment (less working duration) greatly affect the production of mining equipment as a whole.

Keywords: Data mining; mining equipment; machine learning; data clustering; K-Means algorithm

1. Introduction

There are many factors that affect productivity in mining production activities. A study of the digging and loading equipment can be carried out by monitoring the conditions in the field and the factors that affect the production capability of the mechanical equipment. The productivity of heavy equipment that is less than the target can be detrimental to the company [1], [2]. The productivity of the equipment can be seen from the ability of the equipment in its use. The factors that affect the productivity of equipment are the nature of the material, where the harder the type of material, the smaller the production of digging and loading equipment [3]. Productivity and efficiency of mining equipment are among the most important factors contributing to unit mining cost [4]. Therefore, knowing the condition of the machines on mining equipment is mandatory for mining supervisors.

However, one of the challenges of determining the performance of mining equipment requires consideration of quite a number of variables. In analyzing the condition of mining equipment in large quantities requires a lot of energy and time. Based on these problems, a classification model is needed that can categorize mining equipment based on the performance and condition of the equipment.

Clustering production data to determine the performance of mining equipment is important because it increases the productivity of production activities and reduces company losses. Related research, K-Means is a fairly simple clustering algorithm that partitions the dataset into several k clusters. The algorithm is quite easy to implement and run, relatively fast, easy to customize and widely used [5]. The main principle of this technique is to arrange k partitions/centroids/means from a set of data. The K-Means algorithm starts with the formation of a cluster partition at the beginning and then iteratively improves the cluster partition until there is no significant change in the cluster partition [6]. Data Mining (DM) is a series of processes to explore added value from a data set in the form of knowledge that has not been known

*Corresponding author.

Jalan Poros Malino km. 6, Bontomarannu
Gowa, Indonesia, 92171

manually. Several techniques that are often mentioned in the DM literature include clustering, classification, association rule mining, neural networks, and genetic algorithms [7].

Clustering is one of the sub categories of data mining and is a process where the same sample is divided into groups called clusters. Each cluster includes a sample where the members are similar to each other and different from the available samples from other groups [8]. Cluster analysis is a multivariate technique that has the main goal of grouping objects based on their characteristics. Cluster analysis classifies objects so that each object with the closest similarity to another object is in the same cluster [9]. The K-Means algorithm is one of the partitioning algorithms, because K-Means is based on determining the initial number of groups by defining the initial centroid value [10]. The K-means algorithm will group data items in a dataset into a cluster based on the closest distance to the randomly selected initial centroid value which is the starting center point, the distance with all data will be calculated using the Euclidean Distance formula [11].

The purpose of this study is to obtain information on variables that affect the productivity of mining equipment and divide mining equipment categories based on production performance with data mining clustering techniques. The model created is expected to help companies know the performance of equipment quickly based on the cluster group of the equipment at a time.

2. Theoretical Basis

Artificial intelligence (AI) is a method used to solve a problem by imitating the capabilities of living things into a computer program. One branch of AI technique is machine learning (ML) which tries to imitate how human processes or intelligent creatures learn and generalize. The hallmark of ML is the existence of a training process or training. Therefore, ML requires data to be learned which is called training data. There are at least two main functions in ML, namely prediction and classification. The prediction or regression function is used by the machine to estimate the output of an input data based on the data that has been studied in training. While classification is a method in ML used by machines to sort or classify objects based on certain characteristics [12].

Data mining is the process of extracting previously unknown information and patterns from large amounts of data. Data mining uses artificial intelligence, statistics, mathematics and machine learning in the process of extracting information for decision making [13]. K-Means is a machine learning algorithm that is often used in data mining. K-Means groups data into several clusters that have the maximum similarity between data in one cluster. Determination of the most optimal number of clusters can be done using the elbow method [14].

K-Means Clustering algorithm is one of the clustering methods by partitioning from set data into cluster K . It is a distance-based clustering algorithm that divides data into a number of clusters in numerical attributes [15].

1. Determine the number of clusters K and the number of maximum iterations.

2. Perform the initialization process K midpoint cluster, then the equation of centroid count feature [15]:

$$C_i = \frac{1}{M} \sum_{j=1}^M x_j \quad (1)$$

Equation 1 is done as much as p dimensions from $i = 1$ to $i = p$

3. Connect any observation data to the nearest cluster. Euclidean distance spacing measurements can be found using Eq. 2 [15].

$$d = \sqrt{(x_1 - x_2)^2 + (y_1 - y_2)^2} \quad (2)$$

4. Reallocation of data to each group based on comparison of distance between data with each group's centroid [15].

$$a_{ij} \begin{cases} 1 & d = \min\{D(x_i, c_j)\} \\ 0 & \text{otherwise} \end{cases} \quad (3)$$

5. Recalculate the cluster midpoint position.

a_{ij} is the value of the membership of point x_i to the center of the group c_i , d is the shortest distance from the data x_i to the group K after being compared, and c_i is the center of the group to 1. The objective function used by this method is based on the distance and the value of the data membership in the group. The objective function can be determined using Eq. 4 [15].

$$J = \sum_{i=1}^n \sum_{l=1}^k a_{il} D(x_i, c_l)^2 \quad (4)$$

n is the amount of data, k is the number of groups, a_{il} is the membership value of the data point x_i to the c_l group followed a has a value of 0 or 1. If the data is a member of a group, the value $a_{il} = 1$. If not, the value $a_{il} = 0$.

6. If there is a change in the cluster midpoint position or number of iterations < the maximum number of iterations, return to step 3. If not, then return the clustering result [15].

Determination of the optimal number of clusters can use the Elbow method. The Elbow method provides ideas by choosing the cluster value and then adding the cluster value to be used as a data model in determining the best cluster. This method will produce information in determining the best number of clusters by looking at the percentage of comparison results between the number of clusters that form an angle at a point [16].

Determination of the optimal number of clusters using the elbow method is done by looking at the SSE (Sum of Squared Error) value. SSE is shown as in Eq. 5 and Eq. 6 [17].

$$SSE = \sum_{i=1}^K \sum_{x_j \in C_i} |X_j - M_i|^2 \quad (5)$$

$$M_i = \frac{\sum_{j=1}^n X_j}{n} \quad (6)$$

where,

K = Number of clusters

$X = \{x_1, x_2, \dots, x_i, \dots, x_n\}$

$C = \{C_1, C_2, \dots, C_i, \dots, C_n\}$

M = Centroid of cluster (C_i)

Table1. Types and sources of research data

No.	Data Type	Time span	Amount of data
1	Mining equipment production data recorded every shift (Secondary)	2 months	15,427 rows and 62 columns data
2	Mining equipment incident status data (Secondary)	2 months	120,876 rows and 23 columns data

3. Method

The data used in the form of secondary data derived from the research of Mining Engineering students at Hasanuddin University in one of the coal mining companies. The data consists of 2 different files, namely production data and mining equipment incident status data. The time span of this data is two months with details which can be seen in Table 1.

There are many methods for analyzing data. One of the most popular is the Cross Industry Standard Process for Data Mining (CRISP-DM). The method in this study refers to the CRISP-DM with several adjustment. The tools used are Jupyter Notebook with Python programming language.

Data processing stages generally take up most of the time. Very large amounts of data can be analyzed further to get more information. Data Mining is a process that uses statistical, mathematical, artificial intelligence and machine learning techniques to extract information. After further data exploration, an anomaly was found in the data used, so that the anomaly data was cleaned. Then visualization of correlation data between several variables and the production of mining equipment is carried out. This visualization aims to better understand the relationship of variables that influence the production of mining equipment.

The last stage is done with one of the machine learning techniques, namely clustering with the K-Means algorithm. The K-Means algorithm will divide the data based on several influential variables given. Determination of the optimal number of clusters is done by the Elbow method. The Elbow method is done by looking at the point where the decrease in inertia (how far apart each sample is in a cluster) is no longer significant. This division of equipment categories will be useful as recommendations for equipment performance on a shift.

4. Research Discussion

The results of the first data mining process obtained ineffective data that actually did not need to be entered into the data recording. The data in question is data that has only one unique data and data that has the same information purpose as data in other columns. The data is discarded so that it can reduce data storage and data recording becomes faster.

During the visualization process, an anomaly was found in the data. It can be seen in Fig. 2, that many plots of data are gathered at long distances and the production is much higher than the other data. After being traced, it turns out that all of these data belong to the HBM999 type of equipment. It is assumed that this HBM999 represents

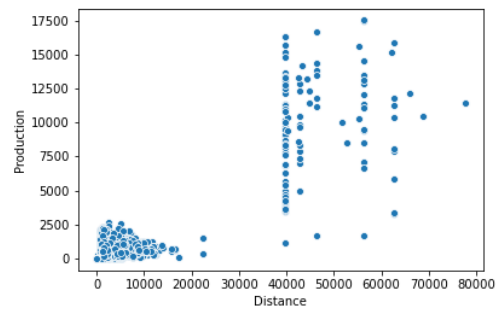


Figure 2. Anomalies in the distance and production variable data plots

many devices that do not yet have an ID so that they are combined into type HBM999. This data is then removed from the analysis and re-visualization is carried out.

The data visualization process is carried out for each type of variable that is considered to affect the production of equipment. The variables analyzed included Shift, Distance, Rites, Capacity, HaulDuration1 (duration of work), HaulDuration2 (duration of delay), HaulDuration3 (duration of standby) and HaulDuration4 (duration of maintenance). Visualization is made by scatter plot for each variable pair with production and heatmap to display correlation values. Figure 3 shows the difference in the average productivity of each equipment on the morning shift and night shift not much different. Even so, the average productivity on the morning shift is slightly higher than the night shift.

Figure 4 shows the pattern of equipment production with respect to distance, rotation and equipment capacity. The farther the distance of conveyance of the equipment, the production tends to be smaller. On the other hand, for large rites and capacities, the production tends to be greater.

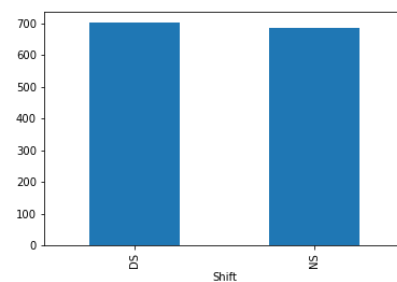


Figure 3. Production graph against shift time

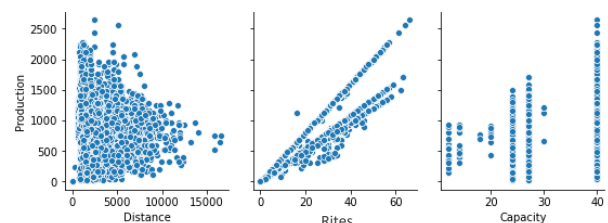


Figure 4. Plot production data against distance, rites and equipment capacity

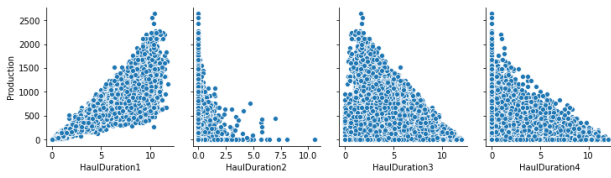


Figure 5. Plot production data against equipment activity duration

Figure 5 shows scatter plots of production data against equipment activity duration. *HaulDuration1* (working duration of equipment) tends to be directly proportional to its production. Meanwhile, *HaulDuration2* (snooze duration), *HaulDuration3* (standby duration) and *HaulDuration4* (maintenance duration) tend to be inversely proportional to their production. Figure 6 shows the correlation between variables. It can be seen that Rites and *HaulDuration1* have a high positive correlation to production, while *HaulDuration2*, *HaulDuration3* and *HaulDuration4* have a negative correlation with production.

Based on the relationship between variables and their relation to production, only a few variables are taken that are used in the clustering stage. the variables used are Distance, Rites and *HaulDuration1*. These three variables are used to see the production performance of mining equipment.

The last step is data clustering using the K-Means machine learning method. Determination of the optimal number of clusters is done by the Elbow method as shown in Fig. 7. It was found that the change in the inertia value was no longer significant at the point $k=3$. So it was determined to divide the data into 3 clusters.

The results of the K-Means clustering can be seen in Fig. 8. Clusters with label 0 (blue) indicate mining equipment with very low production even with the distance between the location where the material is taken to disposal is relatively close. Label 1 (orange) shows

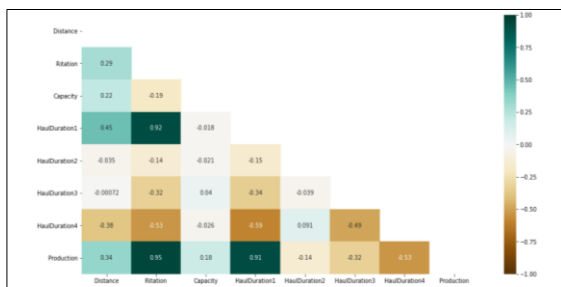


Figure 6. Heatmap of correlation between variables

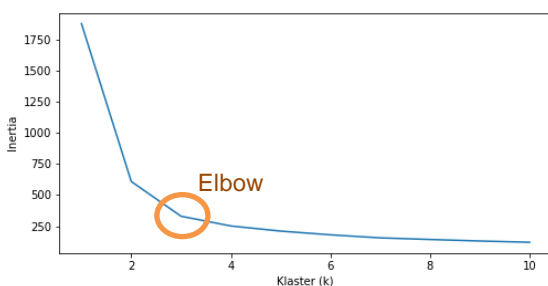


Figure 7. Clustering with elbow

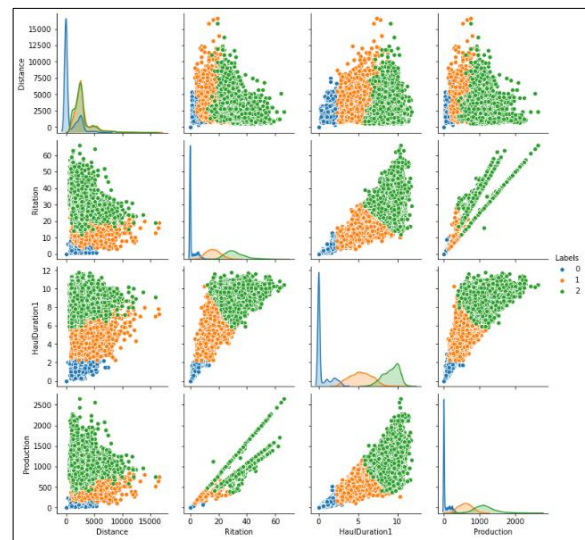


Figure 8. Mining equipment data plot along with its cluster

mining equipment with medium production. Most of the equipment that has long distances is also included in this cluster although its production is classified as less. Label 2 (green) indicates mining equipment with good to very high production performance. Comparison of data labelled 0 to the overall data reached 24.65%.

Based on Fig. 8, it can be seen that the duration of the equipment work greatly affects its production. *HaulDuration1* shows how long the equipment has been running while *HaulDuration4* shows how long the equipment has been down. The greater the time the equipment works, the production tends to be even greater. On the other hand, the greater the *HaulDuration4* time, the smaller the production will tend to be. Figure 8 shows the correlation value for *HaulDuration1* with production reaching 0.91 while the correlation value for *HaulDuration4* with production is -0.53.

Comparison of data in cluster 0 to the overall data reached 24.65%. In addition, data in cluster 1 shows equipment whose production is still not optimal with a percentage reaching 33.85% of the total data. This shows that damaged equipment with less duration of work greatly affects the production of mining equipment as a whole. Product productivity can be increased by anticipating potential breakdowns early with a predictive maintenance program. In addition, mining equipment management can be maximized because potential damage can be detected early.

5. Conclusions

Based on the results of the analysis of mining equipment productivity with data mining techniques is found that the working duration of the equipment greatly affects its production. Correlation value between equipment work duration and its production is 0.9, while the correlation value between maintenance duration and its production is -0.53. Comparison of data on cluster with

less production can reach 58.50% (total of clusters 0 and 1). It shows that damaged equipment (less working duration) greatly affect the production of mining equipment as a whole.

The K-Means model created in this study still cannot be said to be optimal for needs at the industrial level. This is because the data used is still raw and limited in terms of quantity and complexity. Further pre-processing and comparison with other models are required. However, this model can sufficiently demonstrate the production performance of mining equipment with the three most influential variables.

Acknowledgements

A big thank you for Ministry of Education and Culture Republic of Indonesia for providing a forum for Indonesian students to be creative and work through the Student Creativity Program (PKM), especially in PKM-RE activities, because of this program this research can be carried out.

References

- [1] D. Sujatmiko, "Analisis Produktivitas Alat Berat Studi Kasus Proyek Pembangunan PLTU Talaud 2 x 3 MW Sulawesi Utara," Universitas Gadjah Mada, 2013.
- [2] A. T. Tenriajeng, "Pemindahan Tanah Mekanis," Universitas Gunadarma, 2003.
- [3] W. Hartono, *Pemindahan Tanah Mekanik (Alat-alat Berat)*. Surakarta, Indonesia: Lembaga Pengembangan Interscience Publication, 2005.
- [4] J. Paraszczak, "Understanding and Assessment of Mining Equipment Effectiveness," *Trans. Inst. Min. Metall. Sect. A Min. Technol.*, vol. 114, no. 3, pp. 147–151, 2005.
- [5] X. Wu and V. Kumar, *The top ten algorithms in data mining*. London, United Kingdom: CRC Press, 2009.
- [6] I. H. Witten and E. Frank, *Data Mining: Practical Machine Learning and Tool*, 3rd Editio. Burlington, Vermont, USA: Morgan Kaufmann Publisher, 2011.
- [7] Lindawati, "Data mining dengan teknik clustering dalam pengklasifikasian data mahasiswa studi kasus prediksi lama studi mahasiswa Universitas Bina Nusantara," *Semin. Nas. Inform. 2008 (semnasIF 2008)*, vol. 1, no. 5, pp. 174–180, 2008.
- [8] Ediyanto, N. M. Mara, and N. Satyahadewi, "Pengklasifikasian karakteristik dengan metode K-Means Cluster Analysis," *Bul. Ilm. Mat. Stat. dan Ter.*, vol. 2, no. 2, pp. 133–136, 2013.
- [9] S. G. Farhac, R. Yasin, and R. K. Seyyed, "Combining Clustering Algorithms for Provide Marketing Policy in Electronic Stores," *Int. J. Program. Lang. Appl.*, vol. 4, no. 1, 2014.
- [10] T. S. Madhulatha, "An overview on clustering methods," *IOSR J. Eng.*, vol. 2, no. 4, pp. 719–725, 2012.
- [11] A. Agrawal and H. Gupta, "Global K-Means (gkm) clustering algorithm: A survey," *Int. J. Comput. Appl.*, vol. 79, no. 2, pp. 20–24, 2013.
- [12] A. Ahmad, "Mengenal Artificial Intelligence, Machine Learning, Neural Network, dan Deep Learning," *J. Teknol. Indones.*, 2017.
- [13] P. Bhatia, *Data Mining and Warehousing Principles and Practical Techniques*, Edisi ke-1. United Kingdom: Cambridge University Press, 2019.
- [14] A. Winarta and W. J. Kurniawan., "Optimasi Cluster K-Means Menggunakan Metode Elbow pada Data Pengguna Narkoba dengan Pemrograman Python," *J. Tek. Inform. Kaputama*, vol. 5, no. 1, pp. 113–119, 2021.
- [15] M. A. Syakur, B. K. Khotimah, E. M. S. Rochman, and B. D. Satoto, "Integration K-Means Clustering Method and Elbow Method For Identification of The Best Customer Profile Cluster," in *IOP Conf. Series: Materials Science and Engineering* 336, p. 2018.
- [16] P. Bholowalia and A. Kumar, "EBK-Means: A Clustering Technique based on Elbow Method and K-Means in WSN," *Int. J. Comput. Appl.*, vol. 105, no. 9, pp. 975–8887, 2014.
- [17] T. Thinsungnoen, N. Kaoungku, P. Durongdumronchai, K. Kerdprasop, and N. Kerdprasop., "The Clustering Validity with Silhouette and Sum of Squared Errors," in *Proceedings of the 3rd International Conference on Industrial Application Engineering* 2015, 2015, pp. 44–51.

Natural Frequencies of Isotropic Rectangular Plates in Improved Accuracy

Yoshihiro Narita^{a,*}

^aHokkaido University (Professor Emeritus), Sapporo, Japan. Email: ynarita@eng.hokudai.ac.jp

Abstract

The objectives of this paper are to re-visit one of the most important vibration problems and to present comprehensive lists of accurate natural frequencies for isotropic thin rectangular plates. For this purpose, a simple yet very accurate analytical approach is described to study the free vibration of the plates. In numerical computations, convergence and comparison studies are conducted to collaborate accuracy of the present solution and to demonstrate the improvement of numerical solutions in percentage from previous standard results. Twenty-one tables are then provided to list the lowest six frequency parameters for all possible combinations of three typical edge conditions (clamped, simply supported and free edges). Each table is given in five significant figures for non-Levy type problem and in six significant figures for Levy type problem (i.e., plate with two opposite edges simply supported). These results are presented for five different aspect ratios to follow the same format of the previous standard reference.

Keywords: Free vibration, rectangular plate, natural frequency, accuracy, boundary condition

1. Introduction

The free vibration of isotropic thin rectangular plates has been one of the most important problems for a long period of time in mechanical vibration. References up to 1970 on vibrations of general plate shapes are summarized in the famous monograph [1], and the wide coverage for natural frequencies of isotropic rectangular plates was made in 1973 for all possible twenty-one combinations of boundary conditions and five aspect ratios [2]. The numerical results in this reference have been widely accepted as accurate and comprehensive data, where Ritz method with beam functions is used for sixteen combinations not having opposite edges simply supported and the exact solution is employed for five remaining combinations having two opposite edges simply supported. Because of reasonable accuracy, the results are cited as the standard and reliable data in the vibration design book [3].

Besides these classical references, this topic has a long history to date back to an early work by Young in 1950 [4], and since then many papers have appeared including a series of Gorman's work [5-7] by using a method of superposition. Those related studies up to the year of 1980 are listed in the author's work [8]. The development in the 1980's is summarized also in review papers [9,10]. More recently, two papers [11,12] presented their approaches to solve this problem.

When one extends the problem to broader sets of the boundary conditions, namely clamped, simply supported and free edges (denoted by capital letters, C, S and F, respectively), there are $3^4=81$ combinations for a

rectangular plate fixed in the space. Physically, however, some plates have the identical natural frequencies, for example, in C-S-F-F and C-F-F-S square plates (note that the first letter indicates Edge(1) and the rest in counter-clock wise direction). Polya counting theory is applied to solve for the exact number of combinations in Ref.[13], and recently this approach is extended to calculate the number of physically meaningful combinations for generally shaped plates [14].

In this paper, natural frequencies of isotropic rectangular plates are listed in comprehensive way to serve as a new standard data in mechanical design, although the frequencies of the plates with typical edges, such as totally clamped or cantilevered plates, were already solved. For this purpose, Ritz method is employed by using polynomial functions with boundary index, not by the beam functions [2]. With this, better accuracy is realized as resulting in lower values in the upper-bound solutions.

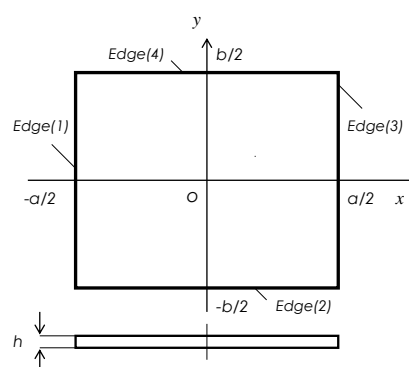


Figure 1. Rectangular plate in the coordinate system

*Corresponding author.

Yamato University, Katayama
Suita, Osaka, Japan

2. Outline of Analytical Method

A previous solution is used here as in [13] based on the method of Ritz within the classical thin plate theory. This analysis-based solution has a low computational cost and easiness in varying combination in boundary conditions, in contrast to numerical methods such as the finite element method. Figure 1 shows a geometry of rectangular plate and the coordinate system, and the dimension of the plate is given by $a \times b \times h$ (thickness).

The relation between stress and strain is written in

$$\begin{Bmatrix} \sigma_x \\ \sigma_y \\ \tau_{xy} \end{Bmatrix} = \begin{bmatrix} Q_{11} & Q_{12} & 0 \\ Q_{12} & Q_{22} & 0 \\ 0 & 0 & Q_{66} \end{bmatrix} \begin{Bmatrix} \epsilon_x \\ \epsilon_y \\ \gamma_{xy} \end{Bmatrix} \quad (1)$$

where the elements are given for isotropic material by

$$Q_{11} = Q_{22} = \frac{E}{1-\nu^2}, Q_{12} = \nu Q_{11}, Q_{66} = G = \frac{E}{2(1+\nu)} \quad (2)$$

with E is Young's modulus, G is a shear modulus and ν is a Poisson's ratio. When Eq. (1) is integrated through the thickness after multiplying by a thickness coordinate z , one gets moment resultant

$$\begin{Bmatrix} M_x \\ M_y \\ M_{xy} \end{Bmatrix} = \begin{bmatrix} D_{11} & D_{12} & 0 \\ D_{12} & D_{22} & 0 \\ 0 & 0 & D_{66} \end{bmatrix} \begin{Bmatrix} \epsilon_x \\ \epsilon_y \\ \gamma_{xy} \end{Bmatrix} \quad (3)$$

If one considers the small amplitude (linear) free vibration of a thin plate, the deflection w may be written by

$$w(x, y, t) = W(x, y) \sin \omega t \quad (4)$$

where W is the amplitude and ω is a radian frequency of the plate. Then, the maximum strain energy due to the bending is expressed by

$$U_{\max} = \frac{1}{2} \iint_A \{\kappa\}^T \begin{bmatrix} D_{11} & D_{12} & 0 \\ D_{12} & D_{22} & 0 \\ 0 & 0 & D_{66} \end{bmatrix} \{\kappa\} dA \quad (5)$$

where the D_{ij} are the bending stiffnesses and $\{\kappa\}$ is a curvature vector

$$\{\kappa\} = \left\{ -\frac{\partial^2 W}{\partial x^2} \quad -\frac{\partial^2 W}{\partial y^2} \quad -2\frac{\partial^2 W}{\partial x \partial y} \right\}^T \quad (6)$$

The maximum kinetic energy is given by

$$T_{\max} = \frac{1}{2} \rho h \omega^2 \iint_A W^2 dA \quad (7)$$

where ρ [kg/m³] is the mass per unit volume.

For the sake of simplicity, non-dimensional quantities are introduced as

$$\xi = \frac{2x}{a}, \eta = \frac{2y}{b} \quad (\text{non-dimensional coordinates}),$$

$$\alpha = \frac{a}{b} \quad (\text{aspect ratio}),$$

$$D = \frac{Eh^3}{12(1-\nu^2)} \quad (\text{reference stiffness}) \quad (8)$$

$$\Omega = \omega a^2 \sqrt{\frac{\rho h}{D}} \quad (\text{frequency parameter})$$

The next step in the Ritz method is to assume that the amplitude as

$$W(\xi, \eta) = \sum_{m=0}^{M-1} \sum_{n=0}^{N-1} A_{mn} X_m(\xi) Y_n(\eta) \quad (9)$$

where A_{mn} are unknown coefficients, and $X_m(\xi)$, $Y_n(\eta)$ are the functions modified later so that any kinematical boundary conditions are satisfied at the edges.

After substituting Eq.(9) into the energies (5) and (7), the stationary value is obtained by

$$\frac{\partial}{\partial A_{\bar{m}\bar{n}}} (T_{\max} - U_{\max}) = 0 \quad (\bar{m} = 0, 1, 2, \dots; \bar{n} = 0, 1, 2, \dots) \quad (10)$$

Then the eigenvalue equation that contains the frequency parameter Ω is derived as

$$\sum_{m=0}^{M-1} \sum_{n=0}^{N-1} \left[d_{11} I^{(2200)} + \alpha^2 d_{12} (I^{(2002)} + I^{(0220)}) + \alpha^4 I^{(0022)} + 4\alpha^2 d_{66} I^{(1111)} - \Omega^2 I^{(0000)} \right]_{\bar{m}\bar{n}\bar{m}\bar{n}} \cdot A_{\bar{m}\bar{n}} = 0 \quad (\bar{m} = 0, 1, 2, \dots; \bar{n} = 0, 1, 2, \dots) \quad (11)$$

where an integral I is the products

$$I_{\bar{m}\bar{n}\bar{m}\bar{n}}^{(pqrs)} = \phi_{\bar{m}\bar{m}}^{(pq)} \cdot \phi_{\bar{n}\bar{n}}^{(rs)} \quad (12)$$

of the two integrals defined by

$$\phi_{\bar{m}\bar{m}}^{(pq)} = \int_{-1}^1 \frac{\partial^{(p)} X_{\bar{m}}}{\partial \xi^{\mathcal{E}^{(p)}}} \frac{\partial^{(q)} X_{\bar{m}}}{\partial \xi^{\mathcal{E}^{(q)}}} d\xi \quad (13)$$

Equation (11) is a set of linear simultaneous equations in terms of the coefficients A_{mn} , and the eigenvalues Ω may be extracted by using existing computer subroutines.

The analytical procedure developed thus far is a standard routine of the Ritz method, and the modification is explained next so as to incorporate arbitrary edge conditions into the amplitude $W(\xi, \eta)$. In the traditional approach, for example, using the beam functions for $X_m(\xi)$ and $Y_n(\eta)$, many different products of regular and hyper trigonometric functions exist for arbitrary conditions and it is difficult to make a unified subroutine to calculate all of the various kinds of integrals.

The present approach introduces a kind of polynomial

$$\begin{aligned} X_m(\xi) &= \xi^m (\xi + 1)^{B_1} (\xi - 1)^{B_3} \\ Y_n(\eta) &= \eta^n (\eta + 1)^{B_2} (\eta - 1)^{B_4} \end{aligned} \quad (14)$$

where B_1, B_2, B_3 and B_4 are "boundary indices" [13,15,16] which are added to satisfy the kinematical boundary conditions and are used in such a way as $B_i=0$ for F (free edge), 1 for S (simply supported edge) and 2 for C (clamped edge). To the C-S-F-F plate, for instance, $B_1=2, B_2=1$ and $B_3=B_4=0$ are applied. With the boundary indices B_i 's and Eqs.(14), the method of Ritz can accommodate arbitrary sets of the edge conditions, and the integrals (12) can be exactly evaluated.

3. Numerical Examples and Accuracy of Solution

3.1. Convergence and Comparison of the Solution

In numerical studies, the material constants are assumed for isotropic materials, and Young's modulus E and Poisson's ratio ν are included in the frequency parameters Ω in Eqs.(8). Poisson's ratio still affects values of the frequency parameters, and a constant of $\nu=0.3$ is used throughout in the paper, except for the comparison in Table 2 with results obtained by another author who used $\nu=0.333$ [5][7]. For thin plates, a value of plate thickness does not affect the frequency parameters, unlike in the analysis of shallow shells (panels) [15,16].

Table 1 presents convergence study of frequency parameters with increase of series terms in Eq.(9). Since the amplitude function satisfies kinematical conditions exactly, this Ritz method yields upper-bound solutions,

Table 1. Convergence characteristics of frequency parameters $\Omega=\omega a(\rho h/D)^{1/2}$ for square plates

Boundary Condition	mode					
	$M \times N$	1	2	3	4	5
C-C-C-C						
	6 × 6	35.986	73.395	73.395	108.22	131.78
	8 × 8	35.985	73.394	73.394	108.22	131.58
	10 × 10	35.985	73.394	73.394	108.22	131.58
	12 × 12	35.985	73.394	73.394	108.22	131.58
	14 × 14	35.985	73.394	73.394	108.22	131.58
S-S-S-S						
	6 × 6	19.739	49.349	49.349	78.958	100.12
	8 × 8	19.739	49.348	49.348	78.957	98.716
	10 × 10	19.739	49.348	49.348	78.957	98.696
	12 × 12	19.739	49.348	49.348	78.957	98.696
	14 × 14	19.739	49.348	49.348	78.957	98.696
C-F-F-F						
	6 × 6	3.4739	8.5128	21.313	27.461	30.980
	8 × 8	3.4718	8.5091	21.292	27.200	30.965
	10 × 10	3.4713	8.5077	21.288	27.199	30.960
	12 × 12	3.4711	8.5071	21.286	27.199	30.958
	14 × 14	3.4711	8.5029	21.285	27.198	30.945
C-C-F-F						
	6 × 6	6.9247	23.924	26.592	47.671	62.746
	8 × 8	6.9218	23.913	26.587	47.661	62.715
	10 × 10	6.9201	23.908	26.586	47.657	62.710
	12 × 12	6.9199	23.906	26.585	47.654	62.708
	14 × 14	*	*	*	*	*
F-F-F-F						
	6 × 6	13.469	19.726	24.541	35.288	35.288
	8 × 8	13.468	19.596	24.271	34.801	34.801
	10 × 10	13.468	19.596	24.270	34.801	34.801
	12 × 12	13.468	19.596	24.270	34.801	34.801
	14 × 14	13.467	19.596	24.271	34.801	34.801

*numerical instability occurs.

and therefore all the frequency parameters converge from above. For uniform edge conditions, such as C-C-C-C, S-S-S-S and F-F-F-F plates, the frequency parameters converge within five significant figures even for small number of terms as in 8×8 terms. When boundary conditions are mixed in one plate, however, the converge speed deteriorates as seen C-F-F-F plate. The worst result with respect to the convergence is given for C-C-F-F plate, where numerical instability occurs for the 14×14 solution, but these are still exceptions among twenty-one sets of edge conditions. For these two cases, the results in the following tables are obtained by using 12×12 solutions.

Table 2 is a comparison study with values of Gorman for C-C-C-C [6], C-F-F-F ($\nu=0.333$) [5] and F-F-F-F plates ($\nu=0.333$) [7]. The exact values can be obtained for S-S-S-S plate. In the all results presented in the table, good agreement is obtained with the present results. A method of Gorman, known as superposition method, is well known to yield accurate numerical results, although the formulation is a little cumbersome. Based on the convergence and comparison studies in these two tables, the accuracy of the present solutions is well established.

3.2. Comprehensive Results for Non-Levy Type Problem

Tables 3 presents lists of frequency parameters in five significant figures of totally clamped rectangular plates (C-C-C-C plate) for the lowest six modes. Aspect ratio is varied from $a/b=0.4, 2/3, 1$ (square), 1.5 and 2.5. This table uses the same format as in Ref.[2] and these results are presented by using the 12×12 solutions, together with the frequency parameters obtained by Leissa [2]. The difference is also calculated for each pair by using

$$\text{dif.}(\%) = \frac{\Omega_{\text{present}} - \Omega_{\text{Ref}[2]}}{\Omega_{\text{present}}} \times 100 \quad (\%) \quad (15)$$

Table 2. Comparison study of frequency parameters $\Omega= \omega a(\rho h/D)^{1/2}$ for square plates

Boundary Condition	mode					
	$M \times N$	1	2	3	4	5
C-C-C-C						
Present		35.985	73.394	73.394	108.22	131.58
Ref.[6]		35.98	73.40	73.40	108.2	131.6
S-S-S-S						
Present		19.7392	49.3480	49.3480	78.9568	98.6960
exact [2]		19.7392	49.3480	49.3480	78.9568	98.6960
C-F-F-F ($\nu=0.333$)						
Present		3.4598	8.3578	21.093	27.065	30.559
Ref.[5]		3.459	8.356	21.09	27.06	30.55
F-F-F-F ($\nu=0.333$)						
Present		13.169	19.224	24.423	34.233	34.233
Ref.[7]		13.17	19.22	24.42	34.23	34.23

Table 3 Frequency parameters $\Omega = \omega a (\rho h/D)^{1/2}$ for C-C-C-C plates.

mode	<i>a/b</i>	0.4	2/3	1	1.5	2.5
1	Present	23.644	27.005	35.985	60.761	147.77
	Ref.[2]	23.648	27.010	35.992	60.772	147.80
	dif.(%)	-0.02	-0.02	-0.02	-0.02	-0.02
2	Present	27.807	41.704	73.394	93.833	173.79
	Ref.[2]	27.817	41.716	73.413	93.860	173.85
	dif.(%)	-0.04	-0.03	-0.03	-0.03	-0.03
3	Present	35.417	66.124	73.394	148.78	221.36
	Ref.[2]	35.446	66.143	73.413	148.82	221.54
	dif.(%)	-0.08	-0.03	-0.03	-0.03	-0.08
4	Present	46.671	66.522	108.22	149.67	291.70
	Ref.[2]	46.702	66.552	108.27	149.74	291.89
	dif.(%)	-0.07	-0.05	-0.05	-0.04	-0.07
5	Present	61.495	79.805	131.58	179.56	384.35
	Ref.[2]	61.554	79.850	131.64	179.66	384.71
	dif.(%)	-0.10	-0.06	-0.05	-0.06	-0.09
6	Present	63.083	100.81	132.20	226.82	394.27
	Ref.[2]	63.100	100.85	132.24	226.92	394.37
	dif.(%)	-0.03	-0.04	-0.03	-0.04	-0.03

Table 5 Frequency parameters $\Omega = \omega a (\rho h/D)^{1/2}$ for C-C-C-F plates.

mode	<i>a/b</i>	0.4	2/3	1	1.5	2.5
1	Present	22.512	22.930	23.921	26.628	37.565
	Ref.[2]	22.577	23.015	24.020	26.731	37.656
	dif.(%)	-0.29	-0.37	-0.41	-0.39	-0.24
2	Present	24.582	29.384	39.998	65.864	76.098
	Ref.[2]	24.623	29.427	40.039	65.916	76.407
	dif.(%)	-0.17	-0.15	-0.10	-0.08	-0.41
3	Present	29.211	44.327	63.221	65.917	134.51
	Ref.[2]	29.244	44.363	63.493	66.219	135.15
	dif.(%)	-0.11	-0.08	-0.43	-0.46	-0.48
4	Present	36.985	62.186	76.710	106.66	152.35
	Ref.[2]	37.059	62.417	76.761	106.80	152.47
	dif.(%)	-0.20	-0.37	-0.07	-0.14	-0.08
5	Present	48.204	68.814	80.572	124.82	192.75
	Ref.[2]	48.283	68.887	80.713	125.40	193.01
	dif.(%)	-0.16	-0.11	-0.18	-0.46	-0.14
6	Present	61.744	69.555	116.66	152.38	212.69
	Ref.[2]	61.922	69.696	116.80	152.48	213.74
	dif.(%)	-0.29	-0.20	-0.12	-0.07	-0.49

Table 4 Frequency parameters $\Omega = \omega a (\rho h/D)^{1/2}$ for C-C-C-S plates.

mode	<i>a/b</i>	0.4	2/3	1	1.5	2.5
1	Present	23.439	25.859	31.826	48.159	107.04
	Ref.[2]	23.440	25.861	31.829	48.167	107.07
	dif.(%)	0.00	-0.01	-0.01	-0.02	-0.02
2	Present	27.016	38.094	63.331	85.492	139.61
	Ref.[2]	27.022	38.102	63.347	85.507	139.66
	dif.(%)	-0.02	-0.02	-0.03	-0.02	-0.04
3	Present	33.785	60.304	71.076	123.95	194.26
	Ref.[2]	33.799	60.325	71.084	123.99	194.41
	dif.(%)	-0.04	-0.03	-0.01	-0.03	-0.08
4	Present	44.109	65.509	100.79	143.95	270.34
	Ref.[2]	44.131	65.516	100.83	143.99	270.48
	dif.(%)	-0.05	-0.01	-0.04	-0.03	-0.05
5	Present	58.001	77.533	116.36	158.27	322.45
	Ref.[2]	58.034	77.563	116.40	158.36	322.55
	dif.(%)	-0.06	-0.04	-0.04	-0.06	-0.03
6	Present	62.964	92.116	130.35	214.52	353.16
	Ref.[2]	62.971	92.154	130.37	214.78	353.43
	dif.(%)	-0.01	-0.04	-0.01	-0.12	-0.08

Table 6 Frequency parameters $\Omega = \omega a (\rho h/D)^{1/2}$ for C-C-S-S plates.

mode	<i>a/b</i>	0.4	2/3	1	1.5	2.5
1	Present	16.848	19.951	27.054	44.890	105.30
	Ref.[2]	16.849	19.952	27.056	44.893	105.31
	dif.(%)	-0.01	0.00	-0.01	-0.01	-0.01
2	Present	21.357	34.020	60.538	76.545	133.48
	Ref.[2]	21.363	34.024	60.544	76.554	133.52
	dif.(%)	-0.03	-0.01	-0.01	-0.01	-0.03
3	Present	29.226	54.364	60.786	122.32	182.66
	Ref.[2]	29.236	54.370	60.791	122.33	182.73
	dif.(%)	-0.04	-0.01	-0.01	-0.01	-0.04
4	Present	40.493	57.508	92.836	129.39	253.08
	Ref.[2]	40.509	57.517	92.865	129.41	253.18
	dif.(%)	-0.04	-0.02	-0.03	-0.01	-0.04
5	Present	51.450	67.790	114.56	152.53	321.57
	Ref.[2]	51.457	67.815	114.57	152.58	321.60
	dif.(%)	-0.01	-0.04	-0.01	-0.03	-0.01
6	Present	55.096	90.051	114.70	202.61	344.35
	Ref.[2]	55.117	90.069	114.72	202.66	344.48
	dif.(%)	-0.04	-0.02	-0.01	-0.02	-0.04

Table 7 Frequency parameters $\Omega = \omega a (\rho h/D)^{1/2}$ for C-C-S-F plates.

mode	<i>a/b</i>	0.4	2/3	1	1.5	2.5
1	Present	15.633	16.213	17.537	20.964	33.529
	Ref.[2]	15.696	16.287	17.615	21.035	33.578
	dif.(%)	-0.40	-0.46	-0.44	-0.34	-0.15
2	Present	18.338	24.172	36.023	54.916	66.363
	Ref.[2]	18.373	24.201	36.046	55.184	66.612
	dif.(%)	-0.19	-0.12	-0.06	-0.49	-0.38
3	Present	23.961	40.680	51.812	63.154	119.32
	Ref.[2]	23.987	40.701	52.065	63.178	119.90
	dif.(%)	-0.11	-0.05	-0.49	-0.04	-0.48
4	Present	32.744	50.600	71.077	98.897	150.78
	Ref.[2]	32.810	50.822	71.194	99.007	150.83
	dif.(%)	-0.20	-0.44	-0.17	-0.11	-0.03
5	Present	44.799	58.945	74.326	108.671	187.44
	Ref.[2]	44.862	59.071	74.349	109.22	187.61
	dif.(%)	-0.14	-0.21	-0.03	-0.51	-0.09
6	Present	50.073	66.213	105.79	150.86	192.23
	Ref.[2]	50.251	66.262	106.28	150.90	193.23
	dif.(%)	-0.35	-0.07	-0.47	-0.03	-0.52

Table 9 Frequency parameters $\Omega = \omega a (\rho h/D)^{1/2}$ for C-S-C-F plates.

mode	<i>a/b</i>	0.4	2/3	1	1.5	2.5
1	Present	22.483	22.778	23.371	24.678	28.466
	Ref.[2]	22.544	22.855	23.460	24.775	28.564
	dif.(%)	-0.27	-0.34	-0.38	-0.39	-0.34
2	Present	24.261	27.930	35.571	53.682	70.270
	Ref.[2]	24.296	27.971	35.612	53.731	70.561
	dif.(%)	-0.15	-0.15	-0.11	-0.09	-0.41
3	Present	28.314	40.651	62.875	64.682	113.89
	Ref.[2]	28.341	40.683	63.126	64.959	114.00
	dif.(%)	-0.10	-0.08	-0.40	-0.43	-0.09
4	Present	35.301	62.093	66.762	97.121	130.26
	Ref.[2]	35.345	62.310	66.808	97.257	130.84
	dif.(%)	-0.12	-0.35	-0.07	-0.14	-0.45
5	Present	45.634	62.642	77.374	123.95	159.30
	Ref.[2]	45.710	62.695	77.502	124.48	159.54
	dif.(%)	-0.17	-0.08	-0.16	-0.43	-0.15
6	Present	59.455	68.562	108.87	127.83	209.34
	Ref.[2]	59.562	68.683	108.99	127.92	210.32
	dif.(%)	-0.18	-0.18	-0.11	-0.07	-0.47

Table 8 Frequency parameters $\Omega = \omega a (\rho h/D)^{1/2}$ for C-C-F-F plates. (10x10 solution)

mode	<i>a/b</i>	0.4	2/3	1	1.5	2.5
1	Present	3.9731	4.9688	6.9201	11.180	24.832
	Ref.[2]	3.9857	4.9848	6.9421	11.216	24.911
	dif.(%)	-0.32	-0.32	-0.32	-0.32	-0.32
2	Present	7.1312	13.237	23.908	29.783	44.571
	Ref.[2]	7.1551	13.289	24.034	29.901	44.719
	dif.(%)	-0.33	-0.39	-0.53	-0.40	-0.33
3	Present	13.042	23.278	26.586	52.376	81.510
	Ref.[2]	13.101	23.384	26.681	52.615	81.879
	dif.(%)	-0.45	-0.45	-0.36	-0.46	-0.45
4	Present	21.733	30.118	47.657	67.766	135.83
	Ref.[2]	21.844	30.262	47.785	68.090	136.52
	dif.(%)	-0.51	-0.48	-0.27	-0.48	-0.51
5	Present	22.798	34.139	62.710	76.812	142.49
	Ref.[2]	22.896	34.240	63.039	77.041	143.10
	dif.(%)	-0.43	-0.30	-0.52	-0.30	-0.43
6	Present	26.404	52.245	65.539	117.55	165.03
	Ref.[2]	26.501	52.398	65.833	117.90	165.63
	dif.(%)	-0.37	-0.29	-0.45	-0.30	-0.37

Table 10 Frequency parameters $\Omega = \omega a (\rho h/D)^{1/2}$ for C-S-S-F plates.

mode	<i>a/b</i>	0.4	2/3	1	1.5	2.5
1	Present	15.591	15.999	16.792	18.469	23.004
	Ref.[2]	15.649	16.067	16.865	18.540	23.067
	dif.(%)	-0.37	-0.42	-0.43	-0.39	-0.27
2	Present	17.915	22.421	31.114	50.419	59.725
	Ref.[2]	17.946	22.449	31.138	50.442	59.969
	dif.(%)	-0.17	-0.13	-0.08	-0.05	-0.41
3	Present	22.880	36.683	51.397	53.467	111.90
	Ref.[2]	22.902	36.703	51.631	53.715	111.95
	dif.(%)	-0.09	-0.05	-0.46	-0.46	-0.04
4	Present	30.855	50.486	64.021	88.699	114.57
	Ref.[2]	30.892	50.696	64.043	88.802	115.11
	dif.(%)	-0.12	-0.42	-0.03	-0.12	-0.47
5	Present	42.045	57.798	67.540	107.67	153.08
	Ref.[2]	42.108	57.908	67.646	108.19	153.24
	dif.(%)	-0.15	-0.19	-0.16	-0.48	-0.10
6	Present	50.053	59.808	101.12	126.06	188.57
	Ref.[2]	50.222	59.840	101.21	126.09	189.49
	dif.(%)	-0.34	-0.05	-0.09	-0.03	-0.49

Table 11 Frequency parameters $\Omega = \omega a (\rho h/D)^{1/2}$ for CSFF plates. (10x10 solution)

mode	<i>a/b</i>	0.4	2/3	1	1.5	2.5
1	Present	3.8437	4.4125	5.3512	6.9187	10.087
	Ref.[2]	3.8542	4.4247	5.3639	6.9309	10.100
	dif.(%)	-0.27	-0.28	-0.24	-0.18	-0.12
2	Present	6.4020	10.871	19.076	27.182	35.048
	Ref.[2]	6.4198	10.912	19.171	27.289	35.157
	dif.(%)	-0.28	-0.37	-0.50	-0.39	-0.31
3	Present	11.523	22.853	24.672	38.386	74.664
	Ref.[2]	11.576	22.958	24.768	38.586	74.990
	dif.(%)	-0.46	-0.46	-0.39	-0.52	-0.44
4	Present	19.660	25.573	43.090	64.048	99.380
	Ref.[2]	19.767	25.698	43.191	64.254	99.928
	dif.(%)	-0.55	-0.49	-0.23	-0.32	-0.55
5	Present	22.430	32.349	52.708	67.189	127.23
	Ref.[2]	22.521	32.425	53.000	67.467	127.69
	dif.(%)	-0.40	-0.24	-0.55	-0.41	-0.36
6	Present	25.954	48.281	63.763	107.75	134.76
	Ref.[2]	26.024	48.467	64.050	108.02	135.45
	dif.(%)	-0.27	-0.39	-0.45	-0.26	-0.51

Table 13 Frequency parameters $\Omega = \omega a (\rho h/D)^{1/2}$ for C-F-S-F plates.

mode	<i>a/b</i>	0.4	2/3	1	1.5	2.5
1	Present	15.316	15.258	15.192	15.115	15.012
	Ref.[2]	15.382	15.340	15.285	15.217	15.128
	dif.(%)	-0.43	-0.54	-0.61	-0.68	-0.77
2	Present	16.282	17.854	20.584	25.635	37.230
	Ref.[2]	16.371	17.949	20.673	25.711	37.294
	dif.(%)	-0.54	-0.53	-0.43	-0.30	-0.17
3	Present	19.607	26.689	39.736	49.231	48.870
	Ref.[2]	19.656	26.734	39.775	49.550	49.226
	dif.(%)	-0.25	-0.17	-0.10	-0.65	-0.73
4	Present	25.498	43.147	49.449	63.691	83.049
	Ref.[2]	25.549	43.190	49.730	64.012	83.325
	dif.(%)	-0.20	-0.10	-0.57	-0.50	-0.33
5	Present	34.314	49.605	56.280	68.083	102.43
	Ref.[2]	34.507	49.840	56.617	68.126	103.14
	dif.(%)	-0.56	-0.47	-0.60	-0.06	-0.69
6	Present	46.282	52.689	77.324	103.08	143.00
	Ref.[2]	46.435	53.013	77.368	103.70	143.68
	dif.(%)	-0.33	-0.61	-0.06	-0.60	-0.47

Table 12 Frequency parameters $\Omega = \omega a (\rho h/D)^{1/2}$ for C-F-C-F plates.

mode	<i>a/b</i>	0.4	2/3	1	1.5	2.5
1	Present	22.283	22.228	22.168	22.093	21.983
	Ref.[2]	22.346	22.314	22.272	22.215	22.130
	dif.(%)	-0.28	-0.39	-0.47	-0.55	-0.67
2	Present	22.991	24.193	26.407	30.784	41.568
	Ref.[2]	23.086	24.309	26.529	30.901	41.689
	dif.(%)	-0.41	-0.48	-0.46	-0.38	-0.29
3	Present	25.608	31.636	43.597	60.964	60.608
	Ref.[2]	25.666	31.700	43.664	61.303	61.002
	dif.(%)	-0.23	-0.20	-0.15	-0.56	-0.65
4	Present	30.574	46.754	61.176	70.869	92.032
	Ref.[2]	30.633	46.820	61.466	70.960	92.384
	dif.(%)	-0.19	-0.14	-0.47	-0.13	-0.38
5	Present	38.481	61.328	67.176	73.883	119.13
	Ref.[2]	38.687	61.566	67.549	74.259	119.88
	dif.(%)	-0.54	-0.39	-0.56	-0.51	-0.63
6	Present	49.680	64.004	79.817	118.08	156.95
	Ref.[2]	49.858	64.343	79.904	118.33	157.76
	dif.(%)	-0.36	-0.53	-0.11	-0.21	-0.51

Table 14 Frequency parameters $\Omega = \omega a (\rho h/D)^{1/2}$ for C-F-F-F plates.

mode	<i>a/b</i>	0.4	2/3	1	1.5	2.5
1	Present	3.4984	3.4846	3.4719	3.4551	3.4378
	Ref.[2]	3.5107	3.5024	3.4917	3.4772	3.4562
	dif.(%)	-0.35	-0.51	-0.57	-0.64	-0.54
2	Present	4.7672	6.3882	8.5065	11.658	17.967
	Ref.[2]	4.7861	6.4062	8.5246	11.676	17.988
	dif.(%)	-0.40	-0.28	-0.21	-0.16	-0.12
3	Present	8.0683	14.467	21.286	21.468	21.398
	Ref.[2]	8.1146	14.538	21.429	21.618	21.563
	dif.(%)	-0.57	-0.49	-0.67	-0.70	-0.77
4	Present	13.805	21.916	27.199	39.330	57.225
	Ref.[2]	13.882	22.038	27.331	39.492	57.458
	dif.(%)	-0.56	-0.56	-0.48	-0.41	-0.41
5	Present	21.523	25.914	30.958	53.542	60.130
	Ref.[2]	21.638	26.073	31.111	53.876	60.581
	dif.(%)	-0.53	-0.62	-0.49	-0.62	-0.75
6	Present	23.047	31.448	54.189	61.619	105.94
	Ref.[2]	23.731	31.618	54.443	61.994	106.54
	dif.(%)	-2.97	-0.54	-0.47	-0.61	-0.56

Table 15 Frequency parameters $\Omega = \omega a (\rho h/D)^{1/2}$ for S-S-F-F plates.

mode	<i>a/b</i>	0.4	2/3	1	1.5	2.5
1	Present	1.3198	2.2334	3.3676	5.0256	8.2505
	Ref.[2]	1.3201	2.2339	3.3687	5.0263	8.2506
	dif.(%)	-0.02	-0.02	-0.03	-0.01	0.00
2	Present	4.7308	9.5393	17.317	21.464	29.566
	Ref.[2]	4.7433	9.5749	17.407	21.544	29.646
	dif.(%)	-0.26	-0.37	-0.52	-0.37	-0.27
3	Present	10.316	16.679	19.293	37.527	64.473
	Ref.[2]	10.362	16.764	19.367	37.718	64.760
	dif.(%)	-0.45	-0.51	-0.39	-0.51	-0.44
4	Present	15.789	24.544	38.211	55.223	98.681
	Ref.[2]	15.873	24.662	38.291	55.490	99.206
	dif.(%)	-0.53	-0.48	-0.21	-0.48	-0.53
5	Present	18.845	26.994	51.035	60.736	117.78
	Ref.[2]	18.930	27.058	51.324	60.882	118.31
	dif.(%)	-0.45	-0.24	-0.57	-0.24	-0.45
6	Present	20.100	44.059	53.487	99.132	125.62
	Ref.[2]	20.171	44.172	53.738	99.388	126.07
	dif.(%)	-0.35	-0.26	-0.47	-0.26	-0.35

Table 17 Frequency parameters $\Omega = \omega a (\rho h/D)^{1/2}$ for F-F-F-F plates.

mode	<i>a/b</i>	0.4	2/3	1	1.5	2.5
1	Present	3.4328	8.9314	13.468	20.096	21.454
	Ref.[2]	3.4629	8.9459	13.489	20.128	21.643
	dif.(%)	-0.88	-0.16	-0.16	-0.16	-0.88
2	Present	5.2783	9.5171	19.596	21.413	32.987
	Ref.[2]	5.2881	9.6015	19.789	21.603	33.050
	dif.(%)	-0.19	-0.89	-0.99	-0.89	-0.19
3	Present	9.5407	20.599	24.270	46.347	59.628
	Ref.[2]	9.6220	20.735	24.432	46.654	60.137
	dif.(%)	-0.85	-0.66	-0.67	-0.66	-0.85
4	Present	11.329	22.182	34.801	49.910	70.803
	Ref.[2]	11.437	22.353	35.024	50.293	71.484
	dif.(%)	-0.96	-0.77	-0.64	-0.77	-0.96
5	Present	18.628	25.651	34.801	57.713	116.42
	Ref.[2]	18.793	25.867	35.024	58.201	117.45
	dif.(%)	-0.89	-0.84	-0.64	-0.84	-0.88
6	Present	18.923	29.791	61.093	67.030	118.27
	Ref.[2]	19.100	29.973	61.526	67.494	119.38
	dif.(%)	-0.94	-0.61	-0.71	-0.69	-0.94

Table 16 Frequency parameters $\Omega = \omega a (\rho h/D)^{1/2}$ for S-F-F-F plates.

mode	<i>a/b</i>	0.4	2/3	1	1.5	2.5
1	Present	2.6886	4.4774	6.6433	9.8458	14.813
	Ref.[2]	2.6922	4.4810	6.6480	9.8498	14.939
	dif.(%)	-0.14	-0.08	-0.07	-0.04	-0.85
2	Present	6.4730	12.943	14.902	14.888	16.238
	Ref.[2]	6.5029	13.009	15.023	15.013	16.242
	dif.(%)	-0.46	-0.51	-0.81	-0.84	-0.03
3	Present	12.574	15.571	25.376	33.913	48.443
	Ref.[2]	12.637	15.674	25.492	34.027	48.844
	dif.(%)	-0.50	-0.66	-0.46	-0.34	-0.83
4	Present	15.234	20.246	26.001	47.953	51.950
	Ref.[2]	15.337	20.373	26.126	48.332	52.089
	dif.(%)	-0.67	-0.63	-0.48	-0.79	-0.27
5	Present	17.371	30.391	48.449	54.781	96.684
	Ref.[2]	17.510	30.548	48.711	55.066	97.225
	dif.(%)	-0.80	-0.52	-0.54	-0.52	-0.56
6	Present	21.597	33.234	50.579	70.270	101.52
	Ref.[2]	21.699	33.411	50.849	70.695	102.34
	dif.(%)	-0.47	-0.53	-0.53	-0.60	-0.80

Table 18 Frequency parameters $\Omega = \omega a (\rho h/D)^{1/2}$ for S-S-S-S plates.

mode	<i>a/b</i>	0.4	2/3	1	1.5	2.5
1	Present	11.4488	14.2561	19.7392	32.076	71.5543
	Ref.[2]	11.4487	14.2561	19.7392	32.0762	71.5564
	dif.(%)	0.00	0.00	0.00	0.00	0.00
2	Present	16.1862	27.4155	49.3480	61.6849	101.164
	Ref.[2]	16.1862	27.4156	49.3480	61.6850	101.163
	dif.(%)	0.00	0.00	0.00	0.00	0.00
3	Present	24.0818	43.8649	49.3480	98.6960	150.511
	Ref.[2]	24.0818	43.8649	49.3480	98.6960	150.512
	dif.(%)	0.00	0.00	0.00	0.00	0.00
4	Present	35.1358	49.3480	78.9568	111.033	219.599
	Ref.[2]	35.1358	49.3480	78.9568	111.033	219.599
	dif.(%)	0.00	0.00	0.00	0.00	0.00
5	Present	41.0575	57.0244	98.6960	128.305	256.610
	Ref.[2]	41.0576	57.0244	98.6960	128.305	256.610
	dif.(%)	0.00	0.00	0.00	0.00	0.00
6	Present	45.7950	78.9568	98.6960	177.653	286.219
	Ref.[2]	45.7950	78.9568	98.6960	177.653	286.218
	dif.(%)	0.00	0.00	0.00	0.00	0.00

Table 19 Frequency parameters $\Omega = \omega a (\rho h/D)^{1/2}$ for S-C-S-C plates.

mode	<i>a/b</i>	0.4	2/3	1	1.5	2.5
1	Present	12.1347	17.3730	28.9509	56.3481	145.484
	Ref.[2]	12.1347	17.3730	28.9509	56.3481	145.484
	dif.(%)	0.00	0.00	0.00	0.00	0.00
2	Present	18.3647	35.3445	54.7431	78.9836	164.739
	Ref.[2]	18.3647	35.3445	54.7431	78.9836	164.739
	dif.(%)	0.00	0.00	0.00	0.00	0.00
3	Present	27.9657	45.4294	69.3270	123.172	202.227
	Ref.[2]	27.9657	45.4294	69.3270	123.172	202.227
	dif.(%)	0.00	0.00	0.00	0.00	0.00
4	Present	40.7500	62.0544	94.5853	146.268	261.105
	Ref.[2]	40.7500	62.0544	94.5853	146.268	261.105
	dif.(%)	0.00	0.00	0.00	0.00	0.00
5	Present	41.3782	62.3131	102.216	170.111	342.165
	Ref.[2]	41.3782	62.3131	102.216	170.111	342.144
	dif.(%)	0.00	0.00	0.00	0.00	0.01
6	Present	47.0009	88.8047	129.096	189.122	392.875
	Ref.[2]	47.0009	88.8047	129.096	189.122	392.875
	dif.(%)	0.00	0.00	0.00	0.00	0.00

Table 20 Frequency parameters $\Omega = \omega a (\rho h/D)^{1/2}$ for S-C-S-S plates.

mode	<i>a/b</i>	0.4	2/3	1	1.5	2.5
1	Present	11.7502	15.5783	23.6464	42.528	103.922
	Ref.[2]	11.7502	15.5783	23.6463	42.5278	103.923
	dif.(%)	0.00	0.00	0.00	0.00	0.00
2	Present	17.1872	31.0723	51.6742	69.0031	128.338
	Ref.[2]	17.1872	31.0724	51.6743	69.0031	128.338
	dif.(%)	0.00	0.00	0.00	0.00	0.00
3	Present	25.9171	44.5644	58.6463	116.267	172.380
	Ref.[2]	25.9171	44.5644	58.6464	116.267	172.380
	dif.(%)	0.00	0.00	0.00	0.00	0.00
4	Present	37.8317	55.3926	86.1345	120.996	237.250
	Ref.[2]	37.8317	55.3926	86.1345	120.996	237.250
	dif.(%)	0.00	0.00	0.00	0.00	0.00
5	Present	41.2071	59.4627	100.270	147.635	320.792
	Ref.[2]	41.2070	59.4627	100.270	147.635	320.792
	dif.(%)	0.00	0.00	0.00	0.00	0.00
6	Present	46.3620	83.6060	113.228	184.101	322.986
	Ref.[2]	46.3620	83.6060	113.228	184.101	322.964
	dif.(%)	0.00	0.00	0.00	0.00	0.01

Table 21 Frequency parameters $\Omega = \omega a (\rho h/D)^{1/2}$ for S-C-S-F plates.

mode	<i>a/b</i>	0.4	2/3	1	1.5	2.5
1	Present	10.1888	10.9752	12.6872	16.8219	30.6297
	Ref.[2]	10.1888	10.9752	12.6874	16.8225	30.6277
	dif.(%)	0.00	0.00	0.00	0.00	0.01
2	Present	13.6037	20.3357	33.0650	45.3022	58.0819
	Ref.[2]	13.6036	20.3355	33.0651	45.3024	58.0804
	dif.(%)	0.00	0.00	0.00	0.00	0.00
3	Present	20.0972	37.9553	41.7019	61.0178	105.548
	Ref.[2]	20.0971	37.9552	41.7019	61.0178	105.547
	dif.(%)	0.00	0.00	0.00	0.00	0.00
4	Present	29.6219	40.2717	63.0148	92.3072	149.457
	Ref.[2]	29.6219	40.2717	63.0148	92.3073	149.457
	dif.(%)	0.00	0.00	0.00	0.00	0.00
5	Present	39.6382	49.7317	72.3976	93.8294	173.106
	Ref.[2]	39.6382	49.7317	72.3976	93.8293	173.106
	dif.(%)	0.00	0.00	0.00	0.00	0.00
6	Present	42.2426	64.1890	90.6113	141.783	182.811
	Ref.[2]	42.2425	64.1889	90.6114	141.783	182.811
	dif.(%)	0.00	0.00	0.00	0.00	0.00

Table 22 Frequency parameters $\Omega = \omega a (\rho h/D)^{1/2}$ for S-S-S-F plates.

mode	<i>a/b</i>	0.4	2/3	1	1.5	2.5
1	Present	10.1258	10.6712	11.6846	13.7114	18.8017
	Ref.[2]	10.1259	10.6712	11.6845	13.7111	18.8009
	dif.(%)	0.00	0.00	0.00	0.00	0.00
2	Present	13.0570	18.2995	27.7563	43.5722	50.5404
	Ref.[2]	13.0570	18.2995	27.7563	43.5723	50.5405
	dif.(%)	0.00	0.00	0.00	0.00	0.00
3	Present	18.8390	33.6974	41.1966	47.8571	100.232
	Ref.[2]	18.8390	33.6974	41.1967	47.8571	100.232
	dif.(%)	0.00	0.00	0.00	0.00	0.00
4	Present	27.5580	40.1307	59.0655	81.4788	110.226
	Ref.[2]	27.5580	40.1307	59.0655	81.4789	110.226
	dif.(%)	0.00	0.00	0.00	0.00	0.00
5	Present	39.3389	48.4082	61.8606	92.6924	147.632
	Ref.[2]	39.3377	48.4082	61.8606	92.6925	147.632
	dif.(%)	0.00	0.00	0.00	0.00	0.00
6	Present	39.6119	57.5930	90.2941	124.563	169.103
	Ref.[2]	39.6118	57.5929	90.2941	124.564	169.103
	dif.(%)	0.00	0.00	0.00	0.00	0.00

Table 23 Frequency parameters $\Omega = \omega a (\rho h/D)^{1/2}$ for S-F-S-F plates.

mode	a/b	0.4	2/3	1	1.5	2.5
1	Present	9.75995	9.6984	9.63127	9.55886	9.48072
	Ref.[2]	9.7600	9.6983	9.6314	9.5582	9.4841
	dif.(%)	0.00	0.00	0.00	0.01	-0.04
2	Present	11.0369	12.9812	16.135	21.6194	33.6228
	Ref.[2]	11.0368	12.9813	16.1348	21.6192	33.6228
	dif.(%)	0.00	0.00	0.00	0.00	0.00
3	Present	15.0626	22.9535	36.7257	38.7216	38.3628
	Ref.[2]	15.0626	22.9535	36.7256	38.7214	38.3629
	dif.(%)	0.00	0.00	0.00	0.00	0.00
4	Present	21.7065	39.1052	38.9450	54.8443	75.2042
	Ref.[2]	21.7064	39.1052	38.9450	54.8443	75.2037
	dif.(%)	0.00	0.00	0.00	0.00	0.00
5	Present	31.1779	40.3560	46.7381	65.7921	86.9680
	Ref.[2]	31.1771	40.3560	46.7381	65.7922	86.9684
	dif.(%)	0.00	0.00	0.00	0.00	0.00
6	Present	39.2387	42.6847	70.7401	87.6262	130.358
	Ref.[2]	39.2387	42.6847	70.7401	87.6262	130.358
	dif.(%)	0.00	0.00	0.00	0.00	0.00

As seen in the table, all the differences are between -0.10% -0.02%, and all the present values are very slightly lower than those in Ref.[2], and due to the fact that all the present solution satisfies exactly the kinematical condition at the edges, it is observed that the present results are more accurate and closer to the exact values (assuming that they exist). The mode numbers (i.e., number of half-waves in the mode shape) are listed for each frequency in Ref.[2].

Tables 4 to 17 are in the same format as in Table 3, and the frequency parameters are tabulated for fourteen sets of edge conditions, where the exact solutions are not available due to the condition that two opposite edges are not simply supported (non-Levy type problem).

In all pairs of the present and reference values (i.e., 450 pairs= (5 aspect ratios)×(6 modes)×(15 tables)), all the differences are negative (the present values are lower) and the differences are all within one percent.

3.3. Comprehensive Results for Levy Type Problem

It is widely known that the exact solution is available for vibration of isotropic rectangular plates when a pair of opposite edges are simply supported. The solution is already presented in Ref. [2]. This means that it is not necessary to use approximate method to calculate natural frequencies. In this paper, however, six tables are prepared in the same format to demonstrate that this Ritz solution can provide frequency parameters in the accuracy with same degree. The present results are given with six

Table 24 Correspondance of the present tables with those in Ref.[2].

Present tables	Tables in Ref.[2]	Representing B.C.	B.C.s to give the identical frequency parameters
(1) Plates <i>not</i> having two opposite edges simply supported			
Table 3	C1	C-C-C-C	
Table 4	C2	C-C-C-S	S-C-C-C, C-S-C-C, C-C-S-C
Table 5	C3	C-C-C-F	F-C-C-C, C-F-C-C, C-C-F-C
Table 6	C4	C-C-S-S	S-S-C-C, S-C-C-S, C-S-S-C
Table 7	C5	C-C-S-F	F-S-C-C, F-C-C-S, S-F-C-C, S-C-C-F, C-F-S-C, C-S-F-C, C-C-F-S
Table 8	C6	C-C-F-F	F-F-C-C, F-C-C-F, C-F-F-C
Table 9	C7	C-S-C-F	F-C-S-C, S-C-F-C, C-F-C-S
Table 10	C8	C-S-S-F	F-S-S-C, F-C-S-S, S-F-C-S, S-S-F-C, S-S-C-F, S-C-F-S, C-F-S-S
Table 11	C9	C-S-F-F	F-F-S-C, F-F-C-S, F-S-C-F, F-C-S-F, S-F-F-C, S-C-F-F, C-F-F-S
Table 12	C10	C-F-C-F	F-C-F-C
Table 13	C11	C-F-S-F	F-S-F-C, F-C-F-S, S-F-C-F
Table 14	C12	C-F-F-F	F-F-F-C, F-F-C-F, F-C-F-F
Table 15	C13	S-S-F-F	F-F-S-S, F-S-S-F, S-F-F-S
Table 16	C14	S-F-F-F	F-F-F-S, F-F-S-F, F-S-F-F
Table 17	C15	F-F-F-F	
(2) Plates having two opposite edges simply supported			
Table 18	A1	S-S-S-S	
Table 19	A2	S-C-S-C	C-S-C-S
Table 20	A3	S-C-S-S	S-S-S-C, S-S-C-S, C-S-S-S
Table 21	A4	S-C-S-F	F-S-C-S, S-F-S-C, C-S-F-S
Table 22	A5	S-S-S-F	F-S-S-S, S-F-S-S, S-S-F-S
Table 23	A6	S-F-S-F	F-S-F-S

significant figures, and compared to the exact values in Ref. [2].

Tables 18 to 23 list up the frequency parameters for rectangular plates with S-S-S-S, S-C-S-C, S-C-S-S, S-C-S-F, S-S-S-S-F and S-F-S-F, respectively. Among 180 pairs of the present and exact frequencies (i.e., 180 pairs= (5 aspect ratios)×(6 modes)×(6 tables)), almost all pairs show the exact match with six significant figures, only with four exceptions showing very slight difference over 0.01 percent.

Table 24 provides classification of physically meaningful sets of edge conditions to give the identical natural frequencies. For example in this table, “Table 4” gives the frequency parameters of C-C-C-S plate and the results are identical with S-C-C-C, C-S-C-C and C-C-S-C.

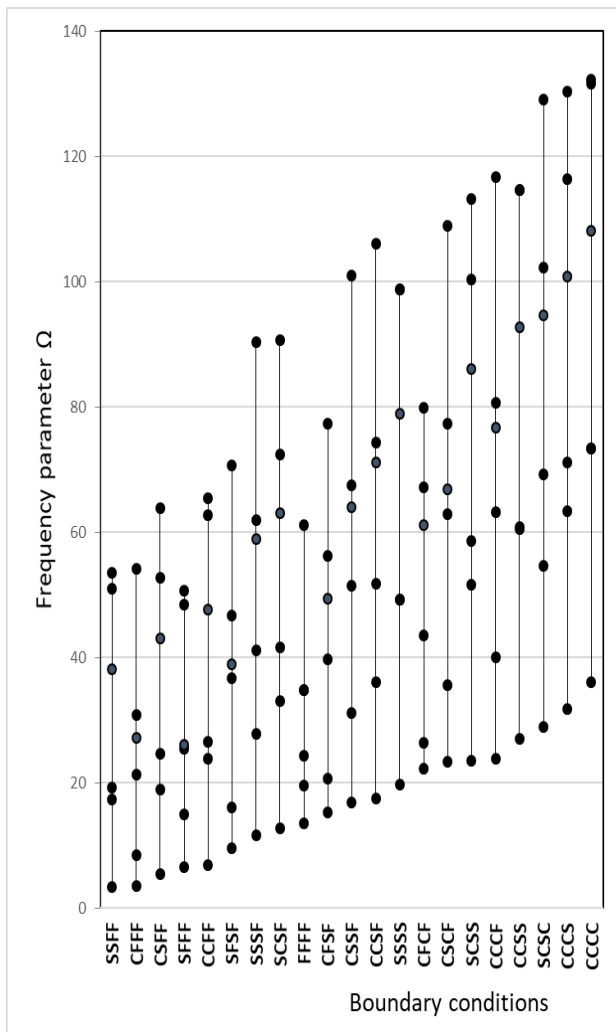


Figure 2. Distribution of lowest six frequency parameters of square plates with twenty-one sets of boundary conditions

Figure 2 presents the distribution of lowest six frequency parameters of square plates for twenty-one sets of boundary conditions. The boundary conditions are aligned in the increasing order of the fundamental frequencies, and the fundamental frequencies may appear almost linearly increasing. Among them, SFFF and FFFF plates have rigid body motions and only the self-equilibrium modes (i.e., modes with some nodal lines) exist. Also, SSSS, CCSS and CCCC plates may appear to have only four distinct modes because two modes include a pair of identical frequencies, and FFFF plate does five distinct modes due to the same reason.

4. Conclusions

The aim of this study was to establish a new standard for natural frequencies of isotropic rectangular plates and to summarize the lists of frequencies for all possible combinations of three classical boundary conditions (i.e., free, simply supported and clamped edges). After the accuracy of the Ritz solution was established for non-Levy type problems (i.e., plates not having two opposite sides simply supported), these frequency parameters were given in five significant figures in the lists and were compared to the other list [2]. The differences were all less than one-

percent. For Levy type (i.e., plates with two opposite sides simply supported) problems where the exact solutions are available, two sets of frequency parameters were in good agreement showing the differences lower than 0.001 percent.

The present results for most commonly needed information in mechanical vibration will be valuable standard for comparison with numerical methods in future studies and design data.

Acknowledgement

This author expresses his gratitude to the Japan Society for the Promotion of Science (JSPS) for the Funding Program MEXT/JSPS KAKENHI Grant Number 21K03957.

References

1. Leissa AW, Vibration of Plates, NASA-SP-160, 1969. <https://ntrs.nasa.gov/citations/19700009156>
2. Leissa AW, The free vibration of rectangular plates, *J. Sound Vib.*, 31(1973), 257-293.
3. Blevins RD, Formulas for natural frequency and mode shape, Krieger Pub. Com. (2001).
4. Young D, Vibration of rectangular plates by the ritz method, *Trans. ASME J. Applied Mechanics*, 17 (1950), 448-453.
5. Gorman DJ, Free vibration analysis of cantilever plates by the method of superposition, *J. Sound Vibr.*, 49 (1976), 453-467.
6. Gorman DJ, Free-vibration analysis of rectangular plates with clamped-simply supported edge conditions by the method of superposition, *Trans. ASME, J. Applied Mech.*, 44 (1977), 743-749.
7. Gorman DJ, Free vibration analysis of the completely free rectangular plates by the method of superposition, *J. Sound Vibr.*, 57 (1978), 437-447.
8. Narita Y, Free vibration of elastic plates with various shapes and boundary conditions, Doctoral Dissertation, Hokkaido University (1980), <https://eprints.lib.hokudai.ac.jp/dspace/handle/2115/32630>
9. Leissa AW, Plate vibration research 1976-1980: classical theory, *Shock Vib. Dig.*, 13-9 (1981), 11-22.
10. Leissa AW, Recent studies in plate vibrations: 1981-85, Part.1 classical theory, 1981-85, *Shock Vib. Dig.*, 19-2 (1987), 11-18.
11. Ramu I, Mohanty SC, Study on free vibration analysis of rectangular plate structures using finite element method, *Procedia Eng.* 38 (2012), 2758-2766.
12. Senjanovic I, Tomic M, Vladimir N, Hadzic N, an analytical solution to free rectangular plate natural vibrations by beam modes-ordinary and missing plate modes, *Trans. FAMENA* 40 (2016), 1-18.
13. Narita Y, Combinations for the free-vibration behaviors of anisotropic rectangular plates under general edge conditions, *Trans. ASME, J. Appl. Mech.*, 67 (2000), 568-573.
14. Narita Y, Polya counting theory applied to combination of edge conditions for generally shaped isotropic plates, *EPI Int. J. Eng.*, 2 (2019), 194-202.
15. Narita Y, Robinson P, Maximizing the fundamental frequency of laminated cylindrical panels using layerwise optimization, *Intl. J. Mech. Sci.*, 48 (2006) 1516-1524.
16. Narita D, Narita, Y., Accurate results for free vibration of doubly curved shallow shells of rectangular planform (Part 1), *EPI Int. J. Eng.*, 4 (2021), 29-36.

Characteristic of Vibration Signal from Cutting Tool Against Steel with a Tensile Strength of 60 for CNC Turning Monitoring System

Muh Fachrul^{a,*}, Ahmad Yusran Aminy^b, Azwar Hayat^c

^aMachine Maintenance and Repair Study Program, Polytechnic of Bosowa. Email: mfachrul79@gmail.com

^bDepartment Mechanical Engineering, Engineering Faculty, Hasanuddin University. Email: ahmadyusran179@gmail.com

^cDepartment Mechanical Engineering, Engineering Faculty, Hasanuddin University. Email: azwar.hayat@unhas.ac.id

Abstract

The condition of the insert significantly affects the product quality and manufacturing efficiency of lathe machining. The current study uses the power spectral density distribution of a signal vibration accelerometer machine built for CNC in developing a system to classify various conditions that can occur in a manufacturing environment. For four common lathe machining insert conditions (i.e., built-up edge, flank wear, standard, and fracture), In this case, the insert condition classification system is created with two stages—insert condition modeling and machining model fusion. At the stage of modeling the insert condition, the magnitude feature of the segmented frequency is captured according to the power spectral density distribution of the accelerometer vibration signal. Root mean square (RMS) and Fast Fourier Transform (FFT) was calculated to conduct vibration prediction studies using a turning cutting tool. The results of the raw signal in the experimental new conditions show the RMS value is in the range of 6.24-6.23 mV, and the FFT is 0.0007-0.0009 mV. In good condition, the raw signal condition shows that the RMS value is 54.36-67.08 mV and FFT 0.0068-0.0080 mV. In the middle state of the raw signal, the RMS value is 83.05-112.07mV, and the FFT value is 0.0089-0.0147mV. In poor condition raw signal, the RMS value is 125.14-152.09 mV, and the value FFT is at 0.0137-0.0178. The data clusters are well grouped and directly proportional between the damage to the tool blade and the increased voltage in RMS.

Keywords: CNC turning, cutting tool, vibration

1. Introduction

In recent years, the development of the global manufacturing industry has become more competitive and more important than ever in improving production efficiency, quality products, and cutting costs. The cutting tool cost is one of the most significant manufacturing expenses in the high-speed CNC sector. On the other hand, cutting tool wear is an unavoidable and widespread problem that directly impacts surface quality and dimensional accuracy. To increase productivity and ensure the quality of the workpiece, an effective and reliable working system is needed that can constantly monitor the condition of the tools [1], [2]. CNC machine tools are machine tools that, in the workpiece soldering process by a cutting tool, are assisted by computer numerical control or CNC (Computer Numerical Control). CNC agreed to use a coordinate system to drive the tool on the machine tool. The coordinate system on a CNC lathe is a cartesian

coordinate system with two axes: the X-axis and the Z-axis. The zero points present on CNC lathes are the Machine zero point (M) and the zero point of the workpiece (W) [3].

The geometry/shape of the lathe cutting tool mainly depends on the workpiece material and the tool material. Types of lathe-cutting tools It is generally divided into 2; namely, single cut edged lathe cutting tools and inserted lathe-cutting tools. For single-edged lathe-cutting tools are usually used in conventional lathes. This cutting tool material is high-speed steel (HSS), and the cutting tool angle is formed using a sharpening tool grinder machine [4].

In machining technology, one of the most significant criteria considered when assessing the quality of parts is confirmed as better surface roughness. So, to obtain the required level of surface quality of the machine components, the tool's vibration must be minimized to the slightest degree. In the machining process, the most critical parameters affecting surface roughness, tool wear, and vibration are turning factors such as axial feed rate, depth of cut, and rotational speed [5].

*Corresponding author. Tel.: +6285342017944
Jl Babussalam II
Makassar, Indonesia, 92161

The interaction between the cutting tool and the turning machine will cause wear and even damage to the cutting tool. So, that tool wear affects the quality of surface roughness, dimensional accuracy, and operating costs in the machining proses [6]. Advanced Manufacturing Technology (AMT) development aims to improve product quality. The implementation of Tool condition machining (TCM) is the most crucial part of AMT[7][8]. The procedures carried out in CNC machining and flexible manufacturing systems (FMS) have made TCM even more pertinent [9]. In response to this problem, a study of TCM technology has been carried out. The TCM system mainly uses sensor information collected during the cutting process to monitor the condition of the tool in real time and then predict the time it will take to replace the device while ensuring product quality and extending the tool usage time. With the popularity of flexible manufacturing systems and the emergence of intelligent manufacturing systems and computer-integrated manufacturing systems [10], [11].

In this study, the interaction between the lathe-cutting tool and the workpiece has been identified. The vibration results produced by the lathe-cutting device are expressed in the Root Mean Square (RMS) parameter. Based on the study of tool life, surface finishing, and vibration when rotating nodular cast iron using tool ceramics. They concluded that the surface finish was almost constant with the development of flank wear under different cutting conditions. They also observed that vibration during cutting decreased with increasing speed at low cutting depths, vibrations remaining almost constant with increased flank wear [12]. As the primary cause of tool failure, flank wear is short of wear that is intended to be the criterion in evaluating the tool life [2], [13]–[15].

2. Research Method

2.1. Material and Parameters

The workpiece in use is made of medium carbon steel with tensile strength, namely ST60, and a round bar shape with a size of 1 inch. The insert cutting tool uses the MCLN carbide lathe type with the rake angle tool -7° and the Relive Angel Tool 7° Style L - Negative 5° End or Side Cutting Edge Angle for negative 80° diamond.

The turning process is carried out using test parameters: a spindle speed of 1128 rpm, a feed rate of 50 mm/minute, and a depth of cut of 0.5 mm, as shown in Table 1.

2.2. Scheme of the Experiment

The turning process stage is categorized into three parts of cutting tool condition: good condition, middle

Table 1. Test parameters

Parameter	Symbols	Units	Value
Spindel Speed	V	rpm	1128
Feed rate	F	Minute	50
Dept of cut	D	mm	0.5

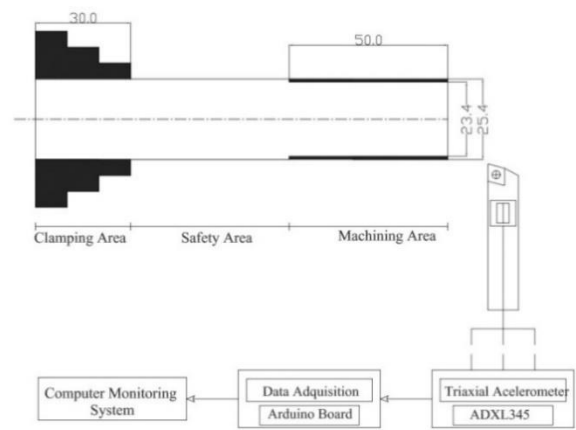


Figure 1. Machining scheme

condition, and poor condition. Before carrying out the workpiece sharpening process, first, take the machine vibration data during the condition without the ignition, which is written as the conditions of the news; each has a different vibration value. The projection of the resulting vibration is indicated in the parameters of time (minute) and amplitude (mm). Then the vibration data is processed using the RMS approach to make it easier to identify the vibration analysis results in each cutting tool condition. Figure 1 is the machining scheme used in this research.

2.3. Experimental Setup

Some of the components used in the experiment test are the accelerometer sensor, which is an essential part of reading the vibration results produced in the turning process. Cutting tools are used to wrench the workpiece; each feeding process is carried out by turning as far as 50 mm. A workpiece is a feeding object using a metal material shaft ST 60.

The cutting tool with the insert cutting tool uses the MCLN carbide lathe type. The shape and coding of the insert cutting tool and its cutting tool holder have been standardized by ISO. The insert cutting tool produced by the maker has a specific color code according to the material of the workpiece to be machined and the cutting conditions. The blue color code is for working steel, the yellow color code is for working stainless steel, and the red color code is for cast ironwork, as shown in Fig. 2. Usually, cutting data is included in the cutting tool insert packaging [16].

Grade	ISO	Range of applications	Group of materials										Application					
			P	M	K	N	S	H	T	M	D	S	G	P				
LC215B	HC-P15											●						
	HC-K15											●						
LC225C	HC-P25											●						
	HC-M25											●						
LC235C	HC-P35											●						
	HC-M35											●						
LC435D	HC-M35											●						
	HC-P35											●						
LC610A	HC-K10											●	●					
LC610M	HC-K10											●	●					
LW610	HW-K10											●	●	●	●	●	●	●

Figure 2. Lathe tool number code

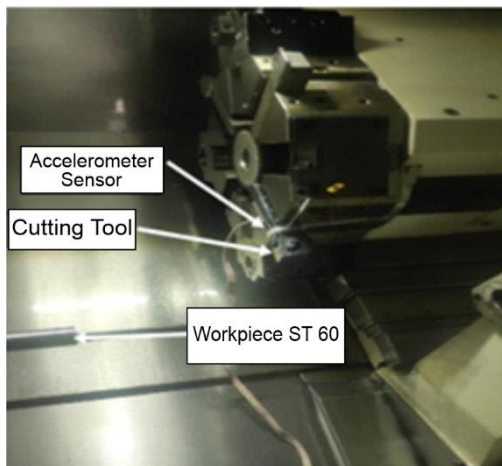


Figure 3. CNC machined parts

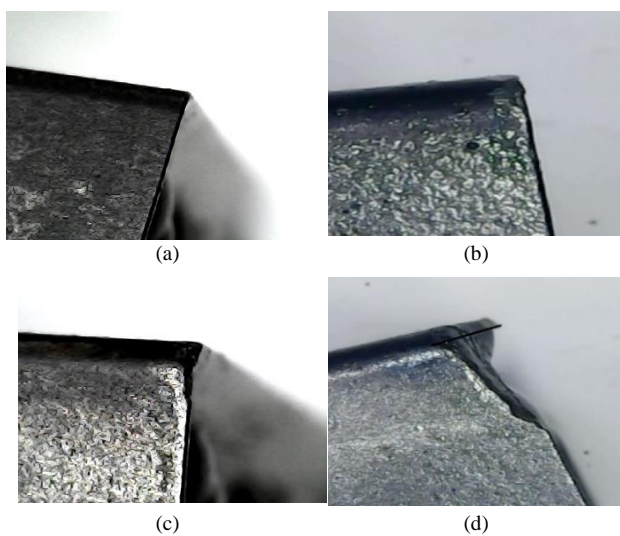


Figure 4. (a) new condition; (b) good condition; (c) middle condition; (d) poor condition

The processing of cutting on a CNC machine has several parts, as shown in Fig. 3.

3. Results and Discussion

Root mean square (RMS) and Fast Fourier Transform (FFT) was calculated to conduct vibration prediction studies using turning cutting tools. Experimental results show that predictions using Raw Signal values have high accuracy and accuracy compared to fast Fourier Transform (FFT) signal results.

3.1. Characteristic

The characteristics of a lathe cutting tool with a worn condition have a flank wear structure with a rough surface.

3.2. Raw Signal Condition

Based on trials that have been carried out by classifying cutting tool conditions. Then obtained, the results of each RMS are as follows in Eq. 1.

$$V_{rms} = \sqrt{\frac{1}{b-a} \int_a^b f^2(t) dt} \tag{1}$$

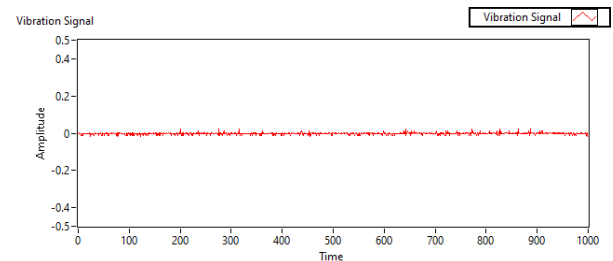
The experimental results are stated in Table 2.

Table 2. RMS data on tool condition

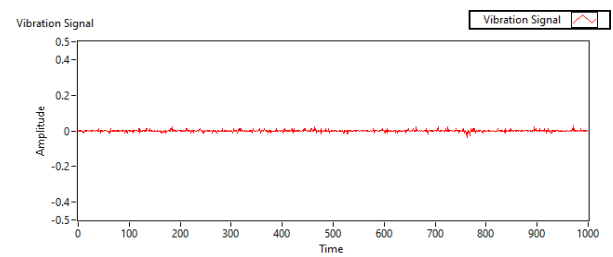
Condition	Experiment	Flank wear (mm)	V _{rms} (mV)	Range (mV)
New Conditions	1	-	6.24	
	2	-	6.26	6.24 - 6.23
	3	-	6.23	
Good condition	4	0	54.36	
	5	0.055	59.36	54.36 - 67.08
	6	0.09	67.08	
Middle condition	7	0.103	83.05	
	8	0.179	88.74	83.05 - 112.07
	9	0.243	112.07	
Poor condition	10	0.307	125.14	
	11	0.324	127.14	125.14 - 152.09
	12	0.304	152.09	

Table 2 shows that to see the RMS value, four tool conditions are given: new condition, good condition, middle condition, and poor condition. The state of the tool is seen from the degree of wear on the tool's flank wear structure. Experiments were carried out three times in data collection to see the repetitive comparison of RMS values. From the table, it can be seen that each tool has almost the same value in each experiment. However, in poor condition, the 12 data has a value of 152.09 mV, which is very different from the 10 and 11 data, namely 125.14 mV and 127.14 mV.

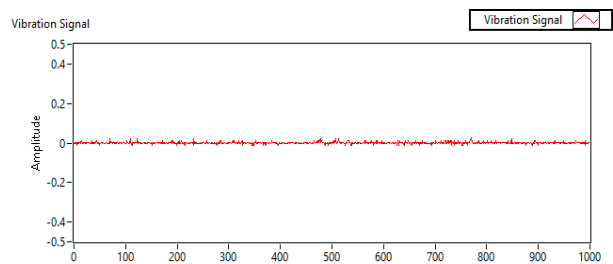
Figure 5 shows the results of vibration in raw signal on the new condition, divided into three experiments.



(a)



(b)



(c)

Figure 5. Results of vibration measurement on the new condition (a) Experiment 1; (b) Experiment 2; (c) Experiment 3

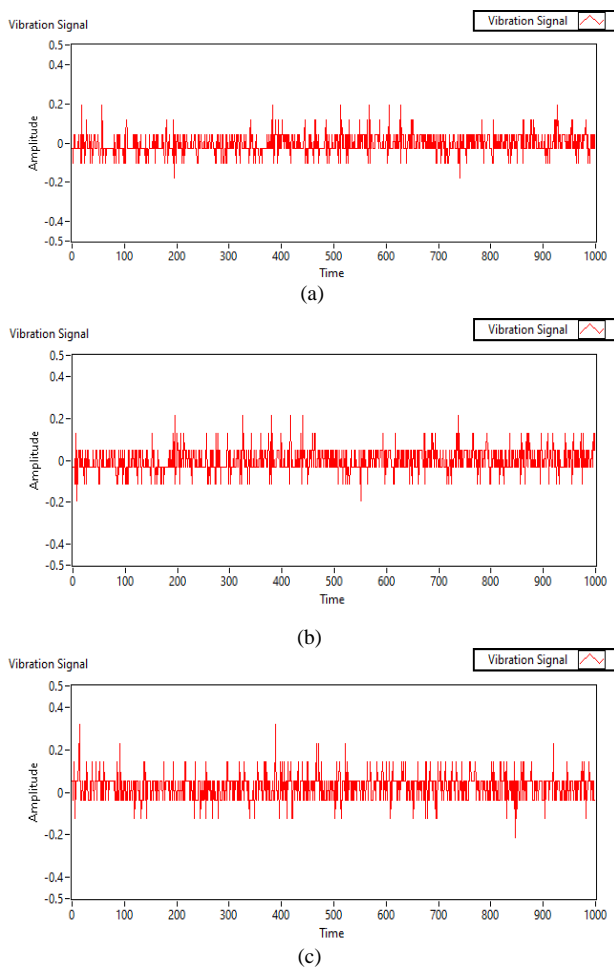


Figure 6. Results of vibration measurement of the tool in good condition (a) experiment 4; (b) experiment 5; (c) experiment 6

Figure 5 shows the results of direct vibration measurements on a newly raw signal using new condition cutting tools by repeating the experiment three times. The first experiment showed the results of the RMS value of 6.24mV, the second with 6.26mV results, and the third with 6.23mV.

Figure 6 shows the results of the vibration measurement of the tool in good condition, divided into three experiments. In this experiment, the amplitude value increased and showed RMS values in the range of 54.36mV to 67.08mV.

Figure 7 shows the results of direct vibration measurements using cutting tools in the middle condition divided into three experiments. In this experiment, the amplitude value increased from RMS 83.05mV to 112.07mV. Directly proportional to the increase in value Flank wear (VB) 0.103mm to 0.243mm.

Figure 8 shows the vibration measurement results on the cutting tool in poor condition, divided into three experiments. In this condition, the wave height reaches 0.5 amplitude, so if you enter the RMS equation, you will get a value of 125.14mV to 152.09mV. This increase is quite severe compared to using a good condition chisel with an amplitude value of 0.1 with an RMS range of 54.36mV to 67.08mV.

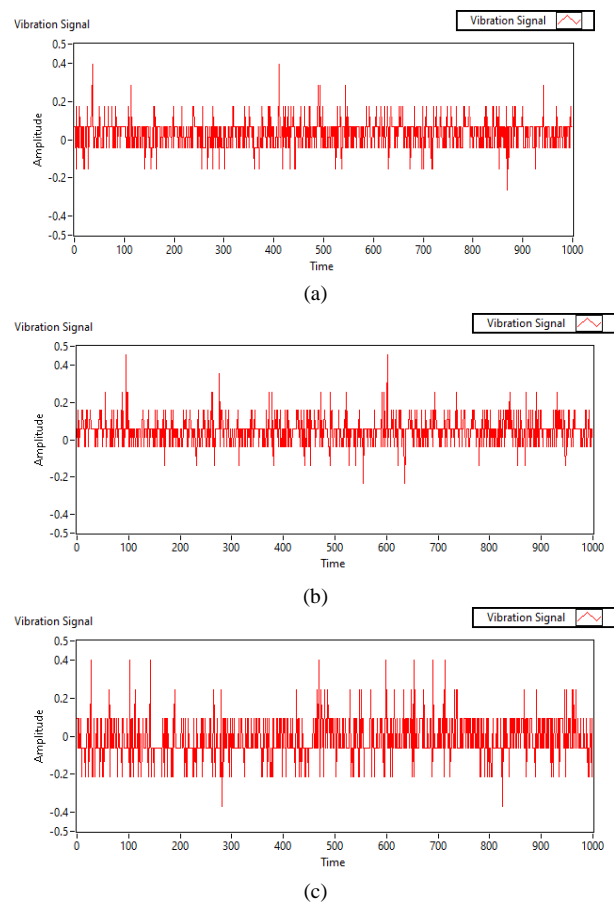


Figure 7. Results of vibration measurement on the cutting tool with middle conditions (a) experiment 7; (b) experiment 8; (c) experiment 9.

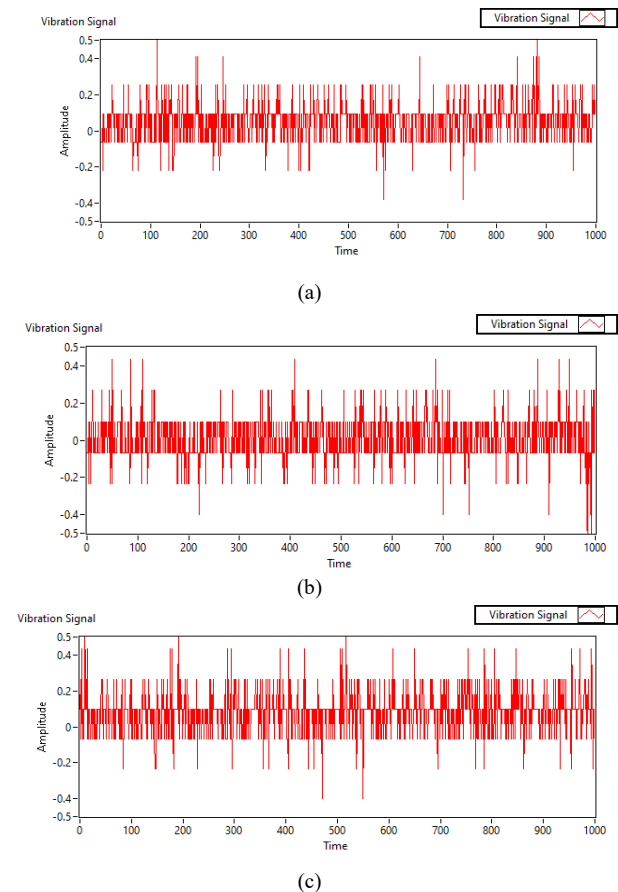


Figure 8. Results of vibration measurement on the cutting tool with poor conditions (a) experiment 10; (b) experiment 11; (c) experiment 12

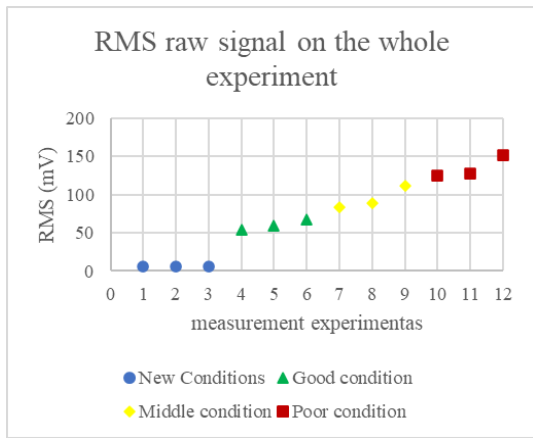


Figure 9. RMS raw signal value on the whole experiment

When considered, the form of data obtained shows that increased damage to the cutting tool eye will be directly proportional to the increase in the voltage of the RMS obtained. And when observed, each condition forms the voltage range of RMS that does not intersect between each cutting tool condition (clusterization). Figure 9 shows the RMS raw signal value.

3.3. Fast Fourier Transform (FFT) Signal

This research study conducted the Fast Fourier Transform signal analysis method to compare the results of Raw and Fast Fourier Transform vibration signals. The FFT signal plot in Table 3 shows the FFT data in the four conditions.

Figure 10 shows the results of the raw signal change to a fast Fourier transform (FFT) using a cutting tool with a new condition, and the RMS value is in the range of 0.0007mV to 0.0009mV.

Figure 11 shows the results of raw signal changes to a fast Fourier transform (FFT) using a good condition chisel, and the flank wear level increases to 0.09mm in direct proportion to the increase in the RMS value in the range 0.0068mV to 0.0080mV.

Table 3. FFT data

Condition	Experiment	Flank wear (mm)	Magnitude (mV)	Range (mV)
New Conditions	1	-	0.0007	0.0007 - 0.0009
	2	-	0.0009	
	3	-	0.0009	
Good condition	4	0	0.0068	0.0068 - 0.0080
	5	0.055	0.008	
	6	0.09	0.007	
Middle condition	7	0.103	0.0089	0.0089 - 0.0147
	8	0.179	0.0105	
	9	0.243	0.0147	
Poor condition	10	0.307	0.0137	0.0137 - 0.0178
	11	0.324	0.0149	
	12	0.304	0.0178	

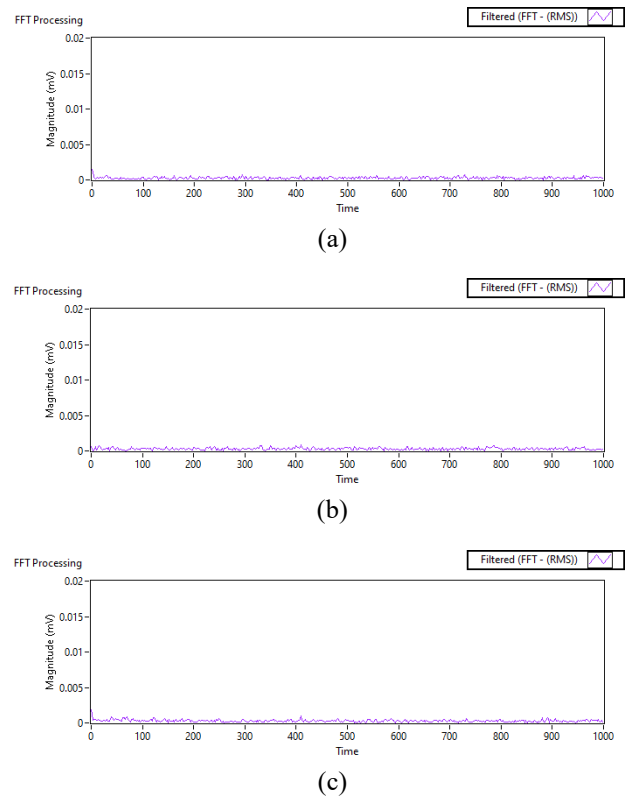


Figure 10. Signals of FFT process results under new conditions (a) experiment 1; (b) experiment 2; (c) experiment 3

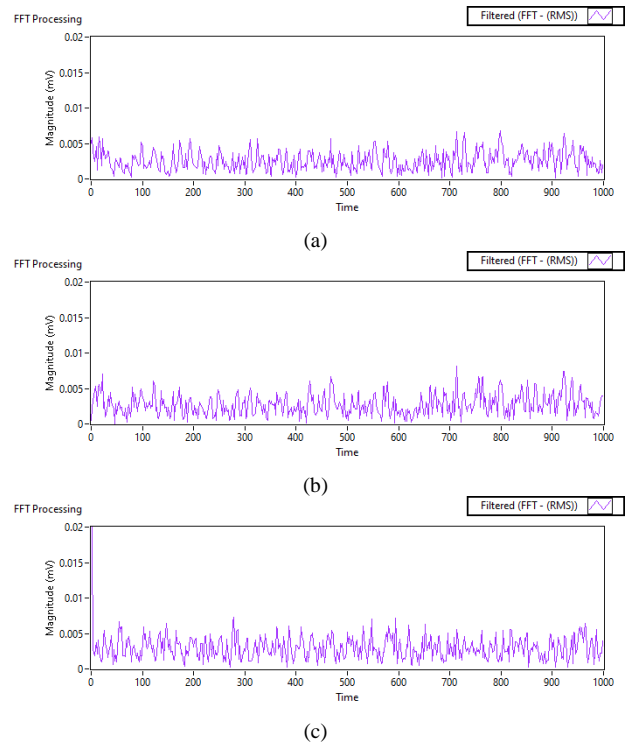


Figure 11. Signals of FFT process results under suitable conditions (a) experiment 4; (b) experiment 5; (c) experiment 6

Figure 12 shows the results of raw signal changes to the fast Fourier transform (FFT) using the cutting tool of the middle condition. The increase in flank wear of experiment 7 at 0.103mm is directly proportional to the increase in the RMS value of 0.0068mV, and experiment 9 with the Flank wear value of 0.243mm shows an increase in the RMS value of 0.0147mV.

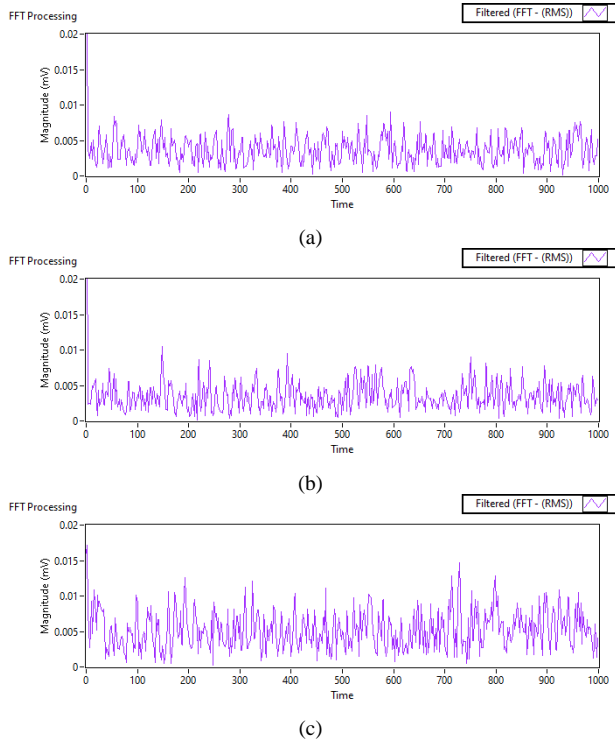


Figure 12. Signals of FFT process results under middle conditions (a) experiment 7; (b) experiment 8; (c) experiment 9

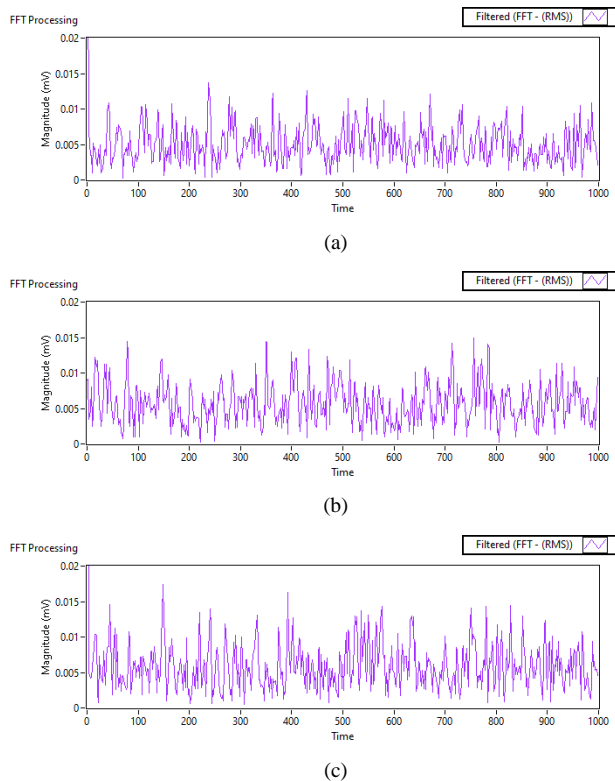


Figure 13. Signals of FFT process results under poor conditions (a) experiment 10; (b) experiment 11; (c) experiment 12

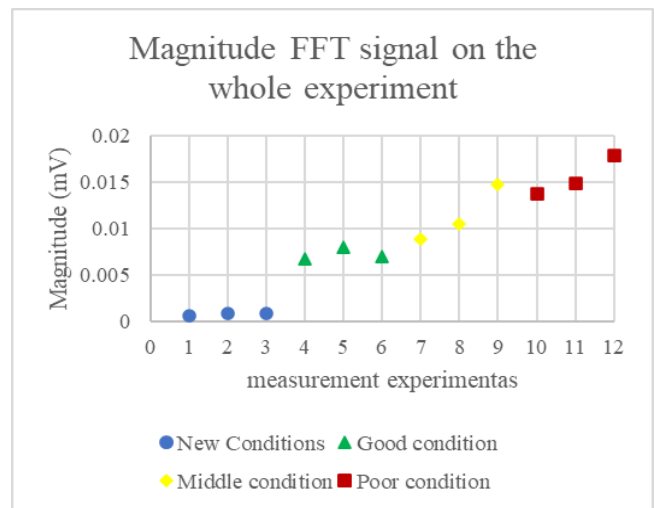


Figure 14. FFT signal condition

Figure 13 shows the results of raw signal changes to a Fast Fourier Transform (FFT) using a cutting tool in poor condition in experiment 10 with a flank wear value of 0.307mm while the RMS value decreased by 0.0137mV from 0.0147 in experiment 9. And it increased again in experiment 11 with flank wear of 0.324mm and an RMS value of 0.0149 mV.

Figure 14 is the overall FFT signal condition. The chart shows that each experiment's range of FFT values shows an increase in the range of damaged tool conditions and a decrease from 0.0089 mV until 0.0147 to a range of damaged tools from 0.0137 mV until 0.0178. the experiment is an imbalance in the data condition poor ten, whose value is in the middle condition range, and condition nine, which is in the damaged condition range. The data obtained show that the increase in magnitude is not always directly proportional to the damage to the tool.

Compared to previous studies using a prediction approach with FFT results[3], the prediction method with RMS values can provide more accurate and linear prediction results because the increase in tool damage will be linear with the increase in the RMS value obtained.

4. Conclusion

Based on the raw signal chart above, it is a combined result of raw signal testing from three cutting tool eye conditions by taking samples from as many as three experiments. The graph explains the increase in RMS values that occurs, depending on the degree of damage to the cutting tool. The greater the degree of damage will affect the degree of magnitude of the RMS value. When considered, the rated voltage value on the raw signal gives a greater value when compared to the measured magnitude value in the FFT process. This improves the reading of the value on the raw signal due to the wide range of reading values obtained.

References

[1] B. Chen, X. Chen, B. Li, Z. He, H. Cao, and G. Cai, "Reliability estimation for cutting tools based on logistic regression model using vibration signals," *Mech. Syst. Signal Process.*, vol. 25, no. 7, pp. 2526–2537, 2011, doi: 10.1016/j.ymssp.2011.03.001.

- [2] D. E. Dimla and P. M. Lister, "On-line metal cutting tool condition monitoring. I: force and vibration analyses," *Int. J. Mach. Tools Manuf.*, vol. 40, no. 5, pp. 739–768, 2000, doi: 10.1016/S0890-6955(99)00084-X.
- [3] E. García Plaza, P. J. Núñez López, and E. M. Beamud González, "Efficiency of vibration signal feature extraction for surface finish monitoring in CNC machining," *J. Manuf. Process.*, vol. 44, pp. 145–157, Aug. 2019, doi: 10.1016/j.jmapro.2019.05.046.
- [4] S. Swain, I. Panigrahi, A. K. Sahoo, A. Panda, and R. Kumar, "Effect of Tool Vibration on Flank Wear and Surface Roughness During High-Speed Machining of 1040 Steel," *J. Fail. Anal. Prev.*, vol. 20, no. 3, pp. 976–994, 2020, doi: 10.1007/s11668-020-00905-x.
- [5] N. Ambhore, D. Kamble, S. Chincharikar, and V. Wayal, "Tool condition monitoring system: A review," *Mater. Today Proc.*, vol. 2, no. 4–5, pp. 3419–3428, 2015, doi: 10.1016/j.matpr.2015.07.317.
- [6] B. Kilundu, P. Dehombreux, and X. Chimentin, "Tool wear monitoring by machine learning techniques and singular spectrum analysis," *Mech. Syst. Signal Process.*, vol. 25, no. 1, pp. 400–415, 2011, doi: 10.1016/j.ymsp.2010.07.014.
- [7] M. A. F. Ahmad, M. Z. Nuawi, S. Abdullah, Z. Wahid, Z. Karim, and M. Dirhamsyah, "Development of tool wear machining monitoring using novel statistical analysis method, I-kaz™," *Procedia Eng.*, vol. 101, no. C, pp. 355–362, 2015, doi: 10.1016/j.proeng.2015.02.043.
- [8] B. Sick, "On-line and indirect tool wear monitoring in turning with artificial neural networks: A review of more than a decade of research," *Mech. Syst. Signal Process.*, vol. 16, no. 4, pp. 487–546, 2002, doi: 10.1006/mssp.2001.1460.
- [9] D. R. Salgado and F. J. Alonso, "Tool wear detection in turning operations using singular spectrum analysis," *J. Mater. Process. Technol.*, vol. 171, no. 3, pp. 451–458, 2006, doi: 10.1016/j.jmatprotec.2005.08.005.
- [10] C. Zhang, X. Yao, J. Zhang, and H. Jin, "Tool condition monitoring and remaining useful life prognostic based on wireless sensor in dry milling operations," *Sensors (Switzerland)*, vol. 16, no. 6, 2016, doi: 10.3390/s16060795.
- [11] J. Zhou, P. Li, Y. Zhou, B. Wang, J. Zang, and L. Meng, "Toward New-Generation Intelligent Manufacturing," *Engineering*, vol. 4, no. 1, pp. 11–20, 2018, doi: 10.1016/j.eng.2018.01.002.
- [12] A. K. Ghani, I. A. Choudhury, and Husni, "Study of tool life, surface roughness and vibration in machining nodular cast iron with ceramic tool," *J. Mater. Process. Technol.*, vol. 127, no. 1, pp. 17–22, 2002, doi: 10.1016/S0924-0136(02)00092-4.
- [13] J. A. Ghani, M. Rizal, A. Sayuti, M. Z. Nuawi, M. N. Ab Rahman, and C. H. C. Haron, "New regression model and I-kaz method for online cutting tool wear monitoring," *World Acad. Sci. Eng. Technol.*, vol. 36, no. 2008, pp. 420–425, 2009.
- [14] C. Scheffer, H. Kratz, P. S. Heyns, and F. Klocke, "Development of a tool wear-monitoring system for hard turning," *Int. J. Mach. Tools Manuf.*, vol. 43, no. 10, pp. 973–985, 2003, doi: 10.1016/S0890-6955(03)00110-X.
- [15] G. H. Lim, "Tool-wear monitoring in machine turning," *J. Mater. Process. Tech.*, vol. 51, no. 1–4, pp. 25–36, 1995, doi: 10.1016/0924-0136(94)01354-4.
- [16] L. Metalworking and T. Group, "Turning Tools & Inserts".

Performance of TEC Cascade on Input Voltage Variations in Fish Cooler Box

Sabiqunassabiqun^a, Zuryati Djafar^{b,*}, Wahyu Haryadi Piarah^c

^aDepartment of Mechanical Engineering, Univeristas Hasanuddin. Email: sabiqunassabiqun11@mail.com

^bDepartment of Mechanical Engineering, Universitas Hasanuddin. Email : zuryatidjafar@unhas.ac.id

^cDepartment of Mechanical Engineering, Universitas Hasanuddin. Email : wahyupiarah@unhas.ac.id

Abstract

The refrigeration system used to meet the needs of human life can be in the form of a thermoelectric cooler (TEC). Due to its small volume, environmental friendliness and several other advantages, TEC can be widely applied such as in fish cooler box. In this study, the cooler boxes used had dimensions of 290mmx 205mm x 254 mm and were given twelve stacked 3 TEC modules with varied DC voltages. The purpose of this study is to determine the voltage that can provide the best TEC performance. This performance will be indicated by the Coefficient of Performance (COP) value of each voltage variation. The experimental results show that the best performance of the TEC is at 42 Volts. The lowest temperature achieved during the experiment was 7.74°C on the cold-side.

Keywords: Coefficient of performance; cool box; thermoelectric cooler

1. Introduction

Fish is the most perishable food source. The presence of microorganisms causes the speed of the decomposition process in fish so it needs to be preserved, and the cooling system is one method of preserving fish [1]. Cooling machines are currently being used more and more by humans to meet the needs of life [2]. Cooling systems are used to reduce heat both in manufacturing processes [3], energy conversion, environment [4], and food processing [5]. Various types of cooling systems that are currently commonly used are air-based cooling systems; and liquid-based cooling systems; Phase Change Material (PCM) based cooling systems [6] and thermoelectric based cooling systems [7].

Thermoelectric cooler (TEC) is a module that can be used for cooling systems. TEC can convert electrical energy into temperature differences directly by using the Peltier effect [8-11]. TEC consists of two different types of semiconductors, namely P and N type semiconductors which are connected via electrodes [12] as shown in Fig. 1. Cooling TEC is an environmentally friendly cooling that can be used as a heat pump in solid form to increase the cooling energy generated. TEC cooling can be directly used using direct current (DC) electricity without using refrigerants and does not cause harmful effects to the environment [13-15].

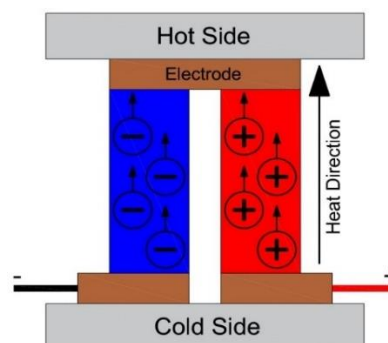


Figure 1. Sketch of General thermoelectric consisting of two ceramic substrates that serve as the foundation and electrical insulation for an n-type (left) and p-type (right) semiconductor element

In the TEC module, electrons in the n-type semiconductor and holes in the p-type semiconductor both move away from the cold-side to the hot-side when external DC power is applied [16]. The movement of electrons and holes in the two semiconductors then carries heat from the cold to the hot sides of the TEC [17].

TEC can be widely applied because it has many advantages, including small volume, does not cause noise, is environmentally friendly, and does not have mechanically moving components [8, 18]. Apart from these many advantages, the low performance coefficient of TEC is a technical obstacle that can limit its widespread application [19]. The TEC installation can be configured in a stack that forms a multi-stage thermoelectric module as shown in Fig. 2 [17].

*Corresponding author. Tel.: +62-812-8047-7465
Jl. Poros Malino Bonto Marannu, Gowa, South Sulawesi
Indonesia, 92171

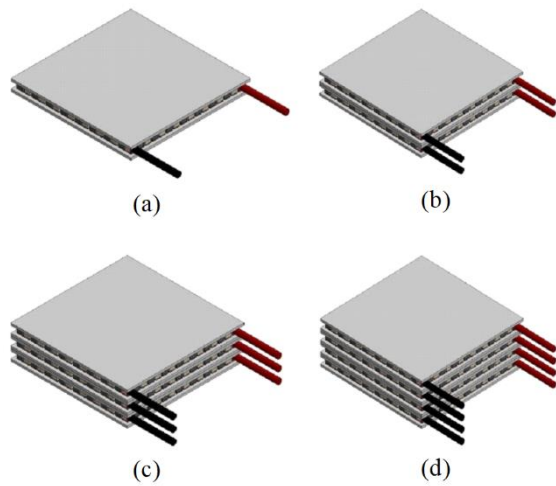


Figure 2. The thermoelectric cooler modules with the configuration of (a) single-module; (b) double modules cascade ; (c) triple modules Cascade ; (d) quadruple-modules cascade

As a result of the development of manufacturing technology and high quality raw materials, commercial TEC modules have a long service life of around 100,000 hours [20]. However, in its application, it is possible for the TEC to damage more quickly. This is indicated by a decrease in the cooling capacity of the TEC or ΔT_{max} which is below the specified criteria, and an increase in the TEC electrical resistance, usually the range of increasing the TEC electrical resistance is 5% or more [20]. TEC1-12706 is a standard size TEC which has 127 arrangements of n-type and p-type semiconductors with a maximum current that can be consumed of 6 Amperes where this type of TEC will be used in this experiment [20].

In a comprehensive review of thermoelectric cooling parameters and performance for specific refrigeration systems, Thiangchanta et al. [21] conducted experiments using a thermoelectric with a vacuum wall and can lower the temperature by about 15°C. Haryanti and Yulianti [2] made a prototype cooling system using two TECs installed in parallel and capable of lowering the temperature of a certain room to 22°C. The experimental results of He et al. [22] where experiments were carried out using a thermoelectric which is known to have a cold-side close to 15°C. Mirmanto et al. [23] concluded that the position of placing the TEC position on the box can affect the cooling process of the cooler box.

The lowest temperature achieved from previous studies is in the range of 15°C. For this reason, this latest research intends to improve the performance of the TEC which will be used in cooler boxes by attaching three modules arranged in a cascade. The performance that will be measured is the COP of the experimental set up.

2. Research Method

2.1. Installation of experimental tools

Figure 3 shows the details of installing the thermoelectric device in the cooler box. Experimental equipment includes an aluminum box covered with

styrofoam (290 x 205 x 254 mm), twelve TEC modules used in this experiment, heatsinks, fans, power supply units, and temperature data acquisition as well as a multimeter to measure voltage, current, and resistance. All contacts between the aluminum box, thermoelectric cooler, and heatsink are arranged as well as possible so that they have minimum thermal resistance using thermal paste.

The cooler box material is made of aluminum with a thickness of 1 mm and wrapped with a styrofoam thermal insulator with a thickness of 20 mm. Twelve TECs with type TEC1-12706 are used as cooling devices with a size of 40 mm x 40 mm x 3.8 mm. The working voltage of the TEC varies from 38 volts, 42 volts and 46 volts with a total electrical resistance of 40.2 Ω TEC. A multimeter is used to measure the power supplied to each Thermoelectric module. A heatsink is attached to the hot-side of the thermoelectric module to help disperse heat to the environment. Meanwhile, the cold-side of the thermoelectric module is mounted on the wall of the aluminum box. DC fans are used to circulate air through the heatsink to help distribute heat to the ambient air.

2.2. Experimental method

After DC power is supplied to the thermoelectric module, the hot-side of the thermoelectric releases heat and the cold-side of the thermoelectric absorbs heat. This happened simultaneously. The cold-side that is attached to the wall of the aluminum box will continue to decrease in temperature from the initial temperature. Due to conduction heat transfer, the temperature of the aluminum box will decrease resulting in a decrease in the room temperature in the aluminum box. After a certain time interval, the temperature of the thermoelectric cold-side will reach its lowest temperature and remain constant at that temperature as long as the electric voltage is still applied.

The electric voltage given to the thermoelectric module is set in three variations, namely 38, 42 and 46 volts. The thermoelectric modules are arranged in series in an electric circuit and work in series-parallel. The total thermoelectric modules used are 12 modules where 6 thermoelectric modules are placed on the left side of the cooler box, and the remaining 6 modules are placed on the right side of the cooler box.

The COP analysis of the cooler box is calculated from the heat absorbed on the cold-side of the TEC (Q_c) and all electric power consumption (P_{in}) which can be written in Eqs. (1) and (2) [16] [24].

$$COP = \frac{Q_c}{P_{in}} \tag{1}$$

$$P_{in} = Q_h - Q_c \tag{2}$$

$$Q_c = \alpha IT_c - k\Delta T - 0,5I^2R \tag{3}$$

$$Q_h = \alpha IT_h - k\Delta T + 0,5I^2R \tag{4}$$

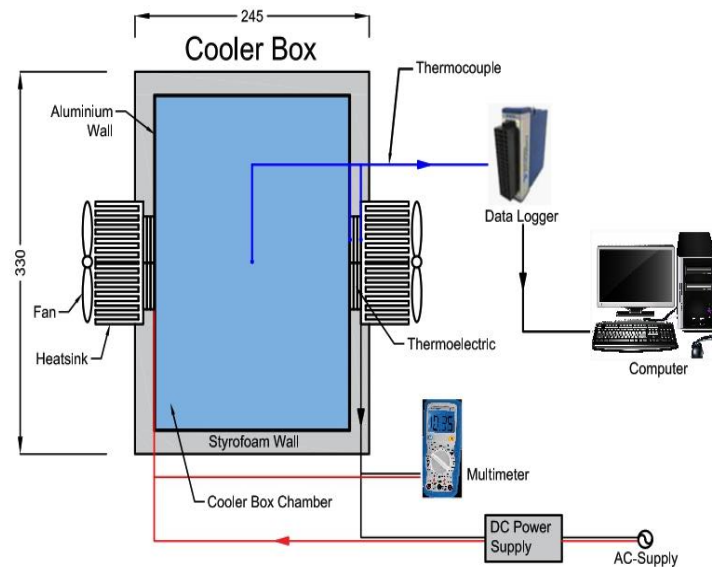


Figure 3. Experiment installation

Where α is the magnitude of the Seebeck coefficient; T_h and T_c are the hot-side and cold-side TEC temperatures; R and I respectively represent electrical resistance and working electric current; k is the thermal conductance and Q_h is the heat released by the hot-side of the TEC and is calculated using Eq. (4) [16, 24]. Q_c is the cooling capacity of the Peltier module which will be calculated using Eq. (3) [16, 24].

Previously, experiments had been carried out with the same method but differed in the arrangement and number of TECs used. For installation of a single TEC module, four TEC modules are required to be used. two modules are placed on the left side of the coolbox and the other two modules are placed on the right side of the coolbox. TECs are arranged in series in an electrical circuit and work in parallel with a given voltage of 14 Volts. The average temperatures of the TEC cold-side, hot-side TEC and coolbox are 17.45°C, 29.85°C and 18.97°C with an average COP of 0.021. In the installation with two modules of TEC arranged in a cascade, a total of eight TEC modules have been used. Four modules are placed on the left side of the coolbox and the other four modules are placed on the right side of the coolbox. TECs are arranged in series in an electrical circuit and work in series-parallel with a given voltage of 28 volts. The average temperature of the TEC cold-side, TEC hot-side and in the cooler are 14.79°C, 35.89°C and 16.82°C with an average COP of 0.048. The difference in the electric voltage obtained from the given electric voltage is the total voltage supplied for each TEC of 3.5 Volts. So that by increasing the number of TECs used, the electric voltage supplied also increases to meet the needs of each TEC of 3.5 Volts.

3. Results and Discussion

3.1. Cold-side and hot-side temperatures

Figure 4 shows the temperature changes on the cold and hot-sides of the TEC during operation. The operating time lasts 480 minutes. The cold-side temperature is the

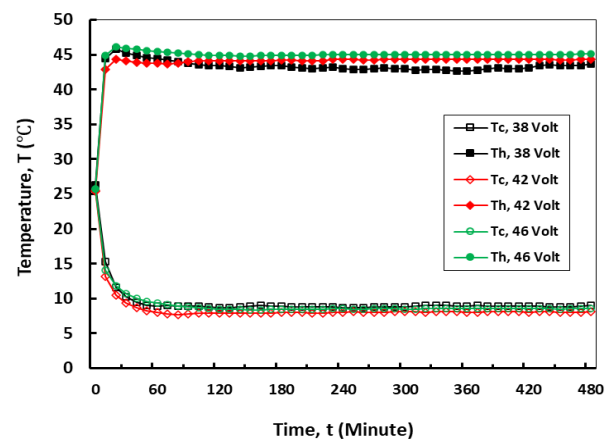


Figure 4. History of T_c and T_h of TEC modules

temperature of one side of the TEC module which absorbs heat because the heat on that side is pumped to the other side of the TEC module when electricity is applied so the temperature is lower. This cold-side then absorbs heat in the coolbox so that the coolbox temperature decreases. The temperature of the hot-side is the temperature of one side of the TEC which releases heat because this side receives heat pumped from the cold-side so that the temperature is higher.

Experimental data shows that the voltage variation of 42 Volts has a lower TEC cold-side temperature compared to the voltage variations of 38 Volts and 46 Volts. However, within the first 80 minutes of system operation, the cold-side temperature of the TEC at a working voltage of 38 volts was lower than the cold-side temperature at a working voltage of 46 volts. The lowest temperature on the cold-side occurs at 42 volts, which is 7.74°C. The temperature difference on the cold-side of the TEC when a voltage of 42 volts is applied at the 480th minute is 0.85 °C for a variation of 38 volts, and 0.45 °C for a variation of 46 volts.

The supply of 46 volts produces a hot-side temperature that is higher than the supply of 42 volts and 38 volts. The average temperature difference from 46 volts to 42 volts

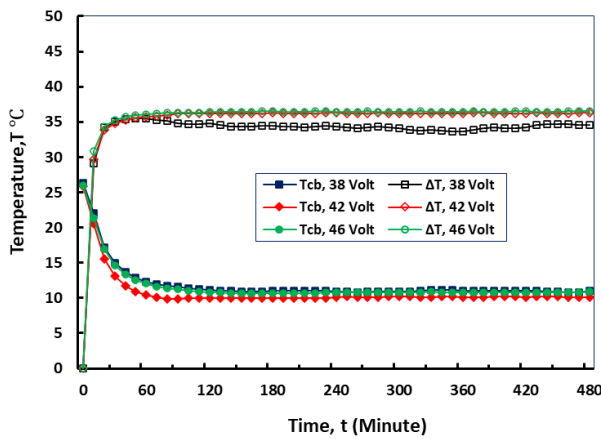


Figure 5. History of Tcb and ΔT of TEC modules

and 38 volts is 0.73°C and 1.63°C respectively. The temperature of the hot-side at 480 minutes for each given working voltage is 43.62°C at 38 volts, 44.35°C at 42 volts, and 45.12°C at 46 volts. Thus, as the greater the applied voltage, starting from 38 volts, 44 volts and 46 volts, it will produce a greater temperature difference even though there is a decrease in temperature on the cold-side. This is due to the consistent rise in temperature on the hot-side as the applied voltage increases.

3.2. Coolbox temperature and ΔT

Figure 5 shows the temperature change in the coolbox and the temperature difference between the cold-side and the hot-side of the TEC during system operation time. The supply of 42 volts produces a lower coolbox temperature than the supply of 38 volts and 46 volts. The average temperature difference from 42 volts to 38 volts and 46 volts is 1.05°C and 0.82°C respectively.

The lowest temperature achieved by the coolbox was 9.89°C which was achieved in the 80th minute when the TEC module was supplied with an electric voltage of 42 volts. After that, the temperature in the coolbox increased again and fluctuated slightly with a temperature change range of $\pm 0.3^{\circ}\text{C}$. The fluctuation range is not that large so that the coolbox temperature at 80 to 480 minutes can be stated to be in a fairly stable condition.

The temperature difference at 46 volts gives a higher value when compared to the temperature difference at 42 volts and 38 volts. The average temperature difference at 46, 42, and 38 volts is 35.50°C ; 35.23°C ; and 33.60°C . Each additional applied voltage produces a higher temperature difference. This happens because of the Seebeck effect where the voltage is directly proportional to the difference in temperature difference. This means that if the electric voltage increases, so does the difference in temperature difference and vice versa.

3.3. Heat absorbed on the cold-side (Q_c)

Figure 6 shows the ability of the cold-side of the TEC module to absorb heat during system operating time. Data on the ability of the cold-side of the TEC module to absorb heat is obtained from the calculation results based on Eq. (4). Figure 6 also shows that by providing 46 volts of electricity, the power to absorb heat on the cold-side of the TEC module is higher than that of 42 volts and 38 volts.

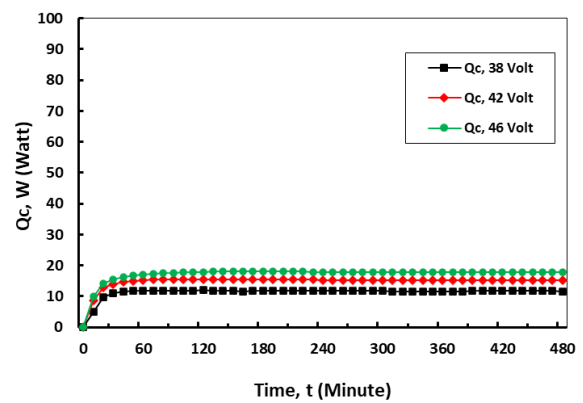


Figure 6. History of Q_c on the cold-side of TEC modules

Even so, the temperature of the cold-side of the TEC module at 42 volts is lower than at 46 volts as shown in Fig. 4. This happens because of the ability of the cold-side of the TEC module to absorb heat (Q_c) is affected by the electricity current that passes through the TEC module. For input voltage 38 volts, the electric current is 0.9 amperes. Meanwhile, for input voltage of 42 volts and 46 volts, the electric current are 0.99 amperes and 1.08 amperes. Thus, the highest value of the ability of the cold-side of the TEC module to absorb heat is achieved by varying the voltage of 46 volts.

3.4. Heat released on the hot-side (Q_h)

Figure 7 shows the value of heat released on the hot-side of the TEC module during system operating time. Data on the value of heat released on the hot-side of the TEC module is obtained from the calculation results based on Eq. (3). It can be seen in Fig. 7, that when the supply voltage is 46 volts, the hot-side of the TEC module releases more heat to the environment compared to the supply of 42 volts and 38 volts. This happens because the temperature of the hot-side of the TEC module at a voltage of 46 volts is higher when compared to the temperature of the hot-side of the TEC module when input voltage of 42 volts and 32 volts are applied as shown in Fig. 4. In addition, this is also affected by the electric current flowing passes through the TEC module when mains voltage is applied. At a voltage of 38 volts, the electric current is 0.9 amperes, while at a voltage of 42 volts and 46 volts, the electric current are 0.99 amperes and 1.08 amperes respectively. So that the greater the voltage supplied, the greater the heat value released by the hot-side of the TEC module to the environment.

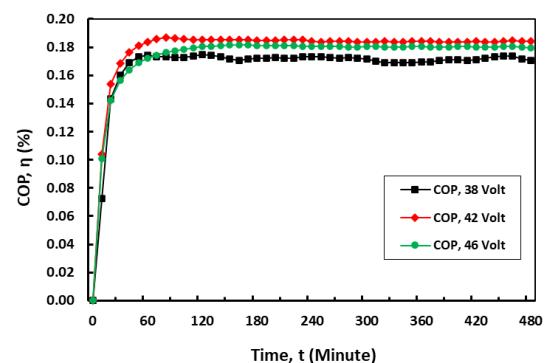


Figure 7. History of Q_h on the cold-side of TEC modules

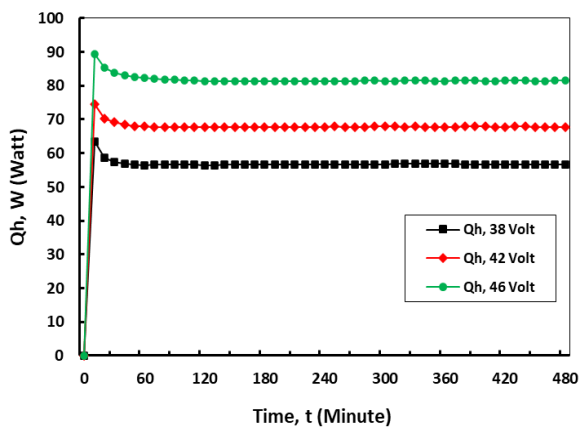


Figure 8. History of COP of TEC modules for three variation input Voltages

3.5. Coefficient of performance (COP)

The COP of the TEC module based on the given electric voltage is shown in Fig. 8. This COP is one of the parameters to measure the performance of the TEC module in cooling. The higher the COP value indicates the better the performance of the TEC modules. This is influenced by the cold-side temperature or ΔT generated by the TEC module when an electric voltage is applied. The lower the cold-side temperature or the greater the ΔT obtained by the TEC module, the higher the COP value.

In Fig. 8, it is shown that the best performance of the TEC module is given by a variation of the electric voltage of 42 Volts during the operating time of the system, amounting to 0.187. This occurs due to the low temperature of the cold-side of the TEC module at an input voltage of 42 Volts as shown in Fig. 4.

For an input voltage of 38 volts, the performance of the TEC module is not that good and fluctuations occur. The low COP value indicates the lack of ability of the cold-side of the TEC module to absorb heat and the low temperature difference between the cold-side and the hot-side of the TEC modules. While the COP value for a system with an input voltage of 46 Volts looks quite stable compared to 38 Volts. However, because the value is lower than the input voltage of 42 volts, the performance of the TEC module for an input voltage of 46 volts is no better than the performance of the input voltage of 42 volts even though the temperature difference between the hot-side and the cold-side of the resulting TEC modules is greater.

4. Conclusion

This experiment was carried out with a system operating time of 480 minutes. The system is a cooler box using a thermoelectric cooler module as the cooling medium. The thermoelectric modules are arranged in series in an electrical circuit, and work in series-parallel with a total of twelve TEC modules used. The best cooling is shown by the input voltage variation of 42 volts. At an input voltage of 42 volts it produces a lower cold-side temperature compared to other variations. However, the temperature difference that occurs between the hot-side and the cold-side of the TEC module at an input voltage of 46 volts is greater than the input voltage of 42 volts and 38

volts. The cold-side temperature and the temperature difference between the hot-side and the cold-side of the TEC module are two parameters that significantly influence the COP where the value indicates better TEC module performance. From the results of data processing, it was found that the COP value at the input voltage of 42 volts is 0.187, higher than the input voltage of 46 volts and 38 volts.

References

- [1] G. M. Hall, *Fish Processing Technology (1997, Springer US)*, 2nd ed. Blackie Academic and Professional, 1997.
- [2] M. Haryanti and B. Yulianti, "Cooling System Design Based on Thermoelectric Using Fan Motor on-off Control," *Proc. - 2018 5th Int. Conf. Inf. Technol. Comput. Electr. Eng. ICITACEE 2018*, pp. 15–18, 2018, doi: 10.1109/ICITACEE.2018.8576958.
- [3] S. Deshpande and Y. Deshpande, "A review on cooling systems used in machining processes," *Mater. Today Proc.*, vol. 18, pp. 5019–5031, 2019, doi: 10.1016/j.matpr.2019.07.496.
- [4] R. Nikbakhti, X. Wang, A. K. Hussein, and A. Iranmanesh, "Absorption cooling systems – Review of various techniques for energy performance enhancement," *Alexandria Eng. J.*, vol. 59, no. 2, pp. 707–738, 2020, doi: 10.1016/j.aej.2020.01.036.
- [5] C. James, G. Purnell, and S. J. James, "A Review of Novel and Innovative Food Freezing Technologies," *Food Bioprocess Technol.*, vol. 8, no. 8, pp. 1616–1634, 2015, doi: 10.1007/s11947-015-1542-8.
- [6] H. Sainthiya and N. S. Beniwal, "Different types of cooling systems used in photovoltaic module solar system: A review," *Proc. 2017 Int. Conf. Wirel. Commun. Signal Process. Networking, WiSPNET 2017*, vol. 2018-January, pp. 1500–1506, 2018, doi: 10.1109/WiSPNET.2017.8300012.
- [7] M. A. Rahman, A. Widyatama, A. I. Majid, and S. Suhanan, "Peltier thermoelectric refrigeration system as the future cold storage system for indonesia: A review," *Proc. - 2019 5th Int. Conf. Sci. Technol. ICST 2019*, pp. 0–5, 2019, doi: 10.1109/ICST47872.2019.9166392.
- [8] Y. Huang, Z. Chen, and H. Ding, "Performance optimization of a two-stage parallel thermoelectric cooler with inhomogeneous electrical conductivity," *Appl. Therm. Eng.*, vol. 192, December 2020, pp. 116696, 2021, doi: 10.1016/j.applthermaleng.2021.116696.
- [9] R. Ranjan, M. R. Pearson, and S. Krishnamurthy, "Thermoelectric package design for high ambient temperature electronics cooling," *Proc. 15th Intersoc. Conf. Therm. Thermomechanical Phenom. Electron. Syst. ITherm 2016*, pp. 857–861, 2016, doi: 10.1109/ITHERM.2016.7517636.
- [10] M. Ibañez-Puy, J. Bermejo-Busto, C. Martín-Gómez, M. Vidaurre-Arbizu, and J. A. Sacristán-Fernández, "Thermoelectric cooling heating unit performance under real conditions," *Appl. Energy*, vol. 200, pp. 303–314, 2017, doi: 10.1016/j.apenergy.2017.05.020.
- [11] Z. Djafar, N. Putra, and R. A. Koestoer, "The utilization of heat pipe on cold surface of thermoelectric with low-temperature waste heat," *Appl. Mech. Mater.*, vol. 302, no. February, pp. 410–415, 2013, doi: 10.4028/www.scientific.net/AMM.302.410.
- [12] S. Gonzalez-Hernandez, "Unification of optimization criteria and energetic analysis of a thermoelectric cooler and heater," *Phys. A Stat. Mech. its Appl.*, vol. 555, pp. 124700, 2020, doi: 10.1016/j.physa.2020.124700.

- [13] X. Su, L. Zhang, Z. Liu, Y. Luo, D. Chen, and W. Li, "Performance evaluation of a novel building envelope integrated with thermoelectric cooler and radiative sky cooler," *Renew. Energy*, vol. 171, pp. 1061–1078, 2021, doi: 10.1016/j.renene.2021.02.164.
- [14] A. Das, T. R. Kumar, S. Gourishankar, D. S. Pillai, T. S. Babu, and N. Rajasekar, "A novel method for modeling of thermoelectric coolers," *2017 7th Int. Conf. Power Syst. ICPS 2017*, pp. 242–246, 2018, doi: 10.1109/ICPES.2017.8387300.
- [15] U. Sanver, E. Yavuz, and C. Eyupoglu, "An electronic control unit for thermoelectric cooling," *Proc. 2019 IEEE Conf. Russ. Young Res. Electr. Electron. Eng. ElConRus 2019*, pp. 141–145, 2019, doi: 10.1109/ElConRus.2019.8656871.
- [16] Z. Djafar, Amrullah, W.H. Piarah, and S. Himran, "Experimental Test of Thermoelectric Performance on the Dispenser Cooler," *International Journal of Smart Material and Mechatronics* vol. 1, No. 1, pp.102–106., 2014.
- [17] Enrique Maciá-Barber, *Thermoelectric materials*, vol. 1. Taylor & Francis Group, LLC, 2015.
- [18] L. Shen *et al.*, "Performance enhancement investigation of thermoelectric cooler with segmented configuration," *Appl. Therm. Eng.*, vol. 168, December 2019, pp. 114852, 2020, doi: 10.1016/j.applthermaleng.2019.114852.
- [19] G. Xu, Y. Duan, X. Chen, T. Ming, and X. Huang, "Effects of thermal and electrical contact resistances on the performance of a multi-couple thermoelectric cooler with non-ideal heat dissipation," *Appl. Therm. Eng.*, vol. 169, no. June 2019, pp. 114933, 2020, doi: 10.1016/j.applthermaleng.2020.114933.
- [20] G. Gromov, "Thermoelectric Cooling Modules," *Am. J. Phys.*, vol. 30, no. 9, pp. vii–vii, 2010, doi: 10.1119/1.1942168.
- [21] S. Thiangchanta, T. Anh, W. Tachajapong, and Y. Mona, "ScienceDirect Experimental investigation of the thermoelectric cooling with vacuum wall system," *Energy Reports*, vol. 6, pp. 1244–1248, 2020, doi: 10.1016/j.egy.2020.11.048.
- [22] R. R. He, H. Y. Zhong, Y. Cai, D. Liu, and F. Y. Zhao, "Theoretical and Experimental Investigations of Thermoelectric Refrigeration Box Used for Medical Service," *Procedia Eng.*, vol. 205, pp. 1215–1222, 2017, doi: 10.1016/j.proeng.2017.10.356.
- [23] M. Mirmanto, S. Syahrul, and Y. Wirdan, "Experimental performances of a thermoelectric cooler box with thermoelectric position variations," *Eng. Sci. Technol. an Int. J.*, vol. 22, no. 1, pp. 177–184, 2019, doi: 10.1016/j.jestch.2018.09.006.
- [24] H. A. Aziz, R. I. Mainil, and A. Aziz, "A Portable Cooling And Heating Equipment Using A Thermoelectric Module With An Input Voltage Of 6 Volts With Additional Heat Pipes As Heat Transfer Media," *Jom FTEKNIK*, vol. 4, no. 2, pp. 1–5, 2017, [in Bahasa].

Classification Freshness of Red Snapper (*Lutjanus Campechanus*) Based on Eye Image Using Convolutional Neural Network

Muh Subhan^{a,*}, Nursakinah^b

^aInformatic Management Studi Program, Politeknik Negeri Fakfak, 98011, Papua Barat, Indonesia. Email: subhan@polinef.id

^bInformatic Management Studi Program, Politeknik Negeri Fakfak, 98011, Papua Barat, Indonesia. Email: nursakinah@polinef.ac.id

Abstract

Indonesia is a maritime country where fish is the most widely extracted and consumed marine natural resource, one of which is snapper. Snapper contains high protein. Therefore, it is suitable for health. Red snapper or *Lutjanus campechanus* is one economical fish with a broad market share. Red snapper is a demersal fish group that ranks third with the most exported commodities after tuna and shrimp. In addition, snapper is one of the most common consumption fish in Indonesia. Therefore, the community needs to be able to identify the freshness of the fish. Fish freshness detection is done manually by touching the fish's body, eyes, and gills. However, this can cause accidental damage to the fish parts, which will be very detrimental. Several studies on identifying fish freshness explain that the VGGNet-16 Architecture on the Convolutional Neural Network algorithm is superior in its modeling performance. This research uses a different fish object, a red snapper object, with two different architectures from several previous studies, namely the Le-Net15 and VGGNet-16 architecture. This research focuses on the eye image carried out through the pre-processing data stage by cutting the fish body, followed by augmentation to reproduce the image data without losing its essence before training the dataset. The model will be trained using the Adam optimization method with very fresh and not fresh predictions. The experimental results of the classification of two classes of red snapper freshness using 600 fish images show that VGGNet-16 achieves the best performance compared to the LeNet-5 architecture, where the classification accuracy reaches 98.40%.

Keywords: Red Snapper; CNN; neural network; deep learning; VGGNet-16

1. Introduction

Indonesia is a maritime country where the marine natural resources most often taken and consumed are fish, one of which is red snapper. Red snapper, or *Lutjanus campechanus*, is a demersal fish that can live in shallow to deep seas. According to the Central Statistics Agency (BPS), national *Lutjanus campechanus* production was recorded at 1.95 thousand tons in 2021. *Lutjanus campechanus* is an economically important type of fish that belongs to the demersal fish group and ranks third in terms of the largest export commodity after tuna and shrimp. In addition, *Lutjanus campechanus* is one of the most common consumption fish found in Indonesia, so the public needs to be able to identify the freshness of the fish.

The quality of fresh fish is characterized by clear eyes, clear corneas, black pupils, convex eyes, and fresh red gills. If the quality decreases, the gills are gray, slimy, and smelly; the scales are strongly attached, shiny, and covered with clear mucus. The smell is typical of fish [1]. The level of freshness of fish is generally identified

manually using eye observation, so it is challenging for the community to distinguish the fish's freshness level. In addition, the freshness of the fish can be identified by touching the fish's body, eyes, and gills, but this can cause accidental damage to the fish, which will be very detrimental.

Many studies on the classification of fish freshness have been carried out, one of which uses non-destructive image processing techniques using fish skin as a focused network. The skin tissue was segmented using the saturation channel of the HSV color space model. Feature statistics were extracted in the HSV color space that provided the fish freshness degradation pattern, which was used to design a framework for fish freshness identification. The result of the maximum classification accuracy of this method is 96.66% [2]. Identification of the freshness of the gill fish tissue is also carried out with an automatic image processing approach by performing. Features have been extracted from the automatically segmented gill focal tissues using Wavelet Transform. The gill tissue of fresh fish is reddish brown. The changing color of the fish tissue indicates fish damage. In the proposed methodology, the gill focus network is taken by region of interest (ROI), the image segment that carries the

*Corresponding author. Tel.: +62-823-112-66360

Imam Bonjol Atas Street
Fakfak-West Papua
Indonesia, 98612

complete information about feature extraction. From the input RGB fish image, the gills are segmented as ROI because they have complete information because of their reddish-brown color. A Non-Destructive Technique evaluates material properties without causing damage. These discriminatory features from the experiment establish a relationship between the statistical wavelet coefficients and the freshness of stored fish [3]. In addition, the classification of fish freshness using several fish samples, namely Giant Gourami, Red Snapper Fish, and Nile Tilapia, was carried out using digital images with the K-Nearest Neighbor approach producing an average accuracy of 91.36% [4].

In addition, research using the Convolutional Neural Network (CNN) algorithm approach is currently a widely developed research topic, including identifying or classifying fish freshness. Research related to the classification of the freshness level of milkfish was carried out by comparing several architectures, namely Xception, MobileNet V1, Resnet50, and VGG16. The experimental results of the classification of two classes of milkfish freshness using 154 images show that VGG16 achieves the best performance compared to other architectures, where the classification accuracy reaches 97% [5]. The study used a Deep Convolution Neural Network (DCNN) approach to detect the freshness of sardine samples and classify fish samples as fresh fish or rotten fish. The automatic detection system was implemented, evaluated, and obtained results of 99.5% accuracy, 96.2% sensitivity, 92.3% specificity, 92.6% PPV, 96% NPV, and 94% f1-score. Using several stages, including pre-processing data, namely Image Rescaling Color Transformation, then the distribution of testing data and training data, then classification using the Deep CNN approach [6]. Another study that implemented fish freshness detection using a convolutional neural network (CNN) approach was carried out to detect goldfish freshness. A VGG-16 architecture was applied to extract features from FSH images automatically. Then, the developed classifier block is constructed by dropout, and a solid layer is used to classify the FSH image. The results indicate a classification accuracy of 98.21%, and the conclusion is that the CNN-based proposal has lower complexity with higher accuracy than traditional classification methods [7]. In another study on freshness detection using fish samples, Nile Tilapia employs an automated method for classifying fish freshness based on a combined deep learning model and image processing. The process extracts features using VGG-16 neural network architecture, and bi-directional long-short-term memory is used to build a machine learning model. The proposed model has achieved 98% accuracy in testing [8].

This study aims to develop software to read and analyze fish images and then automatically predict whether the image is fresh fish or not fresh fish, using two different architectures from previous studies, namely the LeNet-5 and VGGNet-16 architectures. This experiment uses the red snapper object, which consists of image acquisition, pre-processing image, augmentation, and utilizing the holdout method.

2. Material and Method

2.1. System design

Figure 1 shows this study's system design, which consists of Image Acquisition, Pre-processing data, Augmentation classification using Convolutional Neural Network Algorithm Performance analysis method of classification, and Algorithm Performance Result. Implementation of fish freshness classification uses Python programming language to create models and is assisted by the Tensorflow library, which is one of the most famous Python libraries for creating Deep Learning models.

2.2. Image acquisition

Image data of *Lutjanus campechanus* was obtained from the Dulan Pokpok Fisheries Port, Jl. Yos Sudarso, Dulan Pok-Pok Village, Wagom Village, Kec. Fak-Fak, Fak-Fak Regency. The image of the fish is taken from various angles using the camera Hp Iphone 7+ Dual 12 MegaPixel full HD camera specifications with a screen resolution of 1920 x 1080 pixels. A sample of fish image data was taken during April–August 2021. The data obtained were 300 images of very fresh fish and 150 images of Not Fresh Fish. A sample of image data for fresh *Lutjanus campechanus* can be seen in Fig. 2, while the sample data for *Lutjanus campechanus* that is not fresh can be seen in Fig. 3.

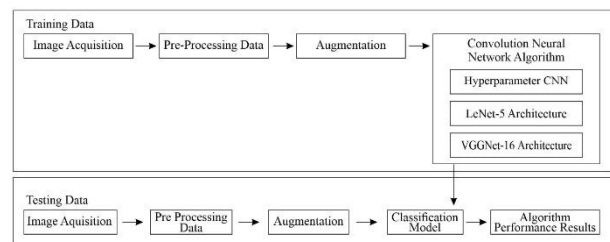


Figure 1. System design



Figure 2. Fresh fish of *Lutjanus campechanus*



Figure 3. Not fresh fish of *Lutjanus campechanus*

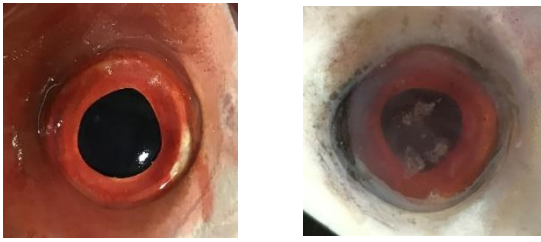


Figure 4. Eyes of fresh fish and not fresh fish

2.3. Pre-processing image

Pre-processing an image is a step to get input data of a *Lutjanus campechanus* image for the classification process by cutting the image. The process is done after getting some *Lutjanus campechanus* image data at the acquisition stage, then doing the cutting process to remove unnecessary objects, namely the fish's body. The research focuses on the red snapper eye object. The image-cutting process gives different image resolution results. Sample image data of a *Lutjanus campechanus* that has been pre-processed image can be seen in Fig. 4

2.4. Augmentation

Data augmentation is the process of reproducing an image without losing its essence [9]. Artificially augmentation is a technique to create new training data from existing training data. Data augmentation aims to expand the training data set to improve CNN performance and prevent over-fitting problems [10]. Augmentation is carried out only on not fresh fish data because the data obtained is less than fresh fish data, so the available data is not balanced. In the data augmentation process, traditional transformations are used, namely reflection and color transformation. These techniques are some of the most popular augmentation techniques because the method is easy to understand and has proven to be fast, reproducible, and reliable. Besides that, the implementation code is relatively easy and available for download with most deep learning frameworks [11]. Augmentation implementation is carried out using the Keras Library deep learning through the Image Data Generator class. Three techniques are used in this study, namely random brightness, one type of augmentation; Color transformation produces 50 new data types; horizontal flip and vertical flip, which is a type of reflection in the traditional transformation technique, each producing 50 new data. Image data non-fresh red snapper was 150 fish. After augmentation, the data obtained was 300 non-fresh red snapper image data, so the training data is 300 fresh *Lutjanus campechanus* and 300 Not fresh *Lutjanus campechanus*.

2.5. Augmentation architectures of Convolution Neural Network (CNN)

CNN is a supervised deep-learning tool. This algorithm is acceptable for multi-class classification and binary classification. CNN is often used to solve various pattern and image recognition problems. Deep learning approaches are effective and suitable for visuals [12]. The

CNN model is a combination of the following types: convolutional layers, pooling layers, fully connected layers, and fully connected layers that extract features from the input, minimize the size for computational performance and classify an image respectively [10]. This study uses CNN architecture. There are LeNet-5 and VGG-16.

The two architectures used are described below:

1. Hyperparameter CNN

Hyperparameter is a variable that determines how a model is trained. In this experiment, the researcher also set the CNN hyperparameter, as presented in Table 1 We made adjustments to hyperparameters during the experiment as follows: The number of neurons in the fully connected layer is 1024, the dropout is 0.1, the optimizer is ADAM, the learning rate is 1e-5, the loss function is binary cross-entropy, the epoch is 100 times, and the batch size is set to 35.

2. LeNet-5 Architecture

Neural Network Architecture was designed by Yann Lecun, Leon Bottou, Yosuha Bengio, and Patrick Haffner for handwriting and printing machine character recognition in 1998 called Lenet-5 [13]. LeNet-5 has eight layers, which are five convolution layers and three fully connected layers. Each unit has 25 inputs. The unit in the first hidden layer receives input from the 5×5 area. The input image is passed to the first hidden layer. This local area of the input image is called the unit receptive field. The unit's output is stored in the same location on the feature map. Various feature maps are generated from different weight vectors applied to the same input image. The features can be extracted from the obtained feature map. Sub-sampling has been described in the second layer. The number of map features obtained after sub-sampling is the same as that obtained after convolution. Here in the 2×2 sub-sampling layer, the area is taken as input and calculated as the average of the four inputs, multiplied by the trainable coefficient and adding trainable bias, giving it to the sigmoid function. An increase in the number of feature maps can be observed as the spatial resolution decreases layer by layer. Learning is carried out using the backpropagation method [14].

Table 2 shows the CNN LeNet-5 Architecture Network Layer used to implement fish freshness classification. There is a difference from the architecture in the output layer with a size of 2 classes because the output classification in this study only uses two classes, namely, Fresh Fish and Not fresh Fish.

Table 1. Hyperparameter CNN

No.	Hyperparameter	Value
1	Neurons in the hidden, fully connected layer	1024
2	Dropout	0.1
3	Optimizer	ADAM
4	Learning rate	1.00E-05
5	Loss function	Binary cross entropy
6	Epoch	100
7	Batch size	35
8	LR 2	0.0005

Table 2. Network layer architecture CNN LeNet-5

Layer	Layer Type	Feature Maps	Kernel Size	Size	Activation Function
Input	Image		-	32x32	
C1	Convolution	6	5x5	28x28	Tanh
S2	Sub Sampling	6	5x5	14x14	Sigmoid
C3	Convolution	16	5x5	10x10	Tanh
S4	Sub Sampling	16	5x5	5x5	Sigmoid
C5	Convolution	120	5x5	1x1	Tanh
F6	Fully Connected	-	5x5	84	Sigmoid
Output	Fully Connected	-	-	2	Softmax

Table 3. Network layer architecture CNN modified VGGNet-16

Layer	Layer Type	Feature maps	Kernel size	Size	Activation Function
Input	Image	3	-	50 x 50	-
	Convolution	64	3x3	50 x 50	Relu
	Convolution	64	3x3	50 x 50	Relu
	Max Pooling	64	2x2	25 x 25	Relu
	Convolution	128	3x3	25 x 25	Relu
	Convolution	128	3x3	25 x 25	Relu
	Max Pooling	128	2x2	12 x 12	Relu
	Convolution	256	3x3	12 x 12	Relu
	Convolution	256	3x3	12 x 12	Relu
	Convolution	256	3x3	12 x 12	Relu
	Max Pooling	256	2x2	6 x 6	Relu
	Convolution	512	3x3	6 x 6	Relu
	Convolution	512	3x3	6 x 6	Relu
	Convolution	512	3x3	6 x 6	Relu
	Max Pooling	512	2x2	3 x 3	Relu
	Convolution	512	3x3	3 x 3	Relu
	Convolution	512	3x3	3 x 3	Relu
	Max Pooling	512	2x2	1 x 1	Relu
	Fully Connected	-	-	4096	Relu
	Fully Connected	-	-	4096	Relu
	Fully Connected	-	-	1000	Relu
Output	Fully Connected	-	-	2	SoftMax

3. VGGNet-16 Architecture

Convolution input layer 1 using a standard image size of 224 x 224 RGB VGGNet-16 has 16 layers, namely 13 convolution layers and three fully connected layers. VGGNet-16 uses the block concept to form a convolution layer, each of which has a size of 3 x 3 and a stride layer of 1. At the end of the block, a max pooling layer of size 2 x 2 and stride 2 of 16 is used. The first convolution input layer is modified to 50 x 50 because of the large amount of processed data, so it requires a heavy training process.

The solution is to reduce the resolution of the input image in the training and testing process. The researcher modified it using the VGGNet-16 concept and produced a convolution neural network model with a modified VGGNet-16 architecture. Table 3 shows Network layer Architecture CNN Modified VGGNet-16.

4. Validation Holdout

The validation process is fundamental to do. The goal is that every piece of data can be used as training and experimental data. There are several model validations, one of which is Holdout validation [15]. Holdout validation is a dataset distribution where the data will be divided into testing data and training data. For example, if 0.2, then 20% of the data is used for testing and the rest for training data, which is 80%.

In this study, the holdout validation method is used, the simplest method that takes the original dataset and randomly divides it into two sets: the dataset into "training" and "testing" sets. The holdout method was applied to all trials conducted using deep learning (CNN), which used 80% of the 480 data for training and the remaining 20% of the 120 data for testing.

3. Results and Discussion

3.1. LeNet-5 architecture training performance

The performance of the model in the LeNet-5 architecture training process is based on hyperparameters and the Network Layer Architecture of CNN. The results showed that the highest training data accuracy reached 95.78% in the 100th epoch, while the lowest training data accuracy resulted in the 20th epoch was 87.77%. From 20 to 100 epoch, there is a rapid change in accuracy. The results of the LeNet-5 architectural training performance can be seen in Table 4. The graphics of Train-Tess Accuracy and Train-test Loss can be seen in Fig. 5.

3.2. Training performance of the VGGNet-16 architecture

The VGGNet-16 architecture training process model is based on the parameters and the Network Layer Architecture of CNN. The results showed that the highest training data accuracy reached 98.40% in the 100th epoch, while the lowest training data accuracy in the 20th epoch was 94.10%. From epoch 20 to epoch 100, there is a rapid change in accuracy. Table 5 Show The results of the VGGNet architectural training performance, Figure 6 shows the train-tess accuracy and train-test loss.

Table 4. LeNet-5 architecture training performance

Epoch	Batch size	Learning Rate	Optimizer	Val_Loss	Val_Acc	Loss	Accuracy
20	35	0.0001	Adam	25.25%	89.17%	25.99%	87.77%
40	35	0.0001	Adam	27.76%	89.17%	17.70%	94.73%
60	35	0.0001	Adam	17.05%	95.83%	21.84%	90.80%
80	35	0.0001	Adam	15.89%	94.17%	14.57%	94.95%
100	35	0.0001	Adam	16.50%	95.83%	14.44%	95.78%

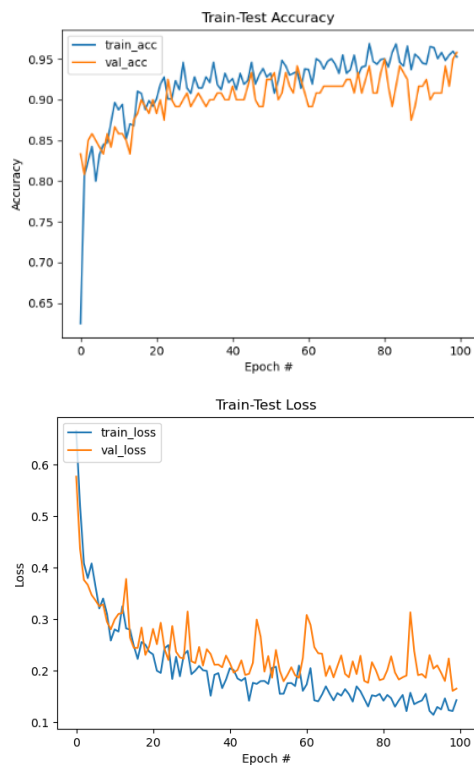


Figure 5. Graphics train-test accuracy and loss LeNet-5 Epoch 100

Table 5. VGGNet-5 architecture training

Epoch	Batch size	Learning Rate	Optimizer	Val_Loss	Val_Acc	Loss	Accur acy
20	35	0.0001	Adam	308.70%	80.00%	207.90%	94.10%
40	35	0.0001	Adam	234.75%	94.17%	206.18%	95.16%
60	35	0.0001	Adam	241.30%	92.50%	212.00%	95.70%
80	35	0.0001	Adam	202.01%	97.50%	196.43%	98.24%
100	35	0.0001	Adam	226.00%	97.00%	193.00%	98.40%

3.3. Testing performance of the LeNet-5 architecture

After training using LeNet-5 and VGGNet-16, the best model was obtained based on predetermined hyperparameters. The modeling was tested on new data

(that had not been previously trained) to determine the model's performance. The amount of tested data is 40 fish images, consisting of 20 images of fresh fish and 20 photos of not fresh fish. The test is to see how much accuracy is obtained from the model generated using LeNet-5 and VGGNet-16. The results of the LeNet-5 test of Lutjanus campechanus with a fresh label were 20, with the detection results of 14 fresh Lutjanus campechanus and six non-fresh Lutjanus campechanus. The LeNet-5 test of Lutjanus campechanus with the label not fresh amounted to 20, with the detection of not fresh 13 and 7 fresh Lutjanus campechanus. The following table shows the LeNet-5 red snapper test results, fresh and not fresh.

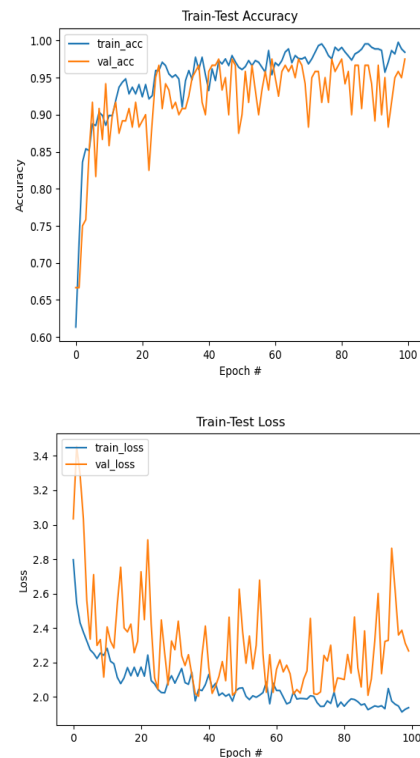


Figure 6. Train-test accuracy dan loss VGGNet-16 Epoch 100

Table 6. Testing result performance of the LeNet-5 architecture

Result testing fresh Lutjanus campechanus.				Result testing Not fresh Lutjanus campechanus.			
Image Fish	Class	classify	Probability	Image Fish	Class	classify	Probability
1 jpg	Fresh	Fresh	99.94%	21 jpg	Not Fresh	Not Fresh	100%
2 jpg	Fresh	Fresh	96.01%	22 jpg	Not Fresh	Not Fresh	100%
3 jpg	Fresh	Fresh	99.98%	23 jpg	Not Fresh	Not Fresh	65.32%
4 jpg	Fresh	Fresh	99.99%	24 jpg	Not Fresh	Not Fresh	99.95%
5 jpg	Fresh	Fresh	99.92%	25 jpg	Not Fresh	Not Fresh	99.95%
6 jpg	Fresh	Fresh	96.45%	26 jpg	Not Fresh	Not Fresh	99.93%
7 jpg	Fresh	Fresh	95.04%	27 jpg	Not Fresh	Fresh	98.55%
8 jpg	Fresh	Fresh	98.68%	28 jpg	Not Fresh	Fresh	100%
9 jpg	Fresh	Fresh	99.58%	29 jpg	Not Fresh	Fresh	99.89%
10 jpg	Fresh	Not Fresh	94.40%	30 jpg	Not Fresh	Fresh	100%
11 jpg	Fresh	Not Fresh	99.58%	31 jpg	Not Fresh	Fresh	99.58%
12 jpg	Fresh	Not Fresh	98.68%	32 jpg	Not Fresh	Not Fresh	99.70%
13 jpg	Fresh	Not Fresh	96.62%	33 jpg	Not Fresh	Not Fresh	100%
14 jpg	Fresh	Not Fresh	99.99%	34 jpg	Not Fresh	Not Fresh	99.76%
15 jpg	Fresh	Not Fresh	99.22%	35 jpg	Not Fresh	Not Fresh	97.21%
16 jpg	Fresh	Fresh	98.62%	36 jpg	Not Fresh	Not Fresh	55.78%
17 jpg	Fresh	Fresh	89.31%	37 jpg	Not Fresh	Not Fresh	100%
18 jpg	Fresh	Fresh	98.68%	38 jpg	Not Fresh	Not Fresh	99.64%
19 jpg	Fresh	Fresh	99.98%	39 jpg	Not Fresh	Fresh	100%
20 jpg	Fresh	Fresh	99.99%	40 jpg	Not Fresh	Fresh	99.98%

Table 7. Testing result performance of the VGGNet-16 architecture

Result testing Not fresh Lutjanus campechanus				Result testing Not fresh Lutjanus campechanus					
Image	Fish	Class	classify	Probability	Image	Fish	Class	classify	Probability
1	Jpg	Fresh	Fresh	100%	21	jpg	Not Fresh	Fresh	97.19%
2	Jpg	Fresh	Fresh	85.26%	22	jpg	Not Fresh	Fresh	99.84%
3	Jpg	Fresh	Fresh	100%	23	jpg	Not Fresh	Not Fresh	93.90%
4	Jpg	Fresh	Fresh	100%	24	Jpg	Not Fresh	Not Fresh	99.24%
5	Jpg	Fresh	Fresh	100%	25	Jpg	Not Fresh	Not Fresh	100%
6	Jpg	Fresh	Fresh	100%	26	Jpg	Not Fresh	Not Fresh	100%
7	Jpg	Fresh	Fresh	100%	27	Jpg	Not Fresh	Not Fresh	100%
8	Jpg	Fresh	Fresh	99.99%	28	Jpg	Not Fresh	Not Fresh	100%
9	Jpg	Fresh	Fresh	100%	29	Jpg	Not Fresh	Not Fresh	100%
10	Jpg	Fresh	Fresh	99.63%	30	Jpg	Not Fresh	Fresh	100%
11	Jpg	Fresh	Fresh	100%	31	Jpg	Not Fresh	Fresh	100%
12	Jpg	Fresh	Fresh	99.87%	32	Jpg	Not Fresh	Fresh	100%
13	Jpg	Fresh	Fresh	98.81%	33	Jpg	Not Fresh	Not Fresh	100%
14	Jpg	Fresh	Fresh	100%	34	Jpg	Not Fresh	Not Fresh	99.99%
15	Jpg	Fresh	Fresh	100%	35	Jpg	Not Fresh	Not Fresh	99.22%
16	Jpg	Fresh	Not Fresh	100%	36	Jpg	Not Fresh	Not Fresh	99.93%
17	Jpg	Fresh	Not Fresh	85.26%	37	Jpg	Not Fresh	Not Fresh	99.65%
18	Jpg	Fresh	Not Fresh	100%	38	Jpg	Not Fresh	Not Fresh	99.84%
19	Jpg	Fresh	Not Fresh	91.55%	39	Jpg	Not Fresh	Not Fresh	99.90%
20	Jpg	Fresh	Not Fresh	100%	40	Jpg	Not Fresh	Not Fresh	100%

3.4. Testing performance of the VGGNet-16 architecture

After conducting training using LeNet-5 and VGGNet-16, the best model was obtained based on predetermined parameters, and it was tested on new data to determine the model's performance. The amount of data is 40 fish images, consisting of 20 images of fresh fish and 20 images of non-fresh fish, to see how much accuracy is obtained from the model generated using LeNet-5 and VGGNet-16. The results of the VGGNet-16 test of red snapper with a fresh label were 20, with the detection results of 15 fresh Lutjanus campechanus and five not fresh Lutjanus campechanus. The LeNet-5 test of Lutjanus campechanus with the label not fresh amounted to 20, with the detection of not being fresh amounted to 15 red snappers and five fresh Lutjanus campechanus. The following table shows the results of the VGGNet-16 red snapper testing, fresh and not fresh.

3.5. LeNet-5 and VGGNet-16 model testing results using new data

The following explains the classification performance used in this study by finding the value of performance measurement:

$$Accuracy = \frac{TP+TN}{TP+TN+FN+FP} \tag{1}$$

$$Precision = \frac{TP}{TP+FP} \tag{2}$$

$$Recall = \frac{TP}{TP+FN} \tag{3}$$

$$F1 - measure = 2 \frac{Presisi*Recall}{Presisi+Recall} \tag{4}$$

Table 8 shows the prediction results of LeNet-5 and VGGNet-16. The results of the modeling test, the accuracy value obtained is the highest accuracy value of 75% Using the VGGNet-16 model. Figure 7 shows the new data image of testing data. The 40 images have not been used for training.

Table 8. Testing results using new data

Model	Accuracy	Precision	Recall	F1-Score
LeNet-5	73.00%	70.00%	66.70%	68.30%
VGGNet-16	75.00%	75.00%	75.00%	75.00%

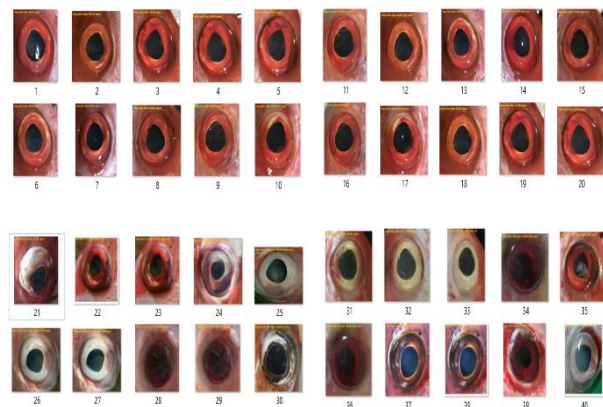


Figure 7. Image data testing

4. Conclusion

Based on the analysis of the results of the identification of the freshness level of Lutjanus campechanus using the CNN LeNet-5 and VGGNet-16 methods, researchers can conclude from the research results:

The procedure for building this classification system involves several process stages, starting from Image acquisition, cutting, and data augmentation. The first stages are carried out to obtain input data for the classification system, and then the classification process is training and testing. The results of the training comparison of the 2 LeNet-5 and VGGNet-16 architectures with the highest accuracy value on LeNet-5 reached 95.78% using epoch 100, batch size 35, learning rate 0.0001, and the VGGNet-16 architecture with an accuracy value of 98.40% using epoch 100, batch size 35, learning rate 0.0001 So, the highest accuracy value is obtained on the VGGNet-16 architecture. Test results comparison of 2

LeNet-5 and VGGNet-16 architectures with the highest accuracy value on LeNet-5 reaching 73.0%, Precision 70.0%, Recall 66.7%, F1-Score 68.3%, and the highest VGGNet-16 architecture reaching 75.0 %, Precision 75.0%, Recall 75.0%, F1-Score 75.0%. It shows that VGGNet-16 is more appropriate to be implemented in classifying fresh and unfresh red snapper freshness.

Acknowledgements

LPPPM Politeknik Negeri Fakfak funded this research. The researchers really appreciate this help. In addition, we would like to convey our gratitude to all of our direct and indirect supporters.

References

- [1] Kementerian Kelautan dan Perikanan (KKP), "Pencarian Produksi Ikan Dengan Perbandingan Tahun," 2020.
- [2] N. Sengar, V. Gupta, M. K. Dutta, and C. M. Travieso, "Image Processing Based Method For Identification Of Fish Freshness Using Skin Tissue," in *4th International Conference on Computational Intelligence & Communication Technology (CICT)*, 2018, pp. 1–4, doi: 10.1109/CICT.2018.8480265.
- [3] M. Arora, P. Mangipudi, M. K. Dutta, and R. Burget, "Image Processing Based Automatic Identification of Freshness in Fish Gill Tissues," doi: 10.1109/ICACCCN.2018.8748778.
- [4] N. M. S. Iswari, Wella, and Ranny, "Fish freshness classification method based on fish image using k-Nearest Neighbor," in *2017 4th International Conference on New Media Studies (CONMEDIA)*, 2017, pp. 87–91, doi: 10.1109/CONMEDIA.2017.8266036.
- [5] K. A. Priya, A. C. Kaladevi, and R. Perumal, "Detection of Sardine Fish Freshness Using Deep Convolution Neural Network," *Ann. Rom. Soc. Cell Biol.*, vol. 25, no. 4, pp. 16063–16070, 2021.
- [6] E. Prasetyo, R. Purbaningtyas, R. D. Adityo, E. T. Prabowo, and A. I. Ferdiansyah, "A Comparison Of Convolution Neural Network For Classifying Milkfish's Freshness On Eye Images," *J. Teknol. Inf. dan Ilmu Komput.*, vol. 8, no. 3, pp. 601–608, 2021, doi: 10.25126/jtiik.202184369.
- [7] A. Nasiri, A. Banan, Y.-D. Zhang, and A. T. Garavand, "Smart deep learning-based approach for non-destructive freshness," *J. Food Eng.*, vol. 278, no. 3, 2020.
- [8] M. A. Rayan, A. Rahim, M. A. Rahman, M. A. Marjan, and U. A. M. E. Ali, "Fish Freshness Classification Using Combined Deep Learning Model," in *2021 International Conference on Automation, Control and Mechatronics for Industry 4.0 (ACMI)*, 2021, pp. 1–5, doi: 10.1109/ACMI53878.2021.9528138.
- [9] T. Badriyah, N. Sakinah, I. Syarif, and D. R. Syarif, "Machine Learning Algorithm for Stroke Disease Classification," in *2020 International Conference on Electrical, Communication, and Computer Engineering (ICECCE)*, 2020, pp. 1–5, doi: 10.1109/ICECCE49384.2020.9179307.
- [10] M. M. A. Monshi, J. Poon, V. Chung, and F. M. Monshi, "CovidXrayNet: Optimizing data augmentation and CNN hyperparameters for improved COVID-19 detection from CXR," *Comput. Biol. Med.*, vol. 133, no. 104375, 2021.
- [11] Mikołajczyk and M. Grochowski, "Data augmentation for improving deep learning in an image classification problem," in *2018 International Interdisciplinary PhD Workshop (IIPHDW)*, 2018, pp. 117–122, doi: 10.1109/IIPHDW.2018.8388338.
- [12] D. M. Abdullah, A. M. Abdulazeez, and A. B. Sallow, "Lung cancer Prediction and Classification based on Correlation Selection method Using Machine Learning Techniques," *Qubahan Acad. J.*, vol. 1, no. 2, pp. 141–149, 2021, [Online]. Available: 10.48161/qaj.v1n2a58.
- [13] Y. LeCun, L. Bottou, Y. Bengio, and P. Haffner, "Gradient-based learning applied to document recognition," in *Proceedings of the IEEE 86 (11)*, 1998, pp. 2278–2324.
- [14] S. Indolia, A. K. Goswami, S. P. Mishra, and P. Asopa, "Conceptual Understanding of Convolutional Neural Network- A Deep Learning Approach," *Procedia Comput. Sci.*, vol. 132, pp. 679–688, 2018.
- [15] F. Tempola, R. Rosihan, and R. Adawiyah, "Holdout Validation for Comparison Classification Naïve Bayes and KNN of Recipient Kartu Indonesia Pintar," in *IOP Conference Series: Materials Science and Engineering*, 2021, vol. 1125, doi: 10.1088/1757-899X/1125/1/012041.

Semiotic Perspective of Characteristics and Meanings of Hunto Sultan Amai Mosque Ornaments in Gorontalo

Asmin Salongi^{a,*}, Afifah Harisah^b, Ria Wikantari^c

^aDepartment of Architecture, Faculty of Engineering, Universitas Hasanuddin, Makassar, Indonesia. Email: asminsalongi231@gmail.com

^bDepartment of Architecture, Faculty of Engineering, Universitas Hasanuddin, Makassar, Indonesia. Email: harisahhussein@gmail.com

^cDepartment of Architecture, Faculty of Engineering, Universitas Hasanuddin, Makassar, Indonesia. Email: rwikantaria@gmail.com

Abstract

A mosque is a well-known form of architecture in the Islamic community, serving as a center for religious activities and a symbol of Islamic identity. The Hunto Mosque in Gorontalo City, Hohuntonga, which means a gathering place, is known for its beautiful architectural design which owes much to the role of the ornaments adorning the building. This research aims to describe and interpret the characteristics and meanings of the ornaments in the Hunto Sultan Amai Mosque, as well as identify the factors that shape their characteristics. A qualitative method with Roland Barthes' (1986) semiotic approach was employed, and data was gathered through observation, interviews, and documentation. The results reveal that the ornamentation in the mosque consists of geometric and floral shapes, with square patterns and lotus flower motifs, colored in white and gold and made of paint. The most prominent placement of these ornaments is on the mosque wall elements. The square shape has meaning "symbol of physical experience and the physical world of materiality", while the lotus flower represents adaptation and idealism. White signifies purity, while gold symbolizes triumph and power. The characteristics and meanings of the ornaments are formed from Arab and Malay architecture.

Keywords: Islamic architecture; ornaments; Hunto Sultan Amai Mosque; Gorontalo; semiotics

1. Introduction

A mosque is a symbol of Islamic heritage and serves as a center for religious activities for Muslims. The importance of mosques to the Muslim community is evident in their grand, beautiful, and monumental architecture [1]. One such mosque that boasts exquisite design and historical artifacts is the Hunto Sultan Amai Mosque in Gorontalo. This mosque is called Hunto, derived from the name of the city of Gorontalo, Hohuntonga, meaning a gathering place. The mosque is named after Sultan Amai, who played a crucial role in spreading the teachings of Islam in Gorontalo and establishing the region's first mosque [2].

The Hunto Sultan Amai Mosque in Gorontalo is renowned for its beautiful architectural design. The beauty of the mosque is not only attributed to its design, but also to the ornaments that adorn the building. These ornaments are not only decorative, but they also carry significant Islamic religious values.

The ornaments in the Hunto Sultan Amai Mosque convey the forms and teachings of Islam, manifested in motifs that do not depict realistic or naturalistic living creatures. These ornaments are historic remnants of Sultan Amai that are hundreds of years old, including the

ornaments located on the pulpit and main pillars of the mosque. The presence of ornaments in the Hunto Mosque is not just for decoration, but they also hold their own meanings and significance.

To understand the meaning behind the ornaments of a building, one can explore semiotics, a field of study that analyzes signs in human life. The author specifically examines the ornaments found in the Hunto Sultan Amai Mosque in Gorontalo from a semiotic perspective, using Roland Barthes theory of signs as a framework (see Fig. 1).

The Hunto Sultan Amai Mosque in Gorontalo has now been designated as a cultural heritage site that must be preserved and maintained by the Ministry of Education and Culture's Center for the Preservation of Cultural Heritage in Gorontalo, as stated by Faiz, M. Hum, the coordinator of the documentation and publication unit of the BPCB Gorontalo during the initial research observation in 2022.

A previous study conducted by [3] on the ornaments of the An-Nur Riau Mosque only focused on the types and forms of ornaments and described their meaning in semiotics. In contrast, this current study focuses on the characteristics of the ornaments (motifs, materials, various shapes, colors, and placement positions), interpreting the meaning of the ornaments in semiotics, and discovering the factors that shape the characteristics of the ornaments in the Hunto Sultan Amai Mosque in Gorontalo.

*Corresponding author. Tel.: +6282193534803
Jalan PorosMalino km.6 Bontomarannu, Gowa
Sulawesi Selatan, Indonesia, 92171



Figure 1. Ornamentation in the main hall of Hunto Sultan Amai Gorontalo Mosque

2. Literature Review

2.1. Mosque

According to Prophet Muhammad (SAW), the mosque is the place where Muslims pray, as he said "The mosque is where you pray." In the Quran, the word "masjid" meaning as mosque, appears 20 times, which is derived from the word "sajada/sujud," meaning to show respect, obedience, and submission [4].

2.2. Ornament

Sunaryo [5] defines ornaments as the application of decoration to a work of art in his book entitled "Ornamen Nusantara". The ornaments found on mosque buildings are usually carved or affixed using materials intended for decoration. These ornaments can be manifested on walls or become part of the structural form of the mosque building, such as ornaments found on windows, doors, air vents, and ceilings.

2.3. The function of mosque ornament

Basically, the function of ornamentation is not only to fill space without meaning. According to [6], ornaments have several functions:

- (a) Purely aesthetic function, which means that ornaments are used to enhance the appearance of a decorated product and turn it into a work of art.
- (b) Symbolic function, as a decoration for an object and having a certain symbolic value in it according to certain norms (customs, religion, other social systems).
- (c) Constructive technical function, structurally meaning that ornaments can be used as support, reinforcement, connection or strengthening of construction.

2.4. Color of ornaments

The color of an ornament is the most important aspect, as it can indicate the origin of the ornament's shape. Color can also provide specific meanings and serve as an identifying characteristic. According to [7], Malay decorative patterns use various colors: (a) yellow to represent grandeur, fertility, and prosperity; (b) green as a symbol of Islam; (c) white for purity and mourning; (d) gold for triumph and power; (e) blue as a symbol of strength in the ocean; (f) black for strength; (g) red for brotherhood, courage, hope, luck, and happiness; (h) brown as a symbol of comfort, simplicity, and classic yet modern aesthetics.

2.5. Variety of architectural ornaments

Various types of decorative elements can be found across the world, many of which are celebrated for their artistic value and are associated with their country of origin. Examples include Islamic, Middle Eastern, Indian, Arab, Malay from Indonesia, Chinese, and European ornaments.

These ornaments can be classified into seven architectural styles: (a) Islamic ornamentation, which features geometric shapes such as lines, circles, squares, triangles, spirals, and crosses, as well as calligraphy in various styles such as *koufi*, *naskhi*, *tsuluts*, *farisi*, *riq'ah*, *diwani*, and *rayhani* [8]; (b) Middle Eastern architectural ornamentation shares similar characteristics with Islamic ornamentation, including calligraphic shapes, diamond and arch geometric shapes, arabesque or interlacing designs, tall towers, and majestic domes [9]; (c) Mughal Indian architectural ornamentation showcases calligraphic shapes, geometry, and shapes of living creatures, such as those found on the Taj Mahal building [10]; (d) Arab architectural ornamentation is characterized by arabesque shapes that are often interlaced with lotus/water lily shapes, as well as various geometric shapes such as circles, triangles, squares, hexagons, and octagons [11]; (e) Malay architectural ornaments (floral forms consist of *kaluk pakis*, *lilit kangkung*, *genting tak putus*, sagging flowers, jasmine flowers, mangosteen flowers, clove flowers, melur flowers, china flowers, forest flowers, sunflowers, *Ketola* flowers, *Kala Bukit* flower, *kiambang*, *tampuk pinang*, *pokok kolan*, *pucuk kacang*, *roda bunga*, *roda jangkar*, *pucuk rebung*, dan *sulo lalang*, Meanwhile, the fauna forms consist of horse saddles, ants with cascades, fish, hanging bees, flock of ducks, birds, elbows eagles, snakes, and fighting dragons. Natural shapes such as cloud motifs, star motifs, sun motifs, and various other decorations such as net ornaments, sunlight ornaments, violin trellis ornaments, and *ricih wajid* ornaments [12]; (f) Chinese architectural ornaments (geometric shapes with meander motifs, and animal shapes such as dragons, phoenixes, turtles, lions, deer, bats, and cranes) [13]; lastly (g) European architectural ornaments with distinctive characteristics such as geometric shapes of arches on doors and windows adoption of Islamic architecture, sloping roofs, walls made of *adobe*, porticoes, vertical bars on stairs and balconies or called *balustrade*, and *tympanums* [10].

2.6. Semiotics

Semiotics etymologically comes from the Greek word *simeon* which means "sign". Terminologically, semiotics can be defined as the science that studies a wide range of objects and events across cultures as signs [14]. According to Barthes, semiotics as the study of signs and their meanings in various human expressions such as language, art, mass media, music, etc., that can be reproduced or represented for an audience. Roland Barthes, an important figure in semiotics, considered it a part of linguistics and developed the concept of the *Order of Signification* [15]. In simple terms, Barthes' semiotic study can be described as follows:

The first level is denotation, which is the relation between the signifier and signified in a sign, and the sign with its reference, which refers to common-sense or the meaning of the sign that is obvious (the sign that is physically visible, not the meaning contained in the sign). The signifier is the material aspect of a discourse: what is seen, said, or heard. The signified is a sign that explains a 'concept' or 'meaning'.

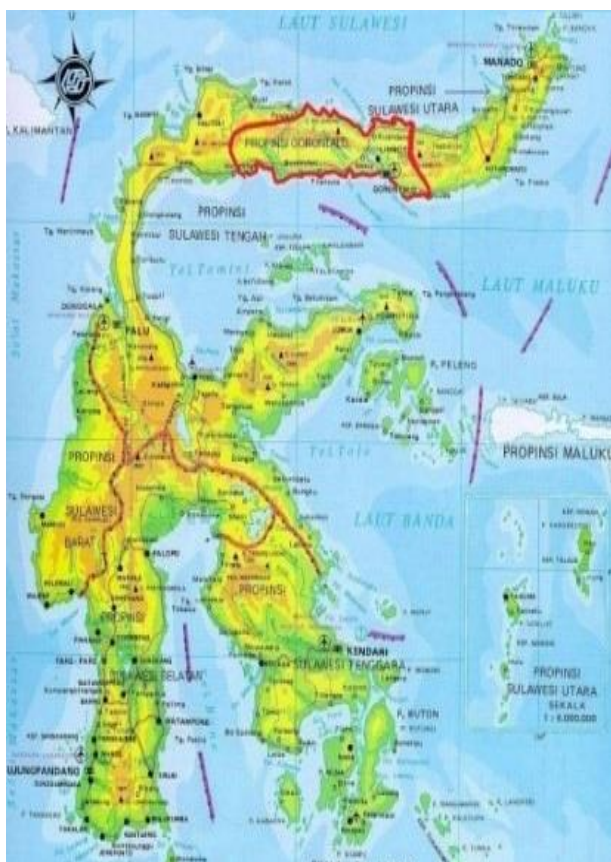
The second level is connotation, which refers to cultural meanings that arise or can also be called meanings that arise due to cultural constructions so that there is a shift, but still attached to the symbol or sign. Barthes (1968) expressed that connotation as an expression of culture.

The level of signification above can explain how myths and ideologies operate in texts through signs, where myths are a message containing an ideology.

In this study, the author used semiotics based on Roland Barthes' theory to examine the Denotative element, which studies the meaning of objects used in a sign, and the Connotative element, which discusses what is intended to be conveyed through a sign in the ornament of Hunto Sultan Amai Mosque in Gorontalo.

3. Research Method

The study is conducted in JL. HI. A. R. Konio. Bsc Gorontalo City, Kota Selatan District, Biawu Subdistrict (Figs. 2-4).



Information:
■ Gorontalo Province

Figure 2. Map of Sulawesi Island



Information:
■ Residential area
■ Hunto Sultan Amai Mosque
■ River of Bone

Figure 3. Map of Gorontalo City

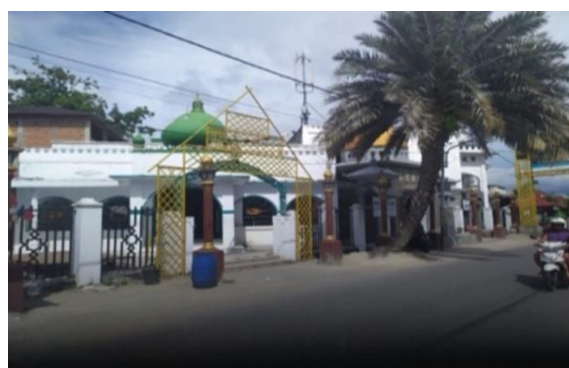


Figure 4. Hunto Sultan Amai Mosque in Gorontalo

It is a qualitative research that uses visual descriptive and explanatory analysis techniques with a semiotic approach. The research period spans two months, from July to September 2022. The data collection methods include observation, interviews, and documentation. The research focuses on the interior ornamentation of the Hunto Sultan Amai Mosque in Gorontalo, specifically examining the characteristics of the wall, window, pillar, pulpit, and mihrab elements, such as color, material, form, motif, and placement position. The study analyzes both the connotative and denotative meanings of these elements based on Roland Barthes' semiotic theory. The characteristics of the mosque's ornaments are shaped by various factors, including Indian, Arab, Malay, Middle Eastern, and Chinese architectures. In this study, there are several limitations, including: (1) the difficulty the authors faced in finding informants with a greater understanding of the architectural history of the Hunto Sultan Amai Mosque in Gorontalo; (2) all informants were unaware of the identity of the first architect who designed the Hunto Sultan Amai Mosque; (3) the authors did not find any specific documents or books that discuss the meaning of the colors of ornaments in the Gorontalo region or the unique ornaments of the Gorontalo region.

4. Results and Discussion

4.1. The history of Hunto Sultan Amai mosque, Gorontalo

The Sultan Amai Mosque is a prominent example of Islamic civilization in the Gorontalo Province due to the

crucial role played by Sultan Amai in the growth of Islam in Gorontalo. The residents' culture values harmony and is inspired by nature. Islam entered Gorontalo through the marriage of Raja Amai and Owutango a princess from the Muslim kingdom of Palasa located in Teluk Tomini. The princess had family ties to Ternate's royal family, who were already exposed to Islam, indicating their understanding and desire to govern according to Islamic teachings. "Because of Islam, the form of the kingdom became a sultanate" [2].

Sultan Amai had to convert to Islam before marrying the Muslim princess of the Palasa kingdom. The requirements included (1) the conversion of Raja Amai and the people of Gorontalo to Islam, and (2) the customs and traditions in Gorontalo society must be based on the Quran. To solidify his conversion, Sultan Amai built a mosque as a dowry for his marriage to the princess of Palasa. [2]. As reported by a few interviewees:

".....then the condition for this proposal was accepted by Raja Palasa (the father of Princess Boki Autango) who said it was allowed (his daughter to be proposed by Raja Amai), but you had to convert to Islam and you had to prove it by building a mosque. That's why this mosque was built in 1495, it is related to the wedding dowry." (Samsuri Kaluku, as the Ta'mirul Hunto Sultai Amai Gorontalo Mosque, July 28, 2022).

The mosque underwent many renovations over five centuries, now the white and green building's appearance has been enhanced with contemporary additions like a dome, tower, second floor, and all structures are now made of brick structures [16], confirmed by interviewees:

"the mosque has undergone countless renovations since its establishment, and it has never ceased to be constructed. The only original elements left are the well and the pulpit, as the bedug had been replaced." (Sarif Qidam, as a worshipper of the Hunto Sultai Amai Mosque in Gorontalo, August 4, 2022)

The interview excerpt reveals that the Hunto Mosque has undergone several renovations, with the most notable one taking place inside the mosque. The interior decorations were designed to look like the Ar-Raudha Park located in Masjid al-Haram. Wooden pillars replaced with concrete, collapsed ceiling with gypsum panels. Nevertheless, The unchanged original ornaments in the mosque include the pulpit in the main hall/liwan and the well in front of the support room.

The mosque has an old well in its southern section built using limestone and maleo bird egg whites [16]. As a result of this historical artifact, the mosque has been designated as one of Gorontalo City's Cultural Heritage Sites, as per the regulations outlined in UU No. 11 of 2010, Article 11 on Cultural Heritage.

4.2. Layout of the mosque

The mosque's architecture is distinct, evident in the building's corners. The primary prayer hall measures 17 x 12 meters, with a white floor adorned with red lines. The walls are split into two sections: the upper part made of white brick and the lower part covered in 10x20 ceramic tiles, featuring white and red patterns, measuring 57 cm

high. Each wall has an iron window, measuring 2 x 1 meters, with calligraphic decorations in the center. The Hunto Sultan Amai Mosque in Gorontalo features an interior divided into a *liwan* space, a waiting room, a support room, a mihrab, a pulpit, walls, pillars, ceiling, and windows (Fig. 5 and Fig. 6).

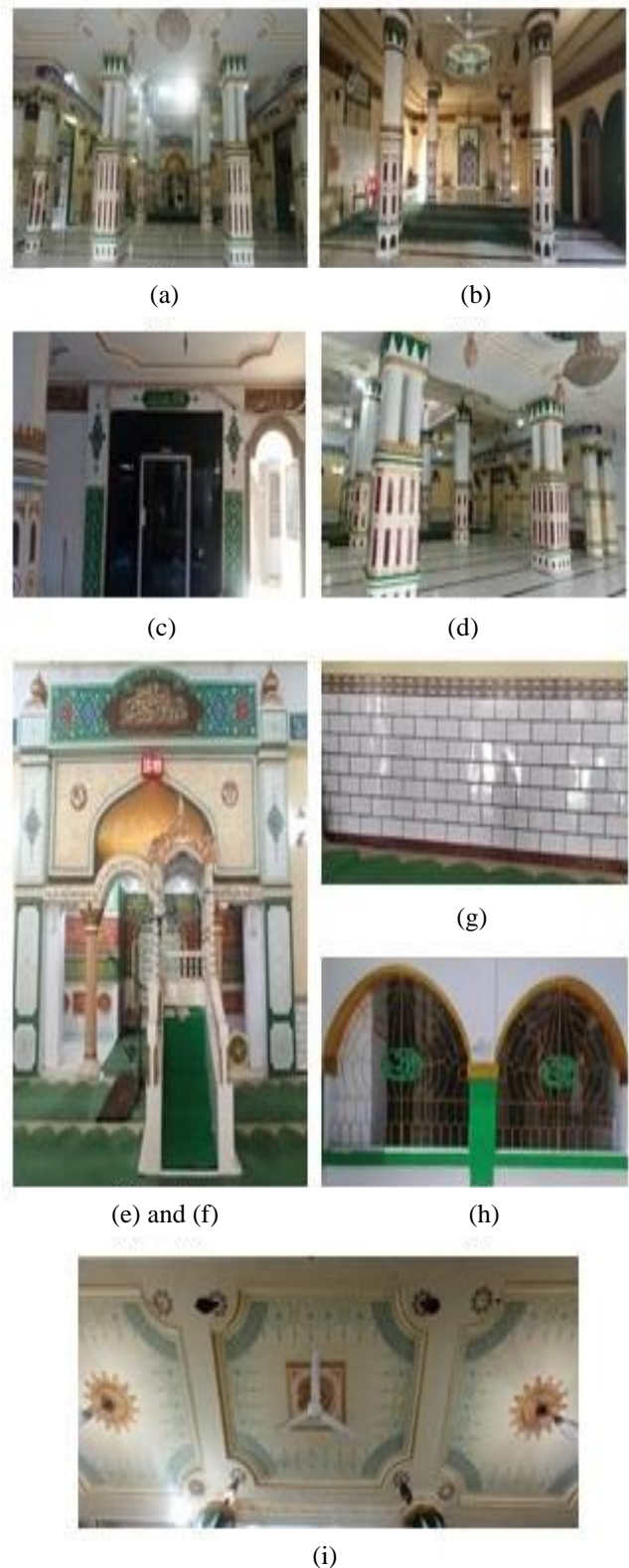
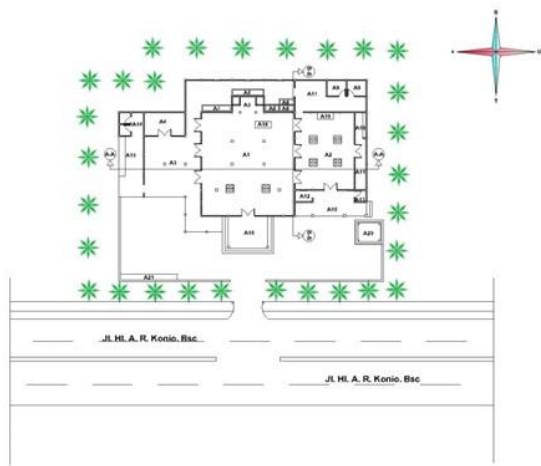


Figure 5. Interior ornaments of the mosque. (a) Main hall/liwan, (b) Women's prayer room/pawestren, (c) Supporting spaces, (d) Columns, (e) Mihrab, (f) Mimbar, (g) Walls, (h) Windows, (i) Ceiling



- | | |
|---------------------------------------|---------------------------|
| A1 : Main room/liwan | A13 : Women's toilet |
| A2 : Pawestren/women's prayer room | A14 : Men's toilet |
| A3 : Additional room/supporting room | A15 : Men's ablution area |
| A4 : Administration room | A16 : Terrace |
| A5 : Mihrab room | A17 : Garden |
| A6 : Tomb of Sultan Amay Gorontalo | A18 : Mimbar |
| A7 : Tomb of Sheikh Syarif Abdul Aziz | A19 : Mihrab |
| A8 : Tomb of the Islamic scholars | A20 : Tower |
| A9 : Warehouse | A21 : Men's ablution area |
| A10 : Women's ablution area | A-A : Section A-A |
| A11 : Kitchen | B-B : Section B-B |
| A12 : Women's ablution area | |

Figure 6. Mosque site plan

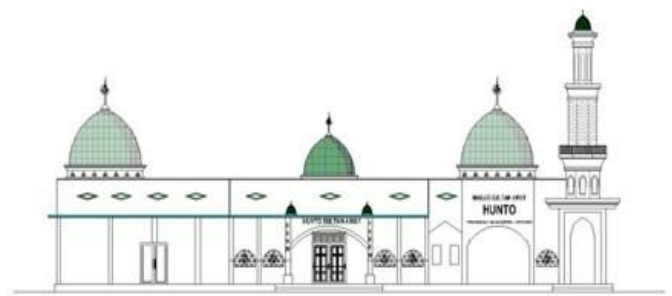


Figure 8. Mosque front view

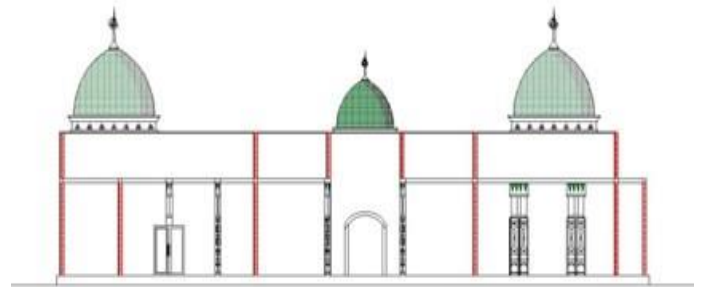
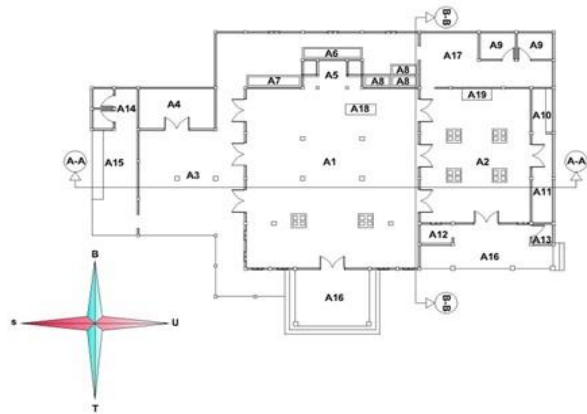


Figure 9. Section A-A of the mosque

4.3. The study of mosque characteristics

The research object focused on the ornaments found in the main prayer hall (A1), women's prayer hall (A2), and support room (A3) with observed elements ranging from the *mihrab*, pulpit, walls, pillars, windows, ceiling, to the windows in each room. (Figs. 7-10).



- | | |
|---------------------------------------|-----------------------------|
| A1 : Main room/liwan | A12 : Women's ablution area |
| A2 : Pawestren/women's prayer room | A13 : Women's toilet |
| A3 : Additional room/supporting room | A14 : Men's toilet |
| A4 : Administration room | A15 : Men's ablution area |
| A5 : Mihrab room | A16 : Terrace |
| A6 : Tomb of Sultan Amay Gorontalo | A17 : Garden |
| A7 : Tomb of Sheikh Syarif Abdul Aziz | A18 : Mimbar |
| A8 : Tomb of the Islamic scholars | A19 : Mihrab |
| A9 : Warehouse | A-A : Section A-A |
| A10 : Women's ablution area | B-B : Section B-B |
| A11 : Kitchen | |

Figure 7. Mosque floor plan

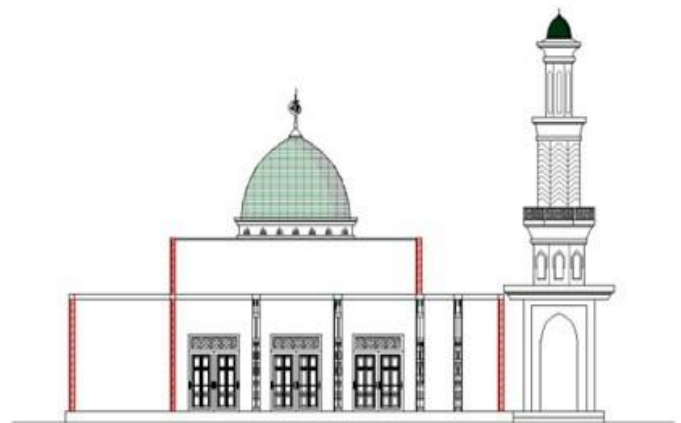














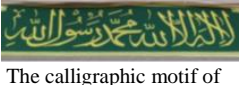

Figure 10. Section B-B of the mosque





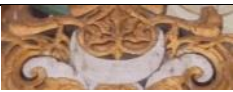

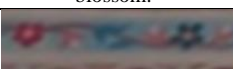
4.4. Characteristics and meanings of mosque ornaments







There are a total of 49 observed ornaments in the Hunto Sultan Amay Mosque in Gorontalo, with 34 ornaments located in the main hall (*liwan*) of the mosque, 9 ornaments in the women's prayer room (pawestren), and the remaining 6 ornaments in the supporting spaces. Table 1 summarizes the explanation of the connotative and denotative meanings as well as the types of ornaments found in each room of the Hunto Sultan Amay Gorontalo Mosque.



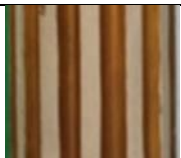






Table 1. Variety of foreign cultural architectural forms along with their motifs


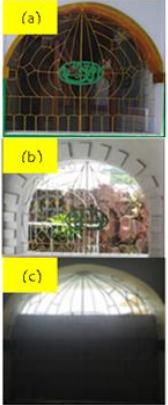
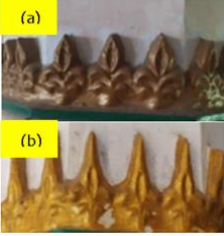
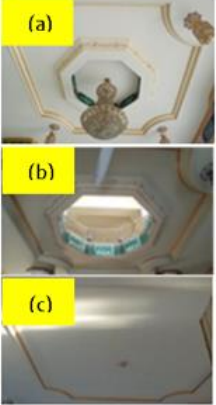
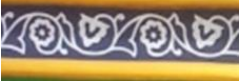
No	Type of Ornament	Form of Ornament Section	Placement Position	Denotative Meaning	Connotative Meaning
1	Chinese Ornaments	 Meander motif	The bottom wall of the window in the main hall of Hunto Sultan Amai Mosque, Gorontalo	Geometric shape of the meander motif resembles yin-yang, made of porcelain/ceramic material, colored in brown with additional red lines.	<i>Yin</i> and <i>yang</i> are symbols in Chinese society that represent the principles of natural forces. <i>Yin</i> is associated with the moon (darkness, water, and feminine principles), while <i>yang</i> is associated with the sun (brightness, fire, and masculine principles). The color brown symbolizes comfort, simplicity, and classic yet modern, while the color red represents brotherhood, courage, hope, luck, and happiness.
2	Middle East Ornament	 Calligraphy Khat Naskhi motif featuring an excerpt from Q.S Ali 'Imran ayat 190	The upper wall of the main hall of Hunto Sultan Amai Mosque, Gorontalo	The calligraphy is in Khat Naskhi of Q.S Ali 'Imran ayat 190. It is made of paint, colored in blue as the base color, with white color on the calligraphy.	Surah Ali 'Imran (3:190) contains signs of the greatness of Allah SWT, which include the creation of mankind and the universe, as well as the alternation of day and night. The color blue symbolizes the power of the ocean, while white represents purity.
3	Middle East Ornament	 Calligraphy Khat Naskhi motif featuring an excerpt from Q.S Al-Anam ayat 98	The upper wall of the main hall of Hunto Sultan Amai Mosque, Gorontalo	The calligraphy is in Khat Naskhi of Q.S Al-Anam ayat 98. Made of paint, colored in green as the base with white color on the calligraphy's writing.	The verse from Surah Al-Anam: 98 concludes that the signs of Allah's greatness are known only to those who believe in Allah SWT. The color green symbolizes the identity of the Islamic religion.
4	Arab and Middle East Ornament	 Basic square/rectangle pattern and Calligraphy Khat Naskhi motif featuring an excerpt from Q.S Al-Fatihah ayat 1-7	The wall of the Mihrab in the main hall of Hunto Sultan Amai Mosque, Gorontalo	The ornament is shaped in a square and filled with calligraphy in the Khat Naskhi reciting ayat 1-7 of Surah Al-Fatihah. It is made of paint, colored in white as the base color, black for the calligraphy, and gold for the square shape.	The square pattern, which is given the meaning of "Symbol of physical experience and the physical world of materiality" meaning "A symbol of real-life experiences and the physicality of the world". This ornament features the theme of Ummul Qur'an (Q.S Al-Fatihah:1-7) which is the essence of the entire Qur'an. The calligraphy is written in a cursive Khat Naskhi, which is a rounded and easily readable script. The color white symbolizes purity, black symbolizes power, and gold symbolizes glory and authority.
5	Arab and Middle East Ornament	 Basic circle pattern and calligraphy Khat Diwani motif featuring Ar-Rahman	The side wall of the Mihrab in Hunto Sultan Amai Mosque, Gorontalo	Geometrically shaped ornament with circular patterns and calligraphy. The calligraphy is in Khat Diwani and features one of the Asmaul Husna, which is Ar-Rahman. Made of paint, colored with a blue base and white on the edges of the circles and the calligraphy.	The circular pattern ornament is given the meaning of "Symbol of eternity, perfect expression of justice". The calligraphy which reads Ar-Rahman means "The Most Compassionate". The Diwani style used in the calligraphy is an Ottoman writing pattern. The color blue symbolizes power in the ocean, while the color white symbolizes purity.
6	Middle East Ornament	 Calligraphy Khat Tsuluts motif featuring an excerpt from Q.S Al-Baqarah ayat 261	The wall of the Mihrab in the main hall of Hunto Sultan Amai Mosque, Gorontalo	The calligraphy on this ornament uses the Khat Tsuluts and features a verse from Surah Al-Baqarah: 261. It is made of paint, colored with a red base and gold on the calligraphy.	The use of Tsuluts script in the calligraphy is as an ornamental writing on the walls of the interior of the mosque. The verse from Surah Baqarah: 261 means that whatever a servant (human being) does will receive rewards from Allah SWT in accordance with their deeds. The gold color symbolizes triumph and power, while the red color symbolizes brotherhood, bravery, hope, luck, and happiness.
7	Middle East Ornament	 Calligraphy Khat Tsuluts motif featuring an excerpt from Q.S Al-Fath ayat 29	The wall of the Mihrab in the main hall of Hunto Sultan Amai Mosque, Gorontalo	The calligraphy on this ornament uses the Khat Tsuluts and features a verse from Surah Al-Fath: 29. It is made of paint, colored with a green base and gold on the calligraphy.	The calligraphy comes from the Tsuluts script, which is used as ornamental writing on the walls of the interior of the mosque. The verse from Surah Al-Fath: 29 means that if a person does good deeds, even as small as a mustard seed, Allah will reward them by multiplying their good deeds. The gold color symbolizes triumph and power, while the green color symbolizes the Islamic religion.




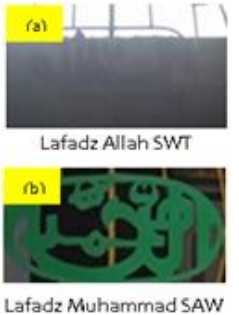


No	Type of Ornament	Form of Ornament Section	Placement Position	Denotative Meaning	Connotative Meaning
8	Middle East Ornament	 Calligraphy Khat Tsuluts motif featuring an excerpt from Q.S Al-Ankabut ayat 45	The upper wall of the window in the main hall of Hunto Sultan Amai Mosque, Gorontalo	The calligraphy style used is the tsuluts script, featuring a verse from Surah Al-Ankabut ayat 45. Made of paint, with a dominant color scheme of red and gold.	The meaning Surah Al-Ankabut ayat 45 is that reading the Quran and performing prayers are commands from Allah. The calligraphy is derived from the tsuluts script, which is a decorative writing style found on the walls of the interior spaces of mosques. The color red signifies brotherhood, courage, hope, luck, and happiness, while gold represents triumph and power.
9	Middle East Ornament	 Calligraphy Khat Tsuluts motif featuring an excerpt from Q.S Al-Baqarah ayat 144	The upper wall of the Mihrab in the main hall of Hunto Sultan Amai Mosque, Gorontalo	The calligraphy style used is the tsuluts script, featuring a verse from Surah Al-Baqarah: 144. Made of paint, with a dominant color scheme of brown and gold.	The calligraphy is derived from the tsuluts script, which is a decorative writing style found on the walls of the interior spaces of mosques. Surah Al-Baqarah ayat 144 talks about the direction of prayer being changed towards the Ka'bah as a decree from Allah SWT. The color brown symbolizes comfort, simplicity, and classic yet modern design, while gold represents triumph and power.
10	Middle East Ornament	 The calligraphic motif of the Tsuluts script featuring an excerpt from Quranic verse Al-Baqarah:255 (Ayat Kursi).	The interior dome walls of the Hunto Sultan Amai Mosque, Gorontalo.	The calligraphic form employed is of the Tsuluts Khat/script, which is characterized by the utilization of a segment from the Quranic verse Al-Baqarah: 255. The medium of creation is paint, while the color scheme comprises red as the primary hue, with white accentuating the calligraphic lettering.	The calligraphic inscription is derived from the Tsuluts script, which is used for decorative purposes on the interior walls of mosque buildings. The verse Al-Baqarah: 255, also known as the "Ayat Kursi," illustrates the omnipotence of Allah the Almighty in all matters. The color red is indicative of fraternity, bravery, optimism, good fortune, and bliss, while white is a representation of purity.
11	Middle East Ornament	 The calligraphic motif of the Tsuluts script featuring an excerpt from Quranic verse Al-Ahzab:21	The upper section of the Mihrab Pawestren at the Hunto Sultan Amai Mosque, Gorontalo.	The calligraphic form utilized is the Tsuluts script, featuring a segment from Quranic verse Al-Ahzab:21. Created using paint as a medium, the calligraphic lettering is colored predominantly in green and yellow.	The calligraphic writing is derived from the Tsuluts script, which is a decorative script found on the interior walls of mosque buildings. The segment from Quranic verse Al-Ahzab:21 describes how Prophet Muhammad SAW is the role model for those who seek Allah's mercy on the Day of Judgment. Green signifies the color associated with Islam, while yellow represents magnificence, fertility, and prosperity in life.
12	Middle East Ornament	 The calligraphic motif of the Tsuluts script featuring an excerpt from Quranic verse Al-Isra:81	The upper walls of the Pawestren section at the Hunto Sultan Amai Mosque, Gorontalo.	The calligraphic form utilized is the Tsuluts script, featuring a segment from Quranic verse Al-Isra: 81. Created using wood and paint as a medium, the calligraphic lettering is colored in red, with gold ornamentation and edging	The calligraphic writing is derived from the Tsuluts script, which is a decorative script found on the interior walls of mosque buildings. The segment from Quranic verse Al-Isra:81 describes the distinction between truth and falsehood. Red signifies brotherhood, courage, hope, luck, and happiness, while gold symbolizes triumph and power
13	Middle East Ornament	 The calligraphic motif of the Tsuluts script featuring the declaration of faith (Shahada)	The upper walls of the supporting room in the Hunto Sultan Amai Mosque, Gorontalo	The calligraphic writing is in the Tsuluts script, featuring the recitation of the tahlil as part of the declaration of faith. It is painted using green as the primary color, and yellow for the calligraphic writing.	Tsuluts calligraphy is a form of decorative writing that is often found on the inner walls of mosque interiors. The statement of faith, or Tauhid, is the key to open the gates of paradise. By worshipping only Allah, one can achieve the level of piety, as stated in the Quranic verse Al-Baqarah: 21. The color yellow symbolizes magnificence, fertility, and prosperity in life, while green is commonly associated with Islam.
14	Arabic and Malay Ornament	 The basic pattern of a circle and the motif of a sunflower	Plafon Mihrab Liwan Masjid Hunto Sultan Amai, Gorontalo	The geometric shape is that of a circle and the floral shape is that of a sunflower. Made from polycarbonate (PC) material, colored in gold, yellow, white, and reddish-brown	The basic pattern ornament in the shape of a circle, given the meaning: 'Symbol of eternity, perfect expression of justice,' while the sunflower motif symbolizes peace, harmony, and a comfortable hope for its inhabitants. The color gold symbolizes triumph and power, yellow represents grandeur, fertility, and prosperity in life, white represents purity, and the reddish-brown color combines the meanings of red and brown, where red represents fraternity, courage, hope, luck, and happiness, while brown symbolizes comfort, simplicity, classic but still modern

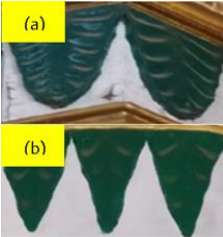
No	Type of Ornament	Form of Ornament Section	Placement Position	Denotative Meaning	Connotative Meaning
15	The Arabic, Middle Eastern, and Malay ornament	 <p>The arch motif (Arab), the calligraphy motif of Kufic script with a fragment from verse 56 of Surah Al-Ahzab (Middle Eastern), and the creeping water spinach motif (Malay)</p>	The Mihrab Liwan Gateway of Hunto Sultan Amai Mosque, Gorontalo	The geometric shape of the arch motif. Its floral shape is creeping water spinach, and its calligraphic form is from the Kufic script reciting a verse from Surah Al-Ahzab:56. Made from paint, it is colored with a white base, gold for the arch lines, green for the calligraphic writing, and yellow for the floral ornament part	The arch motif symbolizes elegance, movement, and growth. The creeping water spinach motif has the meaning of an unquenchable spirit, always moving forward despite obstacles, but with goals adjusted to the prevailing conditions. The Kufic script is called “khath Muzawwa”, which is an Arabic writing that has an angular shape. The excerpt from Surah Al-Ahzab: 56 urges human beings to always send blessings and greetings to the Prophet Muhammad, who is the last prophet (the prophet of the end times). Gold represents triumph and power, white represents purity, green represents the color that is synonymous with Islam, and yellow represents grandeur, fertility, and prosperity in life
16	Arabic and Malay Ornament	 <p>The geometric shape of the basic pattern is the curve, while the floral shape is the Clove Flower motif</p>	The wall of the Mihrab Liwan in the Hunto Sultan Amai Mosque, Gorontalo	The floral shape originates from the Clove Flower motif, while the geometric shape is the curve. It is made of a material called paint and colored with a base color of blue, with gold lines on the curve, and green and blue colors on the ornamental growth	The motif of the arch represents elegance, movement, and growth. When associated with the carnation flower, it signifies grandeur. The color gold symbolizes triumph and power, while green represents the identity of Islam. The color blue represents strength in the ocean
17	Arabic and Malay Ornament	 <p>The geometric shape of the basic pattern is an arch, while the floral shape is derived from the clove flower</p>	Mihrab Pawestren in the Back Gate of Hunto Sultan Amai Mosque, Gorontalo	The geometric shape of the design consists of a curved motif, while the floral shape is that of a clove flower. The design is composed of a base material and is colored using paint, with red used for the edges of the curved lines, green for the edges of the clove flower ornamentation, and pink for the clove flower ornamentation itself.	The curved motif symbolizes elegance, movement, and growth. When combined with the clove flower ornamentation, it represents grandeur. The use of green represents the Islamic faith, while red symbolizes brotherhood, courage, hope, luck, and happiness. The pink color has no specific meaning but is used for aesthetic purposes, and the use of white represents purity.
18	Malay Ornament	 <p>The natural form is patterned after clouds.</p>	The dome ceiling in Hunto Sultan Amai Mosque, Gorontalo	The dome is shaped like a natural cloud and is colored white. The base material used is paint, with blue as the dominant color. This dome ornamentation is an adaptive representation of the original sky that is present in Masjidil Haram.	The cloud motif in this ornamentation does not have any specific meaning but is used as an adaptation of the original cloud shape. The color white represents purity, while blue symbolizes power in the ocean.
19	Malay Ornament	 <p>The natural form is patterned after a crescent moon.</p>	The gateway to the Minbar in the Hunto Sultan Amai Mosque, Gorontalo.	The natural shape of the ornamentation is in the form of a white crescent moon and is made of lingua wood.	The natural ornamentation of the crescent moon is often combined with a star motif, signifying devotion to Allah the Almighty. The color white symbolizes purity.
20	Malay Ornament	 <p>The fauna motif depicts bees hanging on a garden blossom.</p>	The ceiling surrounding the dome in the Hunto Sultan Amai Mosque, Gorontalo.	The fauna ornamentation features a hanging motif of bees with a combination of flower buds. The base material used is gypsum ceiling, with a dominant color of gold and green.	The fauna ornamentation features a hanging motif of bees with a combination of flower buds. The base material used is gypsum ceiling, with a dominant color of gold and green.
21	Malay Ornament	 <p>The floral motif is shaped like forest flowers.</p>	The inner wall of the dome in the Hunto Sultan Amai Mosque, Gorontalo.	The floral ornamentation features colorful forest flowers with different colors for each flower, using paint as the base material, dominated by blue and red.	The Forest Flower motif symbolizes diversity in community life. The color red represents brotherhood, courage, hope, luck, and happiness, while the color blue symbolizes strength and power in the ocean.

No	Type of Ornament	Form of Ornament Section	Placement Position	Denotative Meaning	Connotative Meaning
22	Malay Ornament	 The floralis motif is shaped like unbroken roof tiles.	The upper section of the gateway to the Mihrab in the Liwan area of the Hunto Sultan Amai Mosque.	The roof ornamentation features an unbroken pattern of flower motifs, made of cement and colored with a base color of gold.	The unbroken pattern of roof tiles symbolizes the difficulties of human life, as difficult times are not permanent and will eventually give way to better times. Similarly, good times will not last forever either. The use of the color gold represents triumph and power.
23	Malay Ornament	 The floralis motif is shaped like Ketola flowers.	The ceiling of the Mihrab in the Liwan area of the Hunto Sultan Amai Mosque, Gorontalo.	The floral pattern used in this ornamentation is based on the shape of the ketola flower. It is made from polycarbonate material and features gold coloration around the edges of the ornament, with a green and yellow color scheme forming the basis of the ketola flower motif.	The motif of the ketola flower has a symbolic meaning of beauty. The color gold represents glory and power, the color green represents the identity of Islam, and the color yellow symbolizes majesty, fertility, and prosperity in life. The ornament is made of PC (polycarbonate) material and is colored with gold around the ornament, while green and yellow colors underlie the motif of the ketola flower.
24	Arab and Malay Ornament	 The basic pattern of square, arch, and lotus flower (Arab), as well as the "kaluk pakis" motif (Malay).	The upper section of the Pawestren Mihrab in the Hunto Sultan Amai Mosque, Gorontalo.	The geometric shape of the motif consists of squares and curves, while the floral shape is composed of lotus flowers and "kaluk pakis" motifs. It is made of paint and colored with white and black on the curved parts, gold and red on the lotus flower ornament, and white on the "kaluk pakis" ornament.	The basic pattern is in the form of a square and carries the meaning of "Symbol of physical experience and the physical world of materiality," while the curvature motif symbolizes elegance, movement, and growth. The "Kaluk pakis" motif has symbolic meaning to suggest fertility and prosperity. The lotus flower's meaning teaches us about adaptation and idealism. White represents purity, black represents strength, and gold represents triumph and power.
25	Malay Ornament	 The fauna motif depicts a flock of ducks.	The upper section of the entrance to the Liwan Mosque in Hunto Sultan Amai, Gorontalo.	The fauna motif takes the form of a flock of ducks arranged in the shape of the letter S. It is made of linggua wood and predominantly white in color.	The motif of a flock of ducks holds meanings of mutual cooperation, bravery, togetherness, familial bond, solidarity, and freedom. The color white symbolizes purity.
26	Arabic, Middle East, and Malay Ornament	 The design includes geometric patterns of squares and circles (Arabic), floral motifs of jasmine flowers (Malay), and calligraphic designs of the names Allah and Muhammad in the khat tsuluts script.	The entrance pillars of the Liwan Mosque in Hunto Sultan Amai, Gorontalo.	The geometric motif consists of circular patterns containing calligraphy of the Tsuluts script with the words of Allah and the Prophet, as well as square shapes. The floralis motif features jasmine flowers. The materials used in its construction are paint and cement, and it is primarily colored in white with green edges, while the calligraphic script is in gold and the floral ornamentation is predominantly green.	The square pattern is given the meaning of "Symbol of physical experience and the physical world of materiality", representing the tangible and material aspects of the real world. The circular pattern is given the meaning of "Symbol of eternity, perfect expression of justice", representing the eternal and perfect expression of justice. The jasmine flower symbolizes purity. The calligraphic script of Allah the Almighty and the Prophet Muhammad SAW is an integral part of most ornaments found in every mosque, and is written in the Tsuluts script as decorative writing on the inner walls of the mosque. The color green represents the identity of Islam, while the color gold represents victory and power, and the color white symbolizes purity
27	Malay Ornament	 The floral pattern is a combination of lotus and water lily flowers.	The supporting room walls of the Hunto Sultan Amai Mosque, Gorontalo.	The basic form of this motif is the jasmine flower, but its interior is filled with lotus flowers or lotus vines. It is made of paint and is colored green for the jasmine flower, while the interior with the lotus vines is painted yellow.	The meaning of lotus flowers teaches us about adaptation and idealism. The meaning of jasmine flowers is the same as the meaning of jasmine flowers, which symbolizes purity. The color yellow symbolizes grandeur, fertility, prosperity in life, and the color green is synonymous with Islam.

No	Type of Ornament	Form of Ornament Section	Placement Position	Denotative Meaning	Connotative Meaning
28	Middle East Ornament	 <p>The calligraphy is written in Kufic script with the words of Asmaul Husna</p>	The central part of the ceiling in the Pawestren of the Hunto Sultan Amai Mosque, Gorontalo	The calligraphy shape is from the Kufic style, features the Asmaul Husna (the names of Allah), written in white color with a green background, and made of paint material. The ornament lines are adorned with gold color on the edges.	The Asmaul Husna has its own special characteristics, one of which is as a prayer. The Asmaul Husna that appears in this ornament are Ar-Raḥîmu, which means The Most Compassionate, Al-Maliku, which means The Supreme Ruler, and lastly Al-Quddûsu, which means The Most Holy. The calligraphy is written in khat koufi, which is another name for khath Muzawwa, an Arabic script that has an angular shape. The green color symbolizes the identity of Islam, while gold represents glory and power, and white represents purity.
29	Arabic and Middle East Ornament	 <p>The basic pattern of the design features curved lines and is accompanied by the calligraphy of Kufic script with the words "Shalawat Fatimah Az Zahrah"</p>	The side entrance of the Mihrab Pawestren of the Hunto Sultan Amai Mosque, Gorontalo	The calligraphy form is from the Khat Koufi style, featuring the words of the Shalawat Fatimah Az-Zahra. The calligraphy is made of cat material, colored with a white base color, and decorated with gold on the curved lines and green on the calligraphic text.	The curved motif represents elegance, movement, and growth. The calligraphy inside it, written in the khat koufi style, contains the Shalawat Fatimah Az-Zahra. It is made of paint and colored in white as the base color, with gold on the curved lines and green on the calligraphic writing. The companions of the Prophet Muhammad, who generally had their own version of Shalawat, mention the contents of the calligraphy in various narrations. Similarly, Sayidah Fatimah, the daughter of Prophet Muhammad, composed her own version of Shalawat, which is mentioned in the book Al-Ibriz Min Kalami Sayyidi Abdil Aziz by Ahmad Ibnul Mubarak Al-Maliki. The green color symbolizes the identity of Islam, while the gold color represents glory and power, and the white color symbolizes purity.
30	Arabic Ornament	 <p>The geometric shape is a vertical line motif.</p>	The column of the Mihrab Liwan of Masjid Hunto Sultan Amai, Gorontalo	The ornament shape is in the form of vertical line motifs that are colored in gold. It is made from shaped cement.	The motif of straight lines conveys the meaning of strength and resistance. Vertical straight lines signify stability, strength, or grandeur. The color gold symbolizes victory and power.
31	Arabic Ornament	 <p>The geometric shape of the basic triangle motif pattern</p>	"The roof of the pulpit in the Hunto Sultan Amai Mosque, Gorontalo	A geometric shape with an isosceles triangle motif. Colored in gold and made of lingua wood.	The fundamental design features a triangular shape, which symbolizes humanity, consciousness, and the principle of harmony. The color gold is used to represent triumph and power.
32	Arabic Ornament	 <p>The basic pattern motif is in the form of a circle</p>	The bottom part of the main pillar in the Liwan of Hunto Sultan Amai Mosque, Gorontalo.	The geometric shape features a large, thin circle motif with smaller circles inside that resemble egg yolks. Both are colored in gold and white, and made from molded cement.	The basic pattern is in the shape of a circle, with the meaning of 'Symbol of eternity, perfect expression of justice'. The color white symbolizes purity, while the color gold represents triumph and power.
33	Middle East ornament	<p>Kufic calligraphy with the phrase/word of</p>  <p>Baabul Hijrah</p>  <p>Baabul Marwah</p>  <p>Baabul Malik</p>	The upper section of the door wall located adjacent to the Liwan in the Hunto Sultan Amai Mosque, situated in Gorontalo.	The calligraphic style is in the Kufic script, featuring the Arabic names of the doors in Masjidil Haram. The writing is created using paint and colored in a base shade of blue, with the calligraphic inscription appearing in white.	The calligraphy features the names of the doors in Masjidil Haram, specifically Baabul Hijrah, Baabul Marwah, and Baabu Malik. These doors are commonly used as meeting places for congregants. The calligraphic script used is in the Kufic style, also known as khath Muzawwa, characterized by its angular and geometric appearance. The color white represents purity, while blue symbolizes power and strength in the ocean.
34	Middle East Ornament	<p>Kufic calligraphy with the phrase/word of 'Baabus Salam'</p> 	The upper part of the entrance wall adjacent to the Liwan in Hunto Sultan Amai Mosque, situated in Gorontalo	The calligraphic style used on the upper part of the entrance wall adjacent to the Liwan in Hunto Sultan Amai Mosque, situated in Gorontalo, features the Arabic phrase from one of the largest doors in Masjidil Haram, Baabus Salam. The writing is created using paint and	The calligraphy is in the Kufic script, featuring the Arabic name "Baabus Salam" which is one of the largest gates in Masjid al-Haram, meaning "Gate of Peace". This gate is located between Mount Safa and Marwah. The writing is created using paint and colored in a base shade of blue, with the calligraphic inscription appearing in white. The calligraphic style is in the Kufic script, which is also known as "Khath Muzawwa," a form of Arabic writing with angular shapes. The color white represents purity and the color blue symbolizes power in the ocean.

No	Type of Ornament	Form of Ornament Section	Placement Position	Denotative Meaning	Connotative Meaning
				colored in a base shade of blue, with the calligraphic inscription appearing in white.	
35	Arabic Ornament	 <p>Geometric pattern of Prismatic/rhythmic Curves Motif</p>	The lower part of the main pillar of the Liwan in the Hunto Sultan Amai Mosque, Gorontalo	The lower part of the main pillar in the Liwan of the Hunto Sultan Amai Mosque in Gorontalo features a geometric shape with a prismatic motif. The ornament is made from shaped cement and colored with a white base and red hues on the prismatic motif	The prism motif or rhythmic curve symbolizes gracefulness and elegance, while the white color represents purity. The red color signifies brotherhood, courage, hope, luck, and happiness.
36	Arabic Ornament	<p>Geometric pattern of Prismatic/rhythmic Curves Motif</p> 	(a) The front window of the Liwan of Hunto Sultan Amai Mosque, Gorontalo. (b) The side window of the Liwan of Hunto Sultan Amai Mosque, Gorontalo. (c) The Pawestren window of Hunto Sultan Amai Mosque, Gorontalo.	It has a geometrical shape with a prismatic/rhythmic curve motif. It is made of iron and colored in gold on the iron frame of ornaments (a) and (b), while ornament (c) is white in color and made of iron.	The prismatic/rhythmic curve motif represents gracefulness and flexibility. The color gold symbolizes prosperity, victory, and power, while the color white represents purity and sincerity
37	Malay Ornament	<p>The floral motif of Bamboo Shoot</p> 	(a) The upper pillar of the Pawestren section of the Hunto Sultan Amai Mosque, Gorontalo (b) The upper pillar of the supporting room of the Hunto Sultan Amai Mosque, Gorontalo	The floralis form of the bamboo shoot motif. Made of carved iron material and predominantly colored in gold.	The bamboo shoot motif represents fertility and happiness in human life. The "Bamboo Shoot" motif is a form of decoration made from the enrichment of young bamboo stems or shoots. The color gold symbolizes triumph and power.
38	Arabic Ornament	<p>The geometric shape of the basic octagonal pattern motif.</p> 	(a) Ceiling of the entrance door of the Liwan of Hunto Sultan Amai Mosque in Gorontalo. (b) Middle ceiling of the Pawestren of Hunto Sultan Amai Mosque in Gorontalo. (c) Ceiling of the supporting rooms of Hunto Sultan Amai Mosque in Gorontalo.	It has a geometric shape with an octagonal basic pattern motif. Made of gypsum ceiling material and colored with a white base and gold on the octagonal geometric shape.	The basic pattern is in the form of an octagon or polygon, with the meaning of "Symbol of the God light, spreading the Islamic Faith". The color gold represents glory and power, while white represents purity. The pattern is made of gypsum ceiling and is colored with a white base and gold on the octagonal geometric shapes.
39	Malay Ornament		The wall of the mihrab in the Liwan of	The floral ornament shape is called "Kaluk Pakis". It is made of painted material	The "kaluk pakis" ornament motif carries a symbolic meaning to imply fertility and prosperity. The blue color represents the power of the ocean, while the gold color

No	Type of Ornament	Form of Ornament Section	Placement Position	Denotative Meaning	Connotative Meaning
		The floral motif called "Kaluk Pakis"	the Hunto Sultan Amai Mosque, Gorontalo.	with gold color on the edges of the ornament, blue as the base color, and white.	represents victory and power, and the white color symbolizes purity. It is made of painted material, with gold color on the edges of the ornament, blue as the base color, and white color as well.
40	Malay Ornament	 The floral motif called "Lilit Kangkung"	The side part of the Minbar of Hunto Sultan Amai Mosque, Gorontalo.	The floral motif has the shape of a creeping water spinach, called "lilit kangkung" in Indonesian. It is made of Linggua wood and colored with gold.	The <i>lilit kangkung</i> ornament has a symbolic meaning of an unyielding spirit, to keep moving forward despite obstacles, but with goals adapted to the current circumstances. The color gold represents triumph and power.
41	Malay ornament	 The climbing plant shape in Javanese language is called "Lung-Lungan".	The gateway of the Mimbar in Hunto Sultan Amai Mosque, Gorontalo.	The floral motif of lung-lungan or climbing plants is painted with gold color and made of linggua wood.	The ornamental carving of climbing plants has a symbolic meaning of beauty and a hidden message to convey to the visitors who come to pray to always care about the beauty of their surroundings. The color gold represents triumph and power.
42	Malay Ornament	The floral motif called "Tampuk manggis" 	(a) Column at the entrance door of Liwan in Hunto Sultan Amai Mosque, Gorontalo (b) Side column of the mihrab in Hunto Sultan Amai Mosque, Gorontalo	The floral shape of the <i>tampuk manggis</i> motif. Made of paint and painted predominantly in gold color.	The floral form of "tampuk manggis" motif is very similar to the form of mangosteen fruit before it becomes a fruit, and it signifies grandeur. The gold color symbolizes triumph and power.
43	Middle East ornament	Khat Rayhani calligraphy  Lafadz Allah SWT Lafadz Muhammad SAW	(a) The window of the Pawestren room in Hunto Sultan Amai Mosque, Gorontalo. (b) The front window of the Liwan in Hunto Sultan Amai Mosque, Gorontalo.	The calligraphy is in the Rayhani style and features the words "Allah" and "Muhammad." It is made of iron and colored in green.	This calligraphy writing signifies the element of calligraphy of Allah the Almighty and the Prophet Muhammad PBUH that will never be separated from most of the ornaments in every mosque. It is written using the Rayhani script which is used to write religious books and the manuscript of the Qur'an. The green color symbolizes the color that is identical to the Islamic religion.
44	Arabic Ornament	 The florid shape of the lotus flower motif	Pillars/columns of the Mihrab Liwan at Hunto Sultan Amai Mosque, Gorontalo	The lotus flower motif is formed using cement and colored predominantly in gold and white.	The lotus flower symbolizes the ability to grow and thrive in difficult environments, as it has a wide and flat leaf that floats on the water's surface. It teaches us about adaptation and idealism. The color gold represents triumph and power, while white symbolizes purity.
45	Malay Ornament	The natural shape of a sun motif in English. 	(a) The ceiling around the dome in Hunto Sultan Amai Mosque, Gorontalo. (b) The ceiling of the dome in Hunto Sultan Amai Mosque, Gorontalo.	The natural/cosmic shape of a sun motif, made of gypsum ceiling and colored with gold	The sun motif symbolizes the source of human life and the color gold represents triumph and power.

No	Type of Ornament	Form of Ornament Section	Placement Position	Denotative Meaning	Connotative Meaning
46	Malay Ornament	Jasmine flower leaf 	(a) The top part of the main pillar of Liwan at Hunto Sultan Amai Mosque, Gorontalo. (b) The top part of the additional pillar of Liwan at Hunto Sultan Amai Mosque, Gorontalo.	The floral motif with the design of the jasmine flower leaves is made of molded cement and colored with a white base and predominantly green color.	The plant motif of the jasmine flower adds aesthetic values that provide a sense of beauty to the supporting pillars in every room of the mosque. However, when associated with the jasmine flower, which has the meaning of purity, it adds a symbolic meaning to the ornamentation. The green color represents the identity color of Islam, while the white color symbolizes purity.

The Bubble Diagram below provides a concise and clear overview of the characteristics and meanings of the ornaments of the Hunto Sultan Amai Mosque in Gorontalo, as analyzed through a semiotic perspective (Fig. 11).

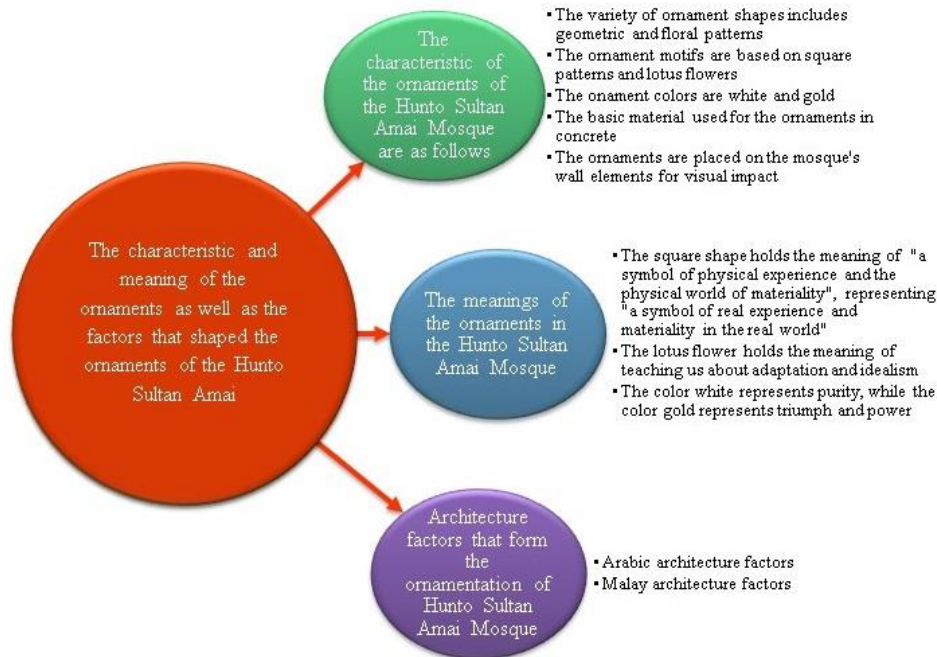


Figure 11. Diagram bubble of ornament characteristics and meanings

5. Conclusion and Suggestion

5.1. Conclusion

This study concludes that the characteristics and meanings of ornaments, as well as the factors that shape the characteristics of ornaments in the interior of Hunto Sultan Amai Mosque, Gorontalo

- The characteristics of ornaments in Hunto Sultan Amai Mosque have a variety of dominant shapes, namely geometric and florid shapes, with basic square patterns and lotus flower motifs. The colors applied in the mosque's interior are predominantly white and gold. The interior ornaments of Hunto Sultan Amai Mosque use mainly paint as the dominant material. The most dominant placement of ornaments is on the mosque walls.
- All ornaments have denotative and connotative meanings from the semiotics perspective of Roland Barthes. The square shape has a connotative meaning of 'symbol of physical experience and the physical world of materiality,' which means 'a symbol of real-life experience and the materiality of the real world.'

The lotus flower motif has a connotative meaning of teaching us about adaptation and idealism. The color white represents purity, while gold represents triumph and power. The placement and materials used in Hunto Sultan Amai Mosque do not have specific meanings from the semiotics perspective of Roland Barthes.

- The architectural style is a factor that shapes the characteristics of the ornaments in the interior of Hunto Sultan Amai Mosque. The Arab architectural style consists of geometric and arabesque lotus flower ornaments. Meanwhile, the Malay architectural style is reflected in the colors used for their symbolic meanings.

5.2. Suggestion

Based on the findings and evaluation, the author recommends the following suggestions

- It is hoped that the people in the community will preserve the entirety of the ornaments and structures of the Hunto Sultan Amai Mosque, without making

any alterations or eliminations, to ensure that the mosque's history is kept for the generations to come and that the distinctive qualities of its ornaments are sustained.

- b. The authors hope that the mosque authorities will establish a dedicated team that can provide information, as the researchers had difficulty finding sources who comprehended the symbolism and meanings of the Hunto Sultan Amay Mosque during their field research. They also hope that in the future, relevant books on the mosque's history, ornament symbolism, and other aspects will be available, given that the Hunto Sultan Amay Mosque attracts tourists and researchers.
- c. It is expected that for future researchers, it is necessary to re-examine the information on the architectural factors that influenced the construction of the Hunto Mosque. This is because the researchers have not seen any specific local elements (Gorontalo) applied to the mosque, while most of the motifs found in the mosque's ornaments, such as geometric motifs, are generally already recognized in Indonesia.

References

- [1] M. Hasyim, "Makna Arsitektur Masjid Pakualaman dalam Tinjauan Kosmologi Jawa," *Analisa*, vol. 18, no. 2, p. 211, 2011, doi: 10.18784/analisa.v18i2.134.
- [2] A. Siola, "Tradisional Dan Modernitas Tipologi Arsitektur Masjid Hunto Sultan Amay Gorontalo," *LOSARI J. Arsit. Kota dan Pemukim.*, vol. 5, no. 1, pp. 1–12, 2020, doi: 10.33096/losari.v5i1.291.
- [3] A. R. Anfa and S. Susanti, "Analisis Semiotika Ornamen pada Masjid Raya An-Nur Riau," *Talent. Conf. Ser. Local Wisdom, Soc. Arts*, vol. 3, no. 3, pp. 153–161, 2020, doi: 10.32734/lwsa.v3i2.875.
- [4] R. Prayogi, "Analisis Ornamen Pada Bangunan Masjid Al Osmani Medan," *PROPORSI J. Desain, Multimed. dan Ind. Kreat.*, vol. 5, no. 2, pp. 217–226, 2020, doi: 10.22303/proporsi.5.2.2020.217-226.
- [5] R. Damanik, W. Sinaga, and Yosrizal, "Local wisdom and functions of malay traditional house in North Sumatera," *Int. J. Sci. Technol. Res.*, vol. 8, no. 4, pp. 38–43, 2019.
- [6] M. Fajar and T. Isfiaty, "Tinjauan Ornamen Pachin Kari pada Arsitektur Mughal Taj Mahal," *Waca Cipta Ruang*, vol. 4, no. 2, pp. 306–311, 2018.
- [7] I. Irwansyah and H. Heldiansyah, "Penerapan Ornamen Melayu Deli pada Rancangan Desain Interior Masjid Pasujudan Jannatun Naim," *PROPORSI J. Desain, Multimed. dan Ind. Kreat.*, vol. 6, no. 2, pp. 103–113, 2021, doi: 10.22303/proporsi.6.2.2021.103-113.
- [8] M. I. Adininggar, E. D. Kurnia, and A. Alfiah, "Penerapan Pembauran Ornamen Islam dan Tionghoa Dalam Arsitektur Masjid Muhammad Cheng Hoo," *TIMPALAJA Archit. student Journals*, vol. 1, no. 2, pp. 140–153, 2020, doi: 10.24252/timpalaja.v1i2a6.
- [9] A. P. H. Nirmala, O. A. Violaningtyas, and R. A. Damayanti, "Ornamen Islam Pada Bangunan Arsitektur Masjid Dian Al Mahri Kubah Emas Depok," *J. Dimens. Seni Rupa dan Desain*, vol. 16, no. 1, pp. 29–42, 2019, doi: 10.25105/dim.v16i1.6159.
- [10] M. R. W. Ghanni *et al.*, "Pengaruh dan Pergumulan Nusantara dengan Arsitektur Asing: Praktek Arsitektur di Era Kelaziman Baru," in *Seminar Karya & Pameran Arsitektur Indonesia: Sustainability in Architecture*, 2020, pp. 376–383.
- [11] T. D. Pancawaty, M. Faqih, F. Teknik, I. Teknologi, and S. Nopember, "Tema: Arabesque," *J. Sains dan Seni POMITS*, vol. 1, no. 1, pp. 1–6, 2012.
- [12] H. Andrina, D. W. Soewardikoen, and N. M. "Ornamen Rumah Tradisional Melayu Riau di Pekanbaru: Rumah Tuan Kadi," *J. Pengetah. dan Peranc. Desain Inter.*, vol. 11, no. 1, pp. 34–49, 2023.
- [13] A. L. D. Harbyantinna, R. S. Raudhoh, and A. Andrianawati, "Ragam Hias Gaya Tionghoa sebagai Identitas Bangunan Candra Naya," *Waca Cipta Ruang J. Ilm. Desain Inter.*, vol. 8, no. 1, pp. 23–27, 2022, doi: 10.34010/wcr.v8i1.6407.
- [14] Al Fiatur Rohmaniah, "Kajian Semiotika Roland Barthes," *Al-Ittishol J. Komun. dan Penyiaran Islam*, vol. 2, no. 2, pp. 124–134, 2021, doi: 10.51339/ittishol.v2i2.308.
- [15] N. F. Bahri, "Analisis Semiotika Roland Barthes pada Masjid Keraton Buton di Kota Baubau, Sulawesi Tenggara," *J. Rupa*, vol. 4, no. 2, p. 121, 2020, doi: 10.25124/rupa.v4i2.2314.
- [16] R. P. S. Hunowu, "Kajian Bentuk Visual Dan Analisis Ornamen Pada Masjid Hunto Sultan Amay Gorontalo," Universitas Komputer Indonesia, 2019.

Thermal Sensation Analysis in the Building of Universitas Ihsan Gorontalo

SitiKhairunnisa Abay^{a,*}, BaharuddinHamzah^b, RosadyMulyadi^c

^aDepartment of Architecture, Faculty of Engineering, Universitas Hasanuddin, Gowa, Indonesia. Email: sitiabay33@gmail.com

^bDepartment of Architecture, Faculty of Engineering, Universitas Hasanuddin, Gowa, Indonesia. Email: baharsyah@yahoo.com

^cDepartment of Architecture, Faculty of Engineering, Universitas Hasanuddin, Gowa, Indonesia. Email: rosady@unhas.ac.id

Abstract

Gorontalo City is characterized by a tropical climate, where thermal comfort is a crucial component to achieve, particularly for educational activities aimed at students. The thermal comfort is affected by various factors, namely building design, internal, and external factors. The university building represents a facility where face-to-face learning and teaching activities occur. The purpose of the current study is to analyze the perceived thermal comfort of students during classroom activities with three different air conditioning (AC) settings (16, 22, and 27 °C) in the Universitas Ihsan Gorontalo campus building. This research employed a quantitative descriptive method, comprising thermal measurements inside the classroom and questionnaire distribution to students to collect thermal sensation data. The research object was conducted in three separate classrooms during the time range of 08.00-15.00 Central Indonesia time. The results revealed that most students felt neutral and comfortable in the three different AC settings inside the classroom. Nevertheless, it should be noted that thermal comfort could be influenced by other factors, such as physical activity and clothing. Consequently, further research could be conducted by taking into consideration these factors and engaging the participation of teachers and staff to acquire a more comprehensive understanding of thermal comfort in the campus building.

Keywords: Thermal comfort; thermal sensation; classroom

1. Introduction

Indonesia is a country characterized by its archipelagic nature and tropical climate. The country's territory encompasses a diverse range of environments, including highlands, lowlands, and mountains, which give rise to varying air temperatures, forming a vertical climate from lowlands to mountains. This vertical climate is characterized by hot, cool, and cold climates. This variability is due to Indonesia's astronomical location, which lies between 6 °C N-11 °C S and 95 ° E-141 ° E, placing it in a low latitude zone and thus resulting in a tropical climate. Among the physical environmental factors affecting the level of comfort while working is thermal comfort. Thermal comfort is a subjective feeling that describes a person's level of comfort with the temperature of their environment. In the context of sensation, thermal comfort is often described as a condition in which a person does not feel too hot or too cold in a given environment [1].

Thermal comfort is essential for the human body to function optimally in various settings, including homes, schools, and workplaces. Comfort is influenced by microclimate variables, such as solar radiation, air temperature, humidity, and wind speed. Additionally,

several individual/subjective factors, such as clothing, acclimatization, age, food/drink intake, obesity, health status, gender, and skin color, can affect comfort levels [2].

According to Humphreys and Nicol, an individual's adaptation to their surrounding temperature also affects their thermal comfort [3]. Individuals who are accustomed to living in hot or tropical climates will have a higher level of comfort than those who are used to living in cooler climates, such as Europe.

Thermal discomfort can be caused by excessively high air temperature, which is influenced by high solar radiation. Vegetation not only contributes to creating comfortable indoor spaces, but can also save energy [4]. Vegetation plays an important role in urban climate and microclimate inside buildings [5].

The environment plays a crucial role in influencing human thermal comfort and productivity within and around buildings. Environmental conditions, such as excessively hot or cold air temperatures, can impact room comfort and work performance [6].

Sunlight reflection, airflow, and vegetation surrounding buildings are some environmental factors that can affect thermal conditions inside and around buildings. Numerous studies have demonstrated that adequate vegetation and airflow can lower air temperatures around buildings and enhance room comfort.

*Corresponding author. Tel.: +62-895-7041-40201
Jalan Poros Malino km.6 Bontomarramu. Gowa
Sulawesi Selatan, Indonesia, 92171

Additionally, the thermal environment is also influenced by the use of materials and building architecture. Factors such as building orientation, ventilation openings and windows, as well as the use of materials on the front facade of the building, can affect the thermal conditions inside and around the building.

Based on these influences, preliminary observations were conducted on the thermal environment conditions outside and inside the buildings of Universitas Ihsan Gorontalo. The initial observations revealed that the external campus area is highly arid, primarily due to the lack of vegetation within the campus surroundings, resulting in elevated air temperatures. Furthermore, a significant portion of the exterior of the buildings has been paved with concrete, and there is a lack of vegetation in the form of green spaces. Consequently, sunlight radiation is reflected back into the air, causing higher air temperatures due to the reduced absorption capacity of the ground surface.

The thermal condition in the building of Ihsan Gorontalo University is still considered uncomfortable. From the architectural aspect, the openings in the form of ventilation and windows in each room use permanent glass material, so they cannot be opened. This is because each room uses air conditioning (AC). If the electricity goes out or the AC is damaged, the room temperature becomes hot. In certain conditions, users of the space become uncomfortable due to the lack of air circulation. The openings in the campus building are also not up to standard. The corridor with minimal openings results in a lack of lighting and airflow entering the building. This certainly also disturbs the comfort of the building users [7].

1.1. Thermal comfort

Thermal comfort is a thermal condition perceived by humans that is influenced by the environment and objects surrounding its architecture [8]. This view shows that thermal comfort is influenced by several factors, one of which is the architectural environment. If the architecture is not in accordance with planning standards, it can affect the thermal comfort of a room [9] explains that the definition of thermal comfort is the thermal balance achieved by the exchange of heat between the human body and the thermal environment at an appropriate level.

Six factors affect thermal comfort according [10]:

- Air temperature
Air temperature is one of the most dominant factors in determining thermal comfort. Units used for air temperature include Celsius, Fahrenheit, Reamur, and Kelvin. Dry bulb temperature, which is the temperature indicated by a regular thermometer bulb in a dry condition, is often used to determine air temperature. Humans are said to be comfortable when their body temperature is around 37° Celsius. Human body temperature is highly influenced by the temperature of their surroundings, and in this case, the laws of thermodynamics apply, stating that

temperature will transfer from a place with a lower temperature.

- Radiant Temperature
Radiant temperature is the heat that radiates from objects that emit heat. Radiant temperature is greater than air temperature in terms of how we release or receive heat from the environment. Each direction of a building has a different amount of radiation formed by the direction of the building that borders the outside and the sunlight that enters. Therefore, when constructing a building, the value of radiant temperature should be taken into account.
- Wind speed
Wind speed is an important factor in thermal comfort. Wind speed is the speed of horizontal airflow at a height above the ground. Wind speed is influenced by the characteristics of the surface it passes over. Still air in a closed space can cause occupants to feel stiff or sweaty. The more uncomfortable the conditions, the higher the required wind speed.
- Relative humidity
Relative humidity is the ratio of the amount of water in the air to the maximum amount of water vapor that the air can hold at that temperature. Humidity in a place will affect the transfer of heat to and from the body. An environment with high relative humidity inhibits the evaporation of sweat from the skin. In a hot environment, less sweat evaporates due to high humidity, causing discomfort for individuals in that environment.
- Clothing insulation
Thermal comfort is greatly influenced by the insulation effect of the clothing we wear. Clothing reduces the release of body heat. Therefore, clothing is classified based on its insulation value. The unit commonly used for measuring clothing insulation is Clo. The comfortable limit for clothing is $n \leq 0.5$ Clo. The total Clo value can be calculated by adding the Clo value for each type of clothing.
- Metabolism level
The level of metabolism is the heat generated within the body during activity. The more physical activity is done, the more heat is produced. The more heat the body produces, the more heat needs to be removed to prevent overheating. Metabolism is measured in MET (1 MET = 58W/m² of body surface area). An average adult human has a skin surface of 1.7 m², and a person in thermal comfort with a 1 MET activity level will have a heat loss of approximately 100 W. When assessing the level of metabolism, it is important to use the average human activity level shown in the last hour.

1.2. Thermal comfort limit

The thermal comfort limit varies depending on the geographic location and the human subjects being studied [11] can be seen in Table 1.

Table 1. Thermal comfort limits

Author	Country	Human Groups	Comfort limit
ASHRAE	USA (30°N)	Scientist	20.5°C – 24.5°C TE
Rao	Calcutta (22°N)	India	20.5°C – 24.5°C TE
Webb	Singapura	Malaysia	25°C – 27°C TE
	Equator	China	
Mom	Jakarta (6°N)	Indonesia	20°C – 26°C TE
Ellis	Singapore	Europe	22°C – 27°C TE
	Equator		

1.3. Thermal comfort zone in a building

- According to Webb the thermal comfort zone for Indonesians [12]:
 - Cool 20.5°C (TE) to 22.8°C (TE)
 - Thermal comfort-optimal 22.8°C (TE)
 - Optimal comfort 26.2°C (TE)
 - Warm 26°C – 27.1°C (TE)
- According to Mom and Wiesebrimm the thermal comfort zone for Indonesians is divided into three zones as follows [12]:
 - Cool comfortable 20.5°C - 22.8°C (TE)
 - Comfortable-optimal 22.8°C-25.8°C (TE)
 - Warm-comfortable 25.8°C-27.1°C (TE)
- The Indonesian thermal comfort standard SNI T-14-1993-03 has three categories:
 - Cool comfortable, 20.5°C-22.8°C, relative humidity 50%-80%
 - Optimal comfort, 22.8°C-25.8°C, relative humidity 70%-80%
 - Almost comfortable, 25.8°C-27.1°C, relative humidity 60%-70%

Furthermore, thermal environmental condition are also influenced by the use of materials and building architecture. The orientation of building, ventilation openings and windows and the use of materials on the building's façade can also influence thermal conditions within and around building [13].

Based on these influences, an initial observation was conducted on the thermal environmental conditions outside and inside the Ichsan Gorontalo University campus building. The initial observation result indicated that the exterior of the campus was very arid, primarily due to a lack of vegetation in the campus environment resulting a hot air temperature around the campus. Additionally, most the exterior building surfaces have been paved with concrete and there is a lack of vegetation such as grass. This inevitably leads to the reflection of sunlight back into air, causing higher air temperatures due to the absence of heat absorption from the ground surface.

In terms of architecture the ventilation openings and windows in each room consist of permanent glass materials that cannot be opened. This is due to the use of air conditioning (AC) in every room. In the event a power outage or AC malfunction, the indoor air temperature becomes hot. The orientation of the Ichsan Gorontalo University building faces west, where the air temperature in the campus environment is extremely hot from 12:00 PM to 4:00 PM local time (Wita). The front

façade of the building is predominantly made of glass material from the first to the third floor without any openings. Most of the wall materials are made of bricks, the ceiling material is plywood and the roof materials is zinc.

The city of Gorontalo has a tropical rain forest climate with temperatures between 22-33°C. The relative humidity in the city of Gorontalo is a $\pm 82\%$ rainy days per year [14].

The purpose of this research is to analyze the thermal sensation in the University campus buildings Ichsan Gorontalo. This research was carried out in order to contribute to science in the field of architecture and development of more sustainable buildings and to create more comfortable thermal environment conditions in and around buildings.

2. Research Method

The research method employed in this study is quantitative descriptive method, which involves collecting data through literature review, field observations, temperature and humidity measurements, as well as questionnaires.

The population of this study is students taking classes in the buildings of Universitas Ichsan Gorontalo. The sample is taken through purposive sampling with the criteria of students who are in classroom C.14 (1st floor), classroom A1 (1st floor), and Architecture Studio (3rd floor) between 8.00 am to 3.00 pm Central Indonesia Time.

The research location is at Ichsan Gorontalo University campus, located Drs. Achmad Nadjamuddin No. 10 street, Dulalowo Selatan Subdistrict, Kota Tengah District, Gorontalo City, can be seen in Fig. 1. Data collection was conducted in the middle of the classroom using a data collection technique consisting of observation, thermal measurement related to temperature and air humidity, and collection of thermal sensation data with questionnaires filled out by students while inside the classroom. The collected data will be analyzed using descriptive statistical techniques. Furthermore, the data from the measurements and questionnaires will be analyzed to find the relationship between air temperature and thermal sensation perceived by the students.

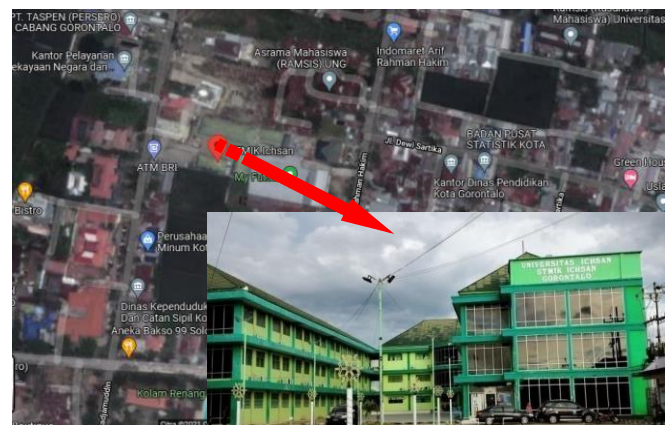


Figure 1. Ichsan University of Gorontalo

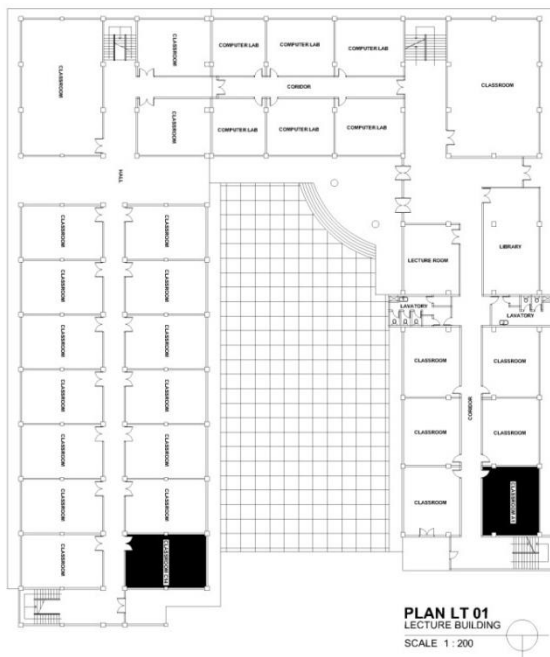


Figure 2. Floor plan 1 Universitas Ichns Gorontalo

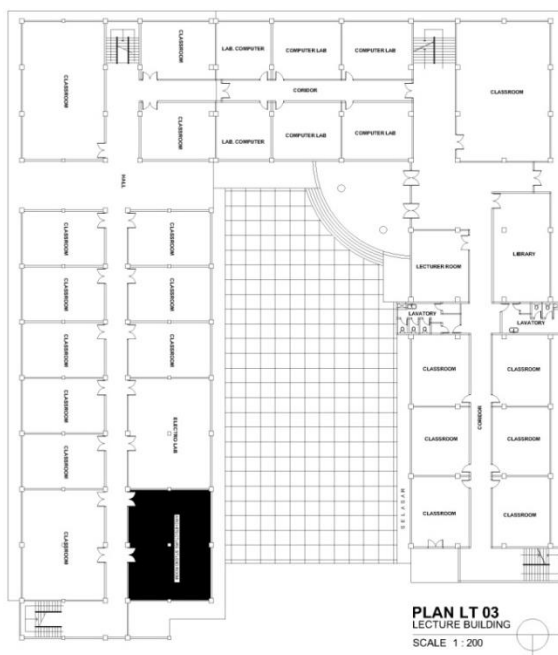


Figure 3. Floor plan 3 Universitas Ichns Gorontalo

The research samples were taken from two classrooms, namely C.14 and A1, located on the first floor of the building. The building is oriented towards the West, and both rooms have different characteristics, can be seen Fig. 2.

The research object on the third floor was only the Architecture studio room, as the adjacent building on the right was a faculty room that was not included in the study, can be seen Fig. 3.

The Fig. 4 is an example representing other rooms for placing measurement points where measurement tools will be placed in each room.

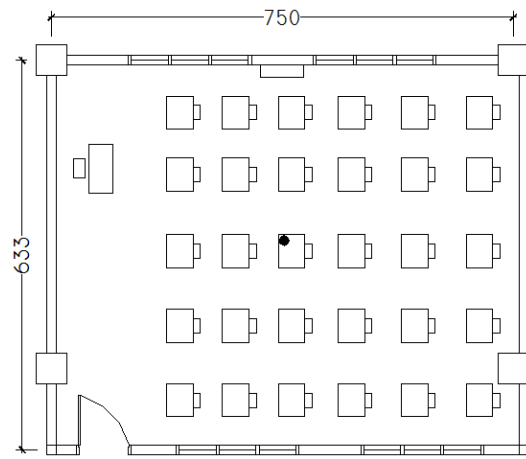


Figure 4. Measurement point in classroom

The selected research objects are classrooms C.14 and A1, and the Architecture Studio room located on the first and third floors. The selection of these research objects is based on their different and interesting characteristics to be investigated regarding thermal comfort.

Classrooms C.14 and A1 have different characteristics and are relatively small compared to the Architecture Studio room. These rooms have different building materials. Classroom C.14 and the Architecture Studio room have one wall made of glass material, while classroom A1 has all walls made of brick material.

3. Result and Discussion

3.1 Thermal environmental condition

The climate of Gorontalo city, based on climate indicators data from the Central Bureau of Statistics throughout 2021, has an average air temperature of 27.10°C with a minimum average temperature of 21.60°C and a maximum average temperature of 35.10°C. The average humidity is 85%, with a minimum average humidity of 43% and a maximum average humidity of 100% [14].

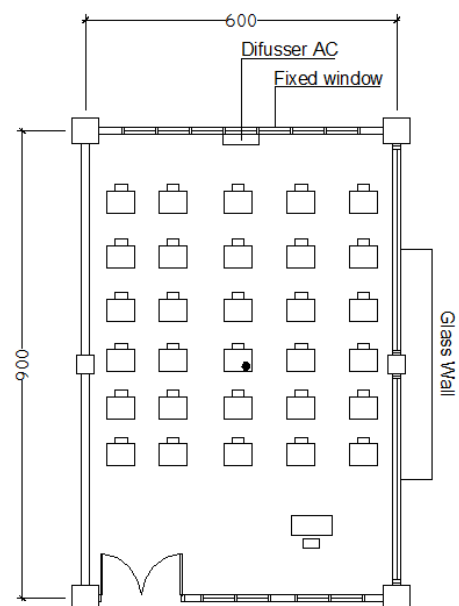


Figure 5. Floor plan of classroom C14, 1st floor

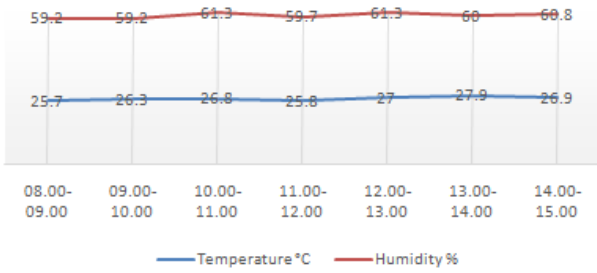


Figure 6. Temperature and humidity in Classroom C.14, 1st floor

1. Classroom C.14, 1st floor

Classroom C.14 is located on the first floor, with an area of 54 m², a length of 9 m² and a width of 6 m². The room has a rectangular shape and is oriented towards the west. One side of the room's wall is made of glass, while the other side is made of brick material and there are two fixed windows, can be seen Fig. 5.

a. Thermostat 16 °C.

The air temperature inside classroom C.14 varied between 25.7°C to 27.9°C, with an average humidity of 60.3%. The lowest temperature occurred at 11:00-12:00 Central Indonesia time with a value of 25.8°C, while the highest temperature occurred at 13:00-14:00 Central Indonesia time with a value of 27.9°C. The highest humidity occurred at 10:00-11:00 and 12:00-13:00 Wita with a value of 61.3%, while the lowest humidity occurred at 08:00-09:00 Wita with a value of 59.2%.

Based on the thermal conditions in the room, the sensation experienced by the respondents (students) can be seen in Fig. 6. Based on the chart, the majority of respondents can be seen Fig. 7 felt comfortable in the room. More than 66.7% of respondents felt comfortable, while only 22.2% of respondents felt slightly comfortable.

In terms of thermal sensation, the majority of respondents felt neutral, which was 59.3% of the total respondents. A total of 33% of respondents felt cold and only 7.4% of respondents felt hot. This indicates that the thermal conditions in the room tend to be optimal and in line with the preferences of the majority of respondents.

Furthermore, only 11.1% of respondents felt very comfortable. However, overall, this data shows that the level of thermal comfort in the room is already quite good and satisfactory for the majority of respondents.

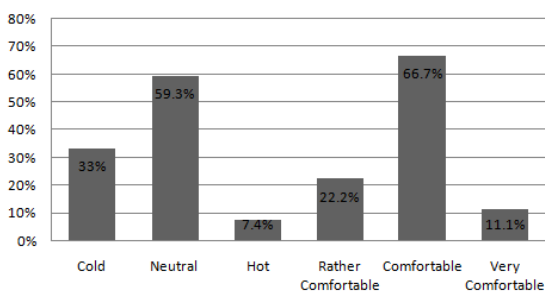


Figure 7. Respondents' thermal sensation charts, Classroom C.14

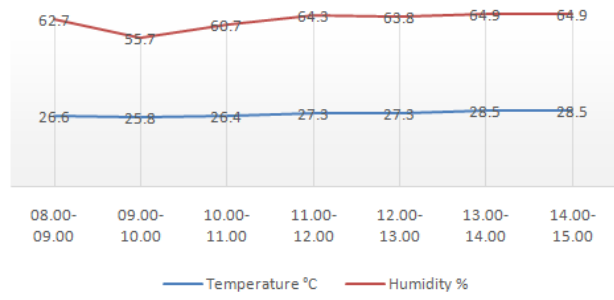


Figure 8. Temperature and humidity in Classroom C.14, 1st floor

b. Thermostat 22°C

The temperature inside classroom C.14 exhibited a significant fluctuation during the observed period, ranging from 25.8°C to its peak of 28.5°C during the 13:00-14:00 Central Indonesia Time interval. The temperature then stabilized at 28.5°C during the 14:00-15:00 interval. Meanwhile, the relative humidity of the room ranged from 55.7% to 64.9%, with less significant fluctuations compared to temperature.

The perceived thermal sensation of the respondents (students) based on the thermal conditions inside the room can be seen in Fig. 8. The chart indicates that most respondents are comfortable in the room, with 41.7% feeling comfortable and 33.3% feeling slightly comfortable. However, 25% of respondents feel very comfortable, indicating the potential to improve the level of thermal comfort in the room can be seen Fig. 9.

Regarding the thermal sensation, half of the respondents (50%) felt cold, while 37.5% felt neither hot nor cold. This implies that the thermal conditions in the room are generally too cold for the majority of the participants.

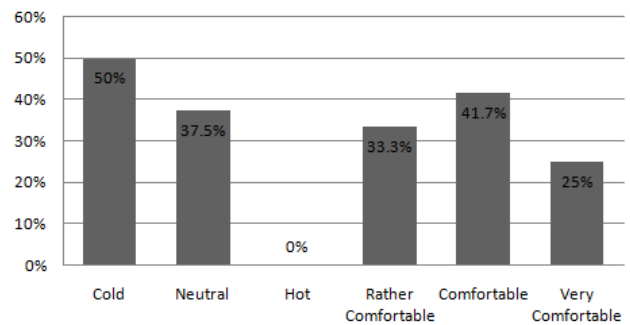


Figure 9. Thermal sensation chart of respondents in classroom C.14

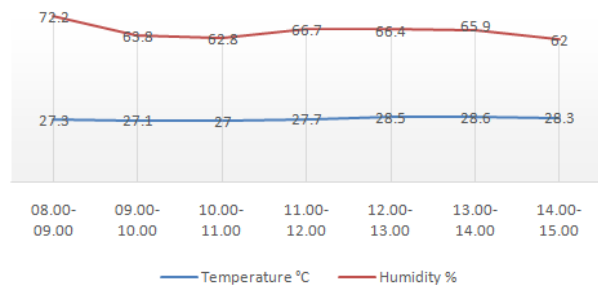


Figure 10. Temperature and humidity inside classroom C.14, 1st floor

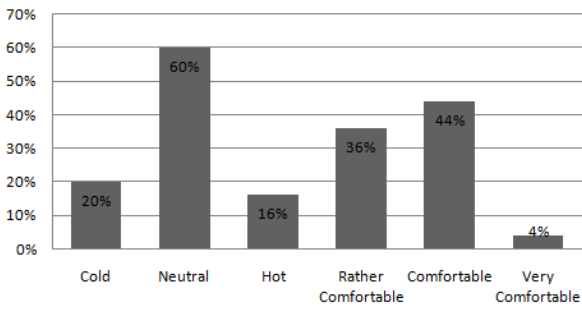


Figure 11. The thermal sensation felt by respondents in classroom C.14

c. Thermostat 27°C

Throughout the observation period, the thermal conditions in the room remained steady, with temperatures hovering between 27-28.6°C. The relative humidity, on the other hand, fluctuated between 62-72.2%. At its peak, the temperature hit 28.6°C between 1:00-2:00 PM, while the humidity peaked at 72.2% between 8:00-9:00 AM (Central Indonesian Time zone).

Figure 10 shows the sensations felt by respondents who were in the room with the thermal conditions as previously described. The chart indicates that most students (60%) have a neutral perception of the thermal conditions in the room, while 44% find it comfortable and only 4% feel very comfortable. However, 20% of students feel cold and 16% feel hot. Additionally, 36% of students find the thermal conditions slightly comfortable.

A significant percentage of students feeling cold and hot, indicates the presence of differences in thermal preferences and needs among individuals in the room can be seen Fig. 11.

2. Classroom A1, first floor

Classroom A1 is located on the first floor, and it has an area of 47.475 m², with a length of 750 m and a width of 633 m. Constructed with brick walls, the classroom can be seen Fig. 12 has no natural openings for ventilation and instead relies on a split air conditioning system for air circulation.

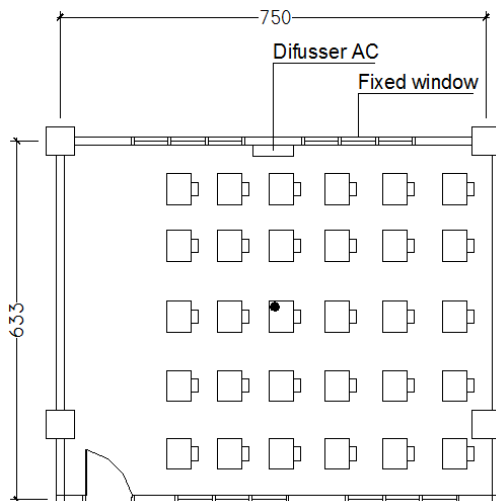


Figure 12. Classroom A, 1st floor

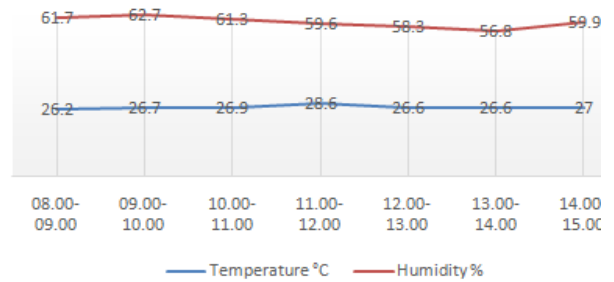


Figure 13. Temperature and humidity in classroom A1, 1st floor

a. Thermostat 16°C

According to the graph, there were significant fluctuations in temperature and humidity within classroom A1 during the observation period. The highest temperature was recorded between 11:00-12:00 WITA, reaching 28.6°C with a humidity level of 59.6%, while the lowest temperature was recorded from 08:00-09:00 WITA, with a temperature of 26.2°C and a humidity of 61.7%. Despite the fact that the relative humidity remained within the comfort range, the considerable temperature fluctuations could affect the thermal comfort in the room.

Based on the previous thermal conditions, the following figure shows the perception of thermal sensation experienced by respondents (students) can be seen Fig. 13.

The graph above indicates that the majority of respondents (80%) experience a cold sensation in the room, with only 20% feeling neutral and none feeling hot. While 60% of respondents feel comfortable, the remaining 40% feel very comfortable. The majority of respondents feeling cold may be due to significant temperature fluctuations during the observation period.

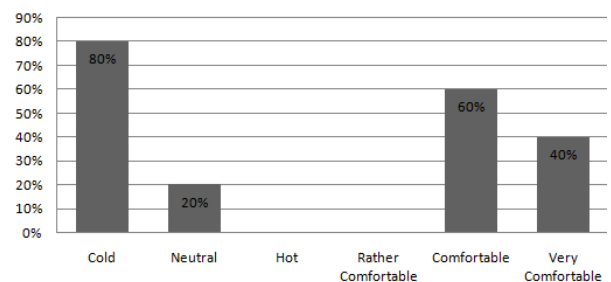


Figure 14. Thermal sensation graph of respondents, classroom A1

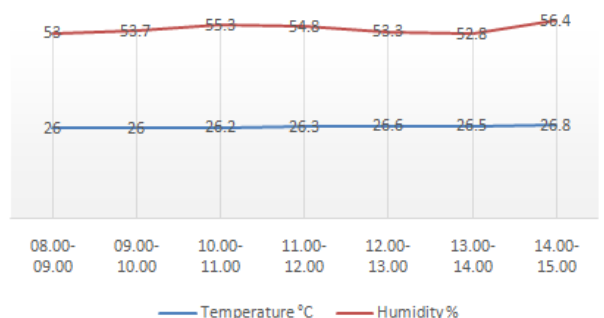


Figure 15. Temperature and humidity inside classroom A1, 1st floor

Nevertheless, the majority of respondents still feel comfortable or very comfortable, implying that the thermal conditions within the room are still quite sufficient to meet human comfort can be seen Fig. 14.

b. Thermostat 22°C

The graph above shows that the room temperature remained fairly constant within a range of 26-26.8°C throughout the observation period. Similarly, the relative humidity also had a relatively narrow range of 52.8-55.3%. However, this range still falls within the range of human comfort. Consequently, it can be inferred that the thermal conditions inside this room can be categorized as comfortable. Based on the previously described thermal conditions, the perception of thermal sensation felt by the respondents (students) can be seen in Fig. 15.

The data collected on thermal sensation revealed that the majority of respondents (66.7%) felt neutral towards the existing thermal conditions. Around one-third of the respondents (33.3%) reported feeling cold, while none of them felt hot. Additionally, an equal number of respondents (50%) felt comfortable and very comfortable, respectively. Notably, none of the respondents reported feeling slightly comfortable. This data suggests that the thermal conditions in the room were generally comfortable for most respondents, despite some feeling cold can be seen Fig. 16.

c. Thermostat 27°C

According to the temperature and humidity data provided, the temperature decreased gradually over the observation period. The highest temperature was recorded between 08:00-09:00 WITA at 27.8°C, while the lowest temperature was recorded between 13:00-14:00 WITA at 26°C. The relative humidity remained within the comfortable range, ranging from 47.5-64.4%.

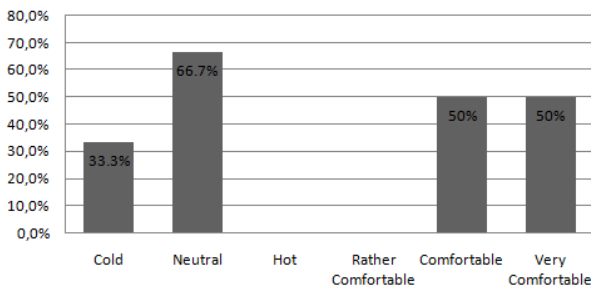


Figure 16. Thermal sensation of respondents chart, A1 classroom

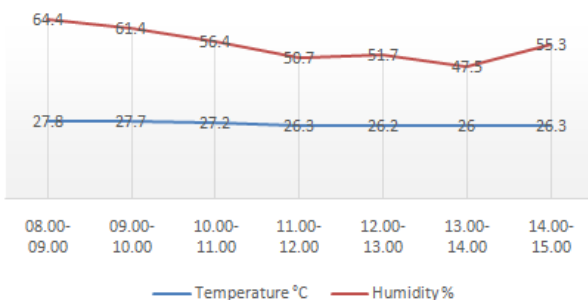


Figure 17. Temperature and humidity inside A1 classroom, 1st floor

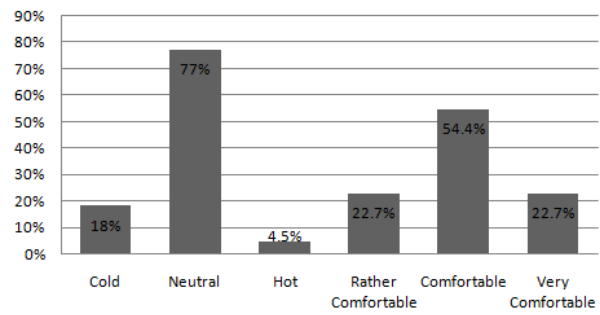


Figure 18. Thermal sensation of respondents chart, A1 classroom

Based on the thermal conditions as explained, the thermal sensation perceptions felt by respondents can be seen in Fig. 17.

The chart shows that most respondents (77%) felt a neutral thermal sensation. A small percentage of respondents (18%) felt cold, and an even smaller percentage (4.5%) felt hot. In terms of thermal comfort, the majority of respondents (54.4%) felt comfortable with the existing thermal conditions, while a portion (22.7%) felt slightly or very comfortable. Therefore, it can be concluded that most respondents felt fairly comfortable with the thermal conditions, although some experienced sensations of cold or heat can be seen in Fig. 18.

3. Architecture Studio Room, 3rd Floor

The architecture studio is located on the third floor, and it has an area of 108 m² with a length of 1200 m² and a width of 900 m². One side of the room's wall uses glass material, while the other side uses brick material can be seen Fig. 19.

a. Thermostat 16°C

The temperature in the architecture studio gradually decreased over the observation period, as indicated by the temperature and humidity data.

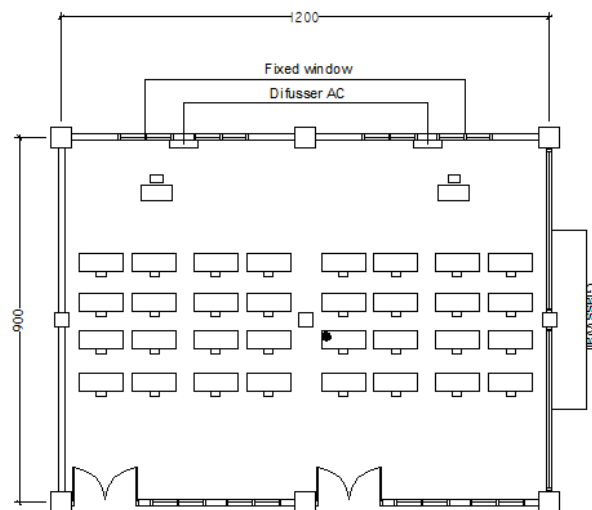


Figure 19. Architecture studio room of 3rd floor, Universitas Ichsan Gorontalo

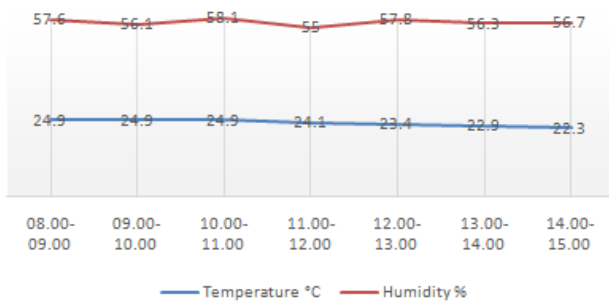


Figure 20. Temperature and humidity in architecture studio room, 3rd floor

The temperature remained stable at 24.9°C, while the humidity ranged from 55-58.1%. Nonetheless, at 11:00-12:00 WITA, there was a considerable drop in temperature to 24.1°C, which then continued to decline until it reached 22.3°C at 14:00-15:00 WITA. While the humidity remained within the comfortable range for humans, fluctuations in temperature can impact the room's thermal comfort.

The Fig. 20 shows the thermal sensation perception felt by respondents (students) based on the thermal conditions inside the room that have been previously described.

The data presented in Fig. 21 shows that most respondents (57.1%) felt comfortable in terms of thermal sensation, followed by feeling neutral (57.1%) and very comfortable (42.9%). On the other hand, feeling cold was reported by 33.3% of the respondents, while only 4.8% felt hot. Unfortunately, there is no data available for the "slightly comfortable" category.

It can be concluded that the majority of respondents felt a comfortable and neutral thermal condition, while the sensation of feeling cold and hot was only felt by a small number of respondents.

b. Thermostat 22°C

The temperature and humidity data that was recorded show that the room temperature fluctuated during the observation period, suggesting that it can change depending on the time and environmental conditions. At specific hours, notably from 11:00-12:00 WITA, the temperature significantly increased and reached 26.3°C with a humidity level of 63.2%.

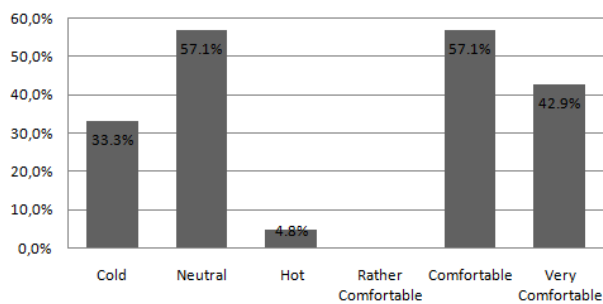


Figure 21. Thermal sensation chart of respondents in architecture studio room

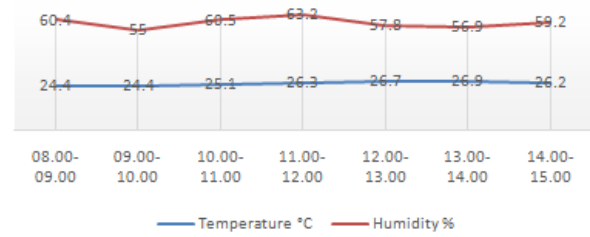


Figure 22. Temperature and humidity in architecture studio room, 3rd floor

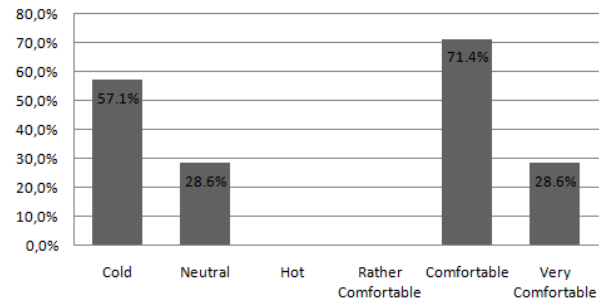


Figure 23. Thermal sensation chart of respondents in Architecture Studio room, 3rd floor

The thermal sensation perceived by respondents (students) in the room depends on the thermal conditions inside the room, as shown in the Fig. 22.

The majority of respondents (students) perceived a thermal sensation in the room, with 57.1% feeling cold, 28.6% feeling neutral, 71.4% feeling comfortable, and 28.6% feeling very comfortable. None of the respondents felt hot or slightly comfortable. These results indicate that most respondents felt comfortable with the room's thermal condition. However, some respondents experienced cold and neutral sensations, which could mean that the room temperature is too low for certain individuals as can be seen in Fig. 23.

c. Thermostat 27°C

The temperature and humidity data presented indicate that there were minor fluctuations observed throughout the study period. At 8:00-9:00 AM WITA, the temperature rose to 26°C, with a humidity of 60.7%. By 9:00-10:00 AM WITA, the temperature dropped to 25.8°C, with a humidity of 54.7%. Between 10:00-11:00 AM WITA, the temperature rose again to 26.5°C, with a relative humidity of 58.3%.

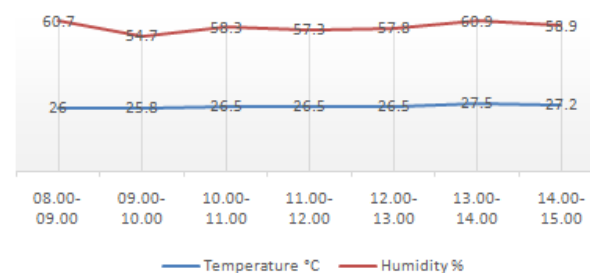


Figure 24. Temperature and humidity inside the architecture studio room, 3rd floor

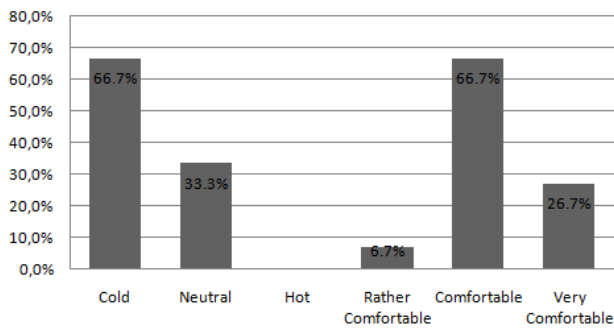


Figure 25. Thermal sensation chart of respondents in Architecture studio room

From 11:00 AM-3:00 PM WITA, the temperature remained steady, hovering around 26.5-27.5°C, while the humidity was recorded between 57.3-60.9%.

Based on the thermal condition notes, it can be concluded that the thermal sensation experienced by respondents can be described through the chart presented can be seen Fig. 24.

Based on the thermal sensation data above, the majority of respondents, 66.7%, felt cold sensation, 33.3% felt neutral sensation, and none of the respondents felt hot sensation. In terms of thermal comfort level, 6.7% of respondents felt slightly comfortable, 66.7% of respondents felt comfortable, and 26.7% of respondents felt very comfortable.

From the analysis, it can be concluded that most respondents felt comfortable with the thermal conditions in the observed Arcitecture Studio room can be seen Fig. 25.

The results of this study describe the thermal conditions in three lecture halls. The majority of respondents felt comfortable and neutral in terms of thermal comfort, although a small portion of respondents felt slightly comfortable, cold, or hot. Significant temperature fluctuations and lower humidity variations can be considered for improving the thermal regulation in the room.

The results of this study illustrate the thermal environment in lecture rooms. Most participants indicated that they experienced a comfortable and neutral thermal sensation, while a minority reported slight comfort, coldness, or warmth. It is important to take into account significant temperature fluctuations and lower humidity variations when aiming to enhance thermal regulation in these rooms.

In thermal and indoor comfort research, several factors need to be considered, including air temperature, humidity, air circulation, wind velocity, radiant temperature, physical activity, and individual preferences. Numerous studies have been conducted to understand thermal preferences in order to seek optimal solutions for creating comfortable thermal conditions indoors.

The ISO standard [15] serves as a frequently utilized resource in this context, outlining principles and parameters for assessing human thermal comfort. It offers guidance on temperature ranges, humidity levels, and other relevant factors that can be utilized as references when designing indoor thermal regulation systems.

The difference between previous research and the present study pertains to the specific emphasis on particular lecture rooms, specifically C.14, A1, and architecture studios. The investigation involved monitoring temperature and humidity fluctuations within a designated timeframe, while also evaluating the respondents' (students) perceived sensations and comfort levels.

Variations in variables and research methods used for studying indoor thermal comfort can result in discrepancies between previous studies and the data presented. These discrepancies arise from differences in research context, methodologies employed, and the specific population being examined.

4. Conclusion

The analysis of temperature and humidity in three sample classrooms showed that most of the respondents felt comfortable with the thermal conditions and perceived a neutral sensation. Nonetheless, some respondents experienced either cold or hot sensations. This suggests that the variations in individual thermal preferences and needs can impact the overall thermal sensation in the room. It is, therefore, crucial to take into account a range of temperature and humidity levels that can cater to the different needs of room users to ensure optimal thermal comfort, 66.7% of respondents felt comfortable at a thermostat setting of 16 degrees Celcius, 66.7% felt comfortable at a thermostat setting of 22 degrees Celcius and 66.7% felt comfortable at a thermostat setting of 27 degrees Celcius with different rooms.

References

- [1] Ashrae Standard, "2010 ASHRAE 90.1 - Energy Standard for Buildings Except Low-Rise Residential Buildings," *ASHRAE/IESNA Stand.*, vol. 2010, pp. 404-636, 1999.
- [2] L. S. Mahabella and M. Abduh, "Kenyamanan termal bangunan rumah tinggal kolonial di sekitar Alun-alun Merdeka Kota Malang," *Semin. Nas. Teknol. dan Rekayasa 2019*, pp. 82-89, 2019.
- [3] B. Talarosha, "Menciptakan Kenyamanan Thermal Dalam Bangunan," *J. Sist. Tek. Ind.*, vol. 6, no. 3, pp. 148-158, 2005.
- [4] N. H. Wong *et al.*, "Thermal evaluation of vertical greenery systems for building walls," *Build. Environ.*, vol. 45, no. 3, pp. 663-672, 2010, doi: 10.1016/j.buildenv.2009.08.005.
- [5] Kepmenkes RI, "Persyaratan Kesehatan Lingkungan Kerja Perkantoran Dan Industri Menteri Kesehatan Republik Indonesia," *Keputusan Menteri Kesehatan Republik Indones. Nomor 1405/Menkes/SK/XI/2002*, pp. 1-22, 2002.
- [6] Y. Y. H. Soegiono and Y. Hadi, "Perhitungan Dan Analisis Efisiensi Penggunaan Air Conditioner Pada Gedung Kuliah Bhakti Persada Universitas Ma Chung," *Spektrum Ind.*, vol. 16, no. 2, p. 149, 2018, doi: 10.12928/si.v16i2.11535.

- [7] Y. Hadi *et al.*, "Analisis Kenyamanan Termal Ruang Kuliah," *J. METRIS*, vol. 21, no. 01, pp. 13–26, 2020, doi: 10.25170/metris.v21i01.2428.
- [8] I. Putri, I. Nurfajriyani, and Q. Fadilatussaniatun, "Pengaruh Suhu Ruangan Kelas Terhadap Konsentrasi Belajar Mahasiswa Pendidikan Biologi Semester Vii (B)," *BIO Educ. (The J. Sci. Biol. Educ.)*, vol. 5, no. 1, pp. 11–15, 2020, doi: 10.31949/be.v5i1.1744.
- [9] H. Sujannah, A. Munir, H. Sawab, M. J. Arsitektur, and D. Perencanaan, "Evaluasi Kenyamanan Termal Hana Cafe Darussalam, Banda Aceh," vol. 3, no. 2, pp. 17–22, 2019.
- [10] A. Schiavon, S. Yang, and B. Donner, "UC Berkeley Indoor Environmental Quality (IEQ) Title Permalink <https://escholarship.org/uc/item/7f01n291> Publication Date," 2016.
- [11] F. G. Noman, N. Kamsah, and H. M. Kamar, "Improvement of thermal comfort inside a mosque building," *J. Teknol.*, vol. 78, no. 8–4, pp. 9–18, 2016, doi: 10.11113/jt.v78.9579.
- [12] S. Latif *et al.*, "Thermal Comfort Identification of Traditional Bugis House in Humid Tropical Climate," *Tesa Arsit.*, vol. 17, no. 1, pp. 61–71, 2019, doi: 10.24167/tesa.v17i1.1803.
- [13] A. Sarinda, Sudarti, Subiki, and M. Program, "Analisis Perubahan Suhu Ruangan terhadap Kenyamanan Termal di Gedung 3 FKIP Universitas Jember 1," *J. Pembelajaran Fis.*, vol. 6, no. 3, pp. 305–311, 2017.
- [14] A. putri Rachmi and M. Hermansyah, *Deskripsi Parameter Cuaca Dan Stabilitas Udara Terkait Kejadian Waterspout Tarakan (Studi Kasus 26 Agustus 2015)*. 2016.
- [15] S. E. Prayoga and A. Kusumawanto, "Thermal Comfort Simulation on Cik Ditiro Corridor," *Dimens. (Journal Archit. Built Environ.)*, vol. 46, no. 1, pp. 67–78, 2019, doi: 10.9744/dimensi.46.1.67-78.

